# Long-Wave Infrared Supercontinuum Source and Sensor for Standoff Sensing and Trace Particle Identification

by

Ramon A. Martinez

A dissertation submitted in partial fulfillment
of the requirements for the degree of
Doctor of Philosophy
(Applied Physics)
in The University of Michigan
2020

Doctoral Committee:

Professor Mohammed N. Islam, Chair
Professor Cagliyan Kurdak
Professor Randy Seeley
Professor Fred J. Terry

Ramon A. Martinez

ramartma@umich.edu

ORCID iD: 0000-0001-7626-780X

For my parents, Ramon and Gloria Martinez

because you gave me everything I needed to succeed

# ACKNOWLEDGEMENTS

*dixitque Deus fiat lux et facta est lux*

And God said let there be light,
and there was light

This dissertation is about infrared light. How to make, how to harness it, and how to understand the information you get back. It has been a long time in coming and there have been so many people to help me along the way.

Thanks to my parents, Ramon and Gloria Martinez. You have always been supportive of everything I've wanted to do academically. Though I did often get the question, "What are you going to do with a degree in physics?" Thank you so much for supporting all the crazy ideas. Everything from dying our hair crazy colors to swing dancing to going away for school. I've been able to accomplish what I have because I knew you were always praying for my success.

Thanks to my brother and sisters for teaching me so much. To Adam for all the hours of Smash and Runescape and MapleStory. For getting excited about hobbies and getting way more diligent about mastering it than I ever was and teaching me how to stick to a task till I'm good at it. To Jackie for teaching me to take risks and know that things will work out in the end through faith in God. Thank you for teaching me to open up and just talk to people because we're all people and it's nice to be heard. To Jojo for teaching me to just get things done. For teaching me to make a decision and stick to my guns and work through the problems that come one

at a time, and sometimes it's fine to just watch trash tv. To Jenna for teaching me to be creative and that with a little bit of patience and guidance even things that can seem overwhelming at first can be accomplished.

My various mentors here at the University of Michigan have shaped who I am as a scientist. Thank you Prof Islam for teaching me to strike at the heart of the problem, to spend time thinking about what the problem is that we need to solve and why people would care. For instilling in me that you can't just make a laser, you have to be able to do something with it. Then when all the nitty gritty is done, it's not worth anything if you can't communicate your findings. Thank you Prof Terry for asking the hard questions, for pushing me to explore good physics problems, and for teaching me the joy of getting quality data. Thank you the times that we got to end research meetings with talk of aquariums and family.

The Applied Physics program has always had my back, and for that I will forever be grateful. Kurdak, you are an amazing director and I hope you never leave. Your passion for science and students is so infectious. Everyone can feel that you care deeply for this program and the people in it. Thank you Charles, Lauren, and Cyndi for helping me navigate AP and grad school. I could always count on your support, whether it was moving a couch or getting people together for Happy hour. Thanks Cindy for making sure that I have sweaters and beanies for my first real winter. Thanks Roy Clarke for enabling Jared and me to run WISE-GISE. It was a great experience teaching the next generation of scientists.

Thanks to my lab mates, who I see more than anyone else. Kaiwen, thanks for all the needlessly intense science conversations and for giving me someone I can bounce ideas off of. Thanks Patrick for your chill competence. Thank you Chitra and Genny for your help in experiments and for helping me learn by teaching what I know. Thanks to Brian, Lucas, Bob, Cindy, Brandon, Mike, and Carl at OMNI. You guys are the real heroes and having you all at OMNI was the golden age of my research

experience. Thank you Augie for getting us the funding that supported the work in this dissertation and all the sassy phone conversations.

Thanks to Paula, Dave, Dan, Barb, Pilar, Dennis, and all the other staff in the EECS building who have helped me navigate its halls and its bureaucracy.

Thank you Randy Seeley for taking me into your group and asking me the same question as my parents, "What are you going to do with your degree after?" Thank you for creating such an open and supportive group that was always willing to help. Thank you to Alfor and the other surgeons for teaching me how to operate on rats, then teaching me how to make sure they live afterwards. Thanks for the hours of conversation that helped me to feel like a part of the team. Thanks to Stace, Jack, Henriette, Simon, and everyone else in the group for all the help in finding my way around the lab.

Thank you to all the folks at AFRL who helped us characterize our fibers and test our SC source vs that of traditional globars. Robert and Ricky thank you for your insight into what a customer might require, and for your support of SC based sources.

Thanks to my friends at the Ann Arbor Seventh Day Adventist Church and Campus Hope. You picked me up from the airport and let me stay over on my first night in Michigan. The hospitality team at Ann Arbor Church has kept me fed on Saturday afternoons at the cost of washing a few dishes and singing a few songs. Thanks to all of you who have supported and prayed for me. For Abide and game nights and white elephants. Thanks Marggie, Abbie, Marina, Tasha, Heaven, Marenda, Geoffrey, Kiana, Brandon, Austin, Marcus, Bamiji, Albert Kim, Kelsey, Roger, Larry, John, Pat, Sal, Lynn, Davina, David, Shoma. You have all made the time spent here worthwhile.

Thanks to friends who came with me from California, Tim and Tiffany, I never would have made this move without you guys, and I would have missed out if I didn't.

My AP peoples have been with me every step of the way. Thanks for the game nights, IM sports, ultimate, and Hamilton. Andrew, it was great living with you. Thanks for the book clubs and snuggles and random shenanigans. Thanks for the trips to see eclipses, and book conventions, and birthday smash weekend, and one night drives to Chicago to see Brandon Sanderson. It's always an adventure. Thank you Jared for co-directing WISE-GISE physics with me, for DMing DND, and dragging me kick and screaming into CSG. While I don't believe all my time there was well spent, I did learn a lot. Thanks Luis and Mal for the honor of officiating and MC-ing your wedding, and for taking that awesome trip down to Miami with Andrew. Sorry Luis for almost burning down your house. Thanks AP people for giving me an outlet for all my extroverted energy after spending all day in lab.

Thanks to improv friends from Pointless. I will treasure my memories from This is a Quiz, The Toast, Bad Brunchers, and all the jams that I've hosted and played in. Thanks for letting me be as weird as I want to be and joining in wholeheartedly.

Thank you to my partner, Linh Huynh. You continually challenge me to work at bettering myself and staying informed. The love and support that we have shared these past 4 years have taught me to become more empathetic and conscientious about how I interact with the world. Thank you for making sure I go to sleep on time and helping me find order in my chaotic walk through life. Here's to many more.

And thanks to you, for reading this. Remind me to tell you about how I had to help kill a chicken. All in the name of science...

# TABLE OF CONTENTS

# LIST OF FIGURES

**Figure**

# LIST OF ABBREVIATIONS

**BV** Bobbert-Vlieger

**Er/YB** Erbium/Ytterbium

**FOM** Figure of Merit

**fs** femtosecond

**FTIR** Fourier Transform Infrared

**LWIR** Long-Wave Infrared

**MFD** Mode Field Diameter

**MI** Modulation Instability

**MIST** Modeled Integrated Scatter Tool

**MFA** Mode Field Adaptor

**MOPA** Master Oscillator Power Amplifier

**MWIR** Mid-Wave Infrared

**NA** Numerical Aperture

**NIR** Near Infrared

**NIST** National Institute of Standards and Technology

**OPA** Optical Parametric Amplifier

**OPD** Optical Path Difference

**OPO** Optical Parametric Oscillator

**PRF** Pulse Repetition Frequency

**PS** Polystyrene

**QCL** Quantum Cascade Laser

**RDX** 1,3,5-Trinitro-1,3,5-Triazinane

**RMS** Root Mean Square

**SC** Supercontinuum

**SNR** Signal-to-Noise Ratio

**SWIR** Short-Wave Infrared

**ZBLAN** $ZrF_4$-$BaF_2$-$LaF_3$-$AlF_3$-NaF

**ZDW** Zero-dispersion Wavelength

# ABSTRACT

This dissertation is based on the development of a long-wave infrared supercontinuum source, and the utilization of this source in a Fourier transform based standoff optical sensor. The spectra from trace particles deposited on smooth surfaces are measured with the sensor and simulated using a Bobbert-Vlieger based model.

We create an ultra-broadband, all-fiber supercontinuum source that emits infrared energy from 1.6 - 11 µm. We utilize a master oscillator parametric amplifier with Erbium/Ytterbium (Er/Yb) and Thulium (Th) amplifiers to pump a cascade of $ZrF_4$-$BaF_2$-$LaF_3$-$AlF_3$-NaF (ZBLAN), arsenic sulfide ($As_2S_3$), and arsenic selenide ($As_2Se_3$) fibers. This source is power scalable and can emit up to 417 mW at 800 kHz pulse repetition frequency, with 69 mW beyond 7.5 µm. The output from the long-wave infrared supercontinuum source is near-diffraction limited single mode output that can be collimated to a one inch spot.

The output of the source is then tested for feasability of use in commercial FTIR based systems. Although not optimized for 1.5 ns pulsed sources, we are able to measure transmission spectra of polystyrene samples, thin films on wafers and 50µL of acetone that has been evaporated in a 10 cm length gas cell and compare to those illuminated with the systems internal globar. We find that even though the input optics are not optimized, the incident energy on the samples is an order of magnitude higher than that of the globar source.

We develop a long-wave infrared standoff sensor by coupling the output of the source to a refraction based FTIR interferometer. The modulated energy is then guided to hit targets that are 3.6 m away from the sensor. The system estimates the

energy of each pulse and creates an interferogram that is Fourier transformed into resultant spectra. The linearity of the sensor is verified via the measurement of thin films of $SiO_2$ and polyimide on silicon wafers. This sensor is then used for standoff volatile gas and bulk sample scattering measurements.

We then focus on the measurement and modeling of trace chemicals that have deposited on smooth substrates. We measure concentrations as low as 6.5 $\mu g/cm^2$ on glass substrates. Furthermore, we measure the diffuse reflectance of RDX, acetaminophen, and caffeine on glass, aluminum, and silicon substrates. Each of these chemicals exhibit spectral features between 950 and 1800 $cm^{-1}$ and substrate based dependencies in reflectance spectra. We simulate these effects with a Bobbert-Vlieger model that takes particle size distribution into account. We find that a range of particle sizes smoothens and broadens reflectance features and changes in target orientation and differences in particle shape can strongly impact the spectra between 1800 and 4000 $cm^{-1}$. We use our Bobbert-Vlieger model to create a library of exemplary spectra based on systematically changing the parameters of the particle size distribution. This library is employed to identify unknown powders based on the root mean square error between the second derivative of measured spectra and those in the library.

# CHAPTER I

# Introduction

## 1.1 Motivation

Imagine a device that acts as a heads-up display for surgeons to help differentiate tumor margins, or where shipping containers can pass optical sensors that check for dangerous compounds and residues. Imagine quality control devices that can quickly determine the thickness and composition of anti-coagulants coating a vial for storage, or sort medical samples quickly based on the chemical signatures of what's inside. Imaging real time smoke-stack emissions monitors that constantly and consistently record emission levels over broad periods of time with part-per-billion accuracy. This dissertation focuses on scientific advances that will lead to making these devices a reality.

We describe the research and demonstration of a non-destructive optical sensor that can determine the chemical composition of particles smaller than a grain of sand and indiscernible to the naked eye. The heart of this dissertation is based on three key requirements for standoff, optical chemical identification: illumination, sensing, and particle modeling. These advances are analogous to three components required for vision: light, eyes, and brain. We first develop a high-power, all-fiber, broadband supercontinuum source that extends from the short-wave to the long-wave infrared spanning 1.6 - 11 µm and outputs energy at power levels that are an order of

magnitude higher than other fiber-based broadband sources available. With a near-diffraction limited beam, this source provides high intensity illumination to standoff targets. We then integrate the output from the source into a Fourier transform infrared based sensor to detect the scattered return from targets placed up to 16 m away. Finally, we the model the effect of small numerical aperture (NA) illumination and collection of scattering from trace particles on a surface at standoff distances, to interpret the chemical signatures that are measured with the FTIR based sensor. These measurements are fundamentally different from the high-NA measurements performed in benchtop applications.

## 1.2 Infrared Light

Infrared light is electromagnetic radiation that spans wavelengths longer than those visible with the human eye. For the purpose of this dissertation we define the ranges as the near-infrared (NIR) (0.75 - 1.0 µm), the short-wave infrared (SWIR) (1 - 2.5 µm), the mid-wave infrared (MWIR) (2.5 - 7 µm) and the long-wave infrared (LWIR) (7 - 15 µm).

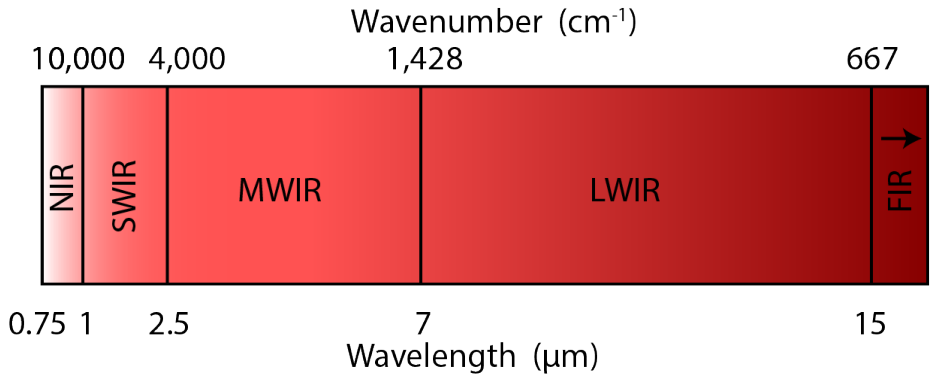


Figure 1.1: Infrared ranges for infrared light in wavelength and wavenumber.

Because some of our equipment operates in the frequency regime, we can also use wavenumber to express a given energy level of light. The conversion between wavelength and wavenumber is:

$$\nu = 10,000/\lambda \tag{1.1}$$

where $\nu$ is wavenumber in $\text{cm}^{-1}$ and $\lambda$ is wavelength in µm. Fig. 1.1 shows the IR ranges on a wavelength scale. Note that wavenumber is inversely proportional to wavelength and, therefore, exhibits a different scale.

Photons in the infrared exhibit energy levels that interact with molecules, through absorption, emission, and reflection. This is the basis for infrared spectroscopy [1] for hydrocarbon-based chemicals. The SWIR contains first overtone (near 1.2 µm), second overtone (near 1.7 µm), and combinational bands (2.0 - 2.5 µm) which are caused by electron transition states. The MWIR contains functional band information associated with bond vibrations. For example, water contains a very strong feature at 3 µm from the O-H bond of water. The LWIR is known as the molecular fingerprint regime (7 - 14 µm) because most molecules have distinct resonances that absorb specific wavelengths of IR light while transmitting others. These resonances are caused by the infrared energy being absorbed by the bonds between elements to cause bending. Because each molecule has a unique set of bonds, these can bend In this way spectroscopists can measure transmission through a sample to determine the identity of a given solid liquid or gas.

## 1.3 Supercontinuum Generation

Supercontinuum (SC) sources provide the best of both worlds between a lamp and a laser. They provide a spectrally broad output with the spatial coherence of a laser. In this way, you can deliver high intensities of broadband light long distances all at the same time.

Supercontinuum generation is a process through which spectrally broad light is produced through non-linear effects in a medium. Supercontinuum generation occurs

in fiber-optics when the peak pulse power in the fiber is high enough to undergo non-linear processes such as self-phase modulation and stimulated Raman scattering which broadens the pulse to shorter and longer wavelengths [2]. Whereas most spatially coherent sources output a single or very narrow wavelength at a given point in time, supercontinuum sources provide spectrally broad outputs.

Most high power, femtosecond (fs) pulses that generate supercontinuum are generated in one of two ways: they can be injected directly into the fiber from mode-locked lasers such as optical parametric oscillators (OPO) [3, 4], or they can be created via modulation instability, where longer pulses break up into hundreds of femtosecond pulses with high peak power. Optical parametric oscillators generate femtosecond pulses by focusing light through a non-linear crystal so that second-order nonlinear effects compress the pulse. This signal can then be amplified through an optical parametric amplifier (OPA) that works under the same principle. One of the benefits of using OPOs to pump SC generation is that the pulses formed have very high peak powers. Very little fiber (on the order of 10 cm) or non-linear crystal is required for broad spectral expansion. The high losses of chalcogenide fibers can be mitigated with short fiber lengths. Furthermore, OPOs can be tuned to emit energy at different wavelengths that extend into the MWIR/LWIR so that supercontinuum generation can be pumped at wavelengths beyond a given fibers zero-dispersion wavelength (ZDW). One of the drawbacks of using OPOs to pump SC generation include bulk optic coupling that requires focusing energy onto the core of the SC generating fiber or crystal, which leads to an increased risk of surface damage. Short fiber lengths also increase the risk of thermal base damage as most of the nonlinear expansion and heating will occur very quickly.

The method for SC generation utilized in this dissertation is to pump the SC generating fibers with nanosecond length pulses that breakup into hundreds of femtosecond pulses through modulation instability (MI). This method allows us to use

commercial off-the-shelf parts for the initial stages of SC generation. Benefits include an all-fiber design, with a near-dispersion limited output, and high power-scalability. MI initiated fs pulses typically exhibit lower peak powers and therefore longer non-linear lengths (on the order of meters) are required for SC generation that extends as broadly as OPO pumped fibers. SC generation via MI initiated pulse break up is much more limited by the loss edge of the fiber used for SC generation.

Prior to the efforts presented in this dissertation, most SC sources that extended into the LWIR were pumped using OPOs emitted average powers of less than 10 mW [3, 5–7], with some sources exhibiting average powers slightly above 30 mW [8, 9]. On the other hand, sources that did exhibit hundreds of mW average power only extended into the MWIR. This dissertation includes details on the creation of a high-power LWIR SC source using MI initiated pulse breakup for SC generation that is the key enabler for standoff FTIR measurements.

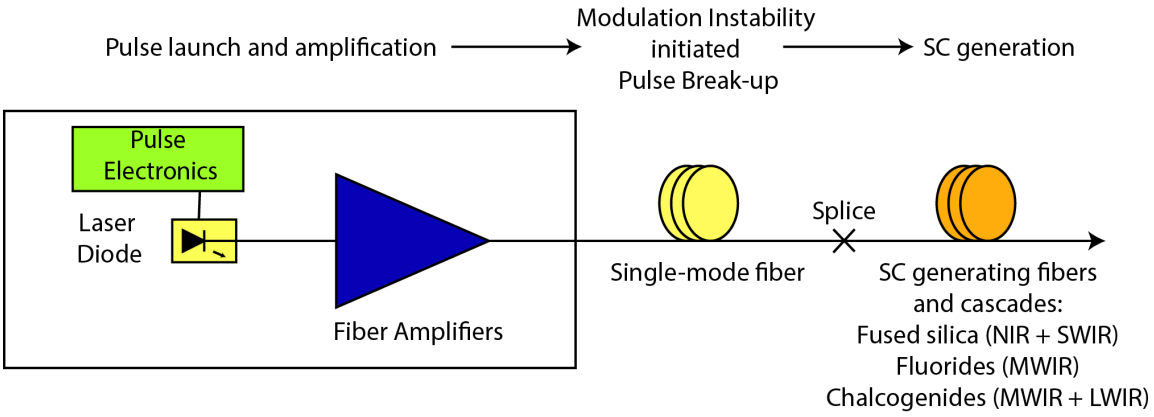


Figure 1.2: General setup for all-fiber based supercontinuum sources that emit in the infrared.

The master oscillator power amplifier (MOPA) scheme for the all-fiber based supercontinuum sources developed in lab is shown in Fig. 1.2. Generally, a pulse from a seed source is amplified several times to increase the peak power to induce pulse breakup via modulation instability. The energy can then be sent through various

super continuum generating fibers which will spread the pulse to shorter and longer wavelengths. Different fibers must be used because each fiber in a cascade has a different loss performance and damage threshold within a given wavelength range. By cascading fibers, we allow SC generation to occur in harder fibers such as fused silica at high peak powers and then output lower powers to softer glasses that may have lower damage thresholds but higher non-linearity.

The specifics for the LWIR source, that I developed during my PhD is described in detail in Chapter II, but most sources created in our lab have a similar architecture. Specifically, in the sources created to expand into the infrared, a 0.5 - 1.5 ns pulse at 1550 nm from a fiber-coupled distributed feedback laser is amplified with forward-pumped, fiber-based Erbium/Ytterbium (Er/Yb) amplifier pumped by up to 8W at 940 nm. After amplification, the pulses are sent through an isolator and band pass filter to remove any excess amplified spontaneous emission (ASE). The resulting light is amplified further to begin modulation instability initiated pulse breakup. The mid-amplifier is a backward-pumped Er/Yb amplifier pumped by up to 20 W at 940, then the energy can be filtered and amplified further by a Thulium (Th) amplifier, or sent through SC generating fibers such as fused silica and $ZrF_4$-$BaF_2$-$LaF_3$-$AlF_3$-NaF (ZBLAN), or chalcogenide fibers, such as, $As_2S_3$, or $As_2Se_3$ fibers [10, 11].

There are many benefits of generating a broadband spectrum in an all fiber system. First, most conventional broadband sources used in spectroscopy, such as light bulbs, halogen lamps, or globars, are spatially incoherent. These sources typically emit in all directions and are difficult to collimate and send long distances. In comparison, our fiber outputs all exhibit a single spatial mode output that is easily collimatable with off-axis parabolic mirrors, and the resulting beam can propagate distances. An all-fiber source also means that there are no moving parts that need to be realigned. Each interface between fibers can either be thermally fused or mechanically butt-coupled and fixed together. This makes the source more rugged than typical mode-locked

sources that pump high energy fs pulses into fibers to generate SC and require bulk optics to guide the pump into the SC generating fibers. Additionally, unlike quantum cascade lasers that emit spatially coherent light at a single wavelength that can be scanned across the MWIR or LWIR [12], SC sources emit all of the radiation at once so that all the energy is available at once. Diffraction gratings and detector arrays can detect multiple wavelengths and entire spectra all at once, but in the LWIR, use of these gratings and arrays is cost-prohibitive, so we use a Fourier transform infrared (FTIR) interferometer to distinguish our wavelengths on a single detector to take advantage of its throughput and multiplex advantages [13].

## 1.4 Fourier-Transform Infrared Spectroscopy

FTIR spectroscopy is a sensing method that shines broadband light on a target and compares the transmission or reflection of the target to a reference scan [14]. The advantage of using an FTIR spectrometer is that a high throughput can be maintained while utilizing all of the wavelengths available at a given point in time, and the output beam can be transmitted over long distances without additional optics.

To do this, a beamsplitter separates the incoming beam of light into two separate arms. One arm is sent towards a stationary mirror and reflected towards the beamsplitter while the other is sent towards a translatable mirror. As the translatable mirror moves, it alters the optical path length of that arm which causes different wavelengths to interfere constructively or destructively when they recombine with the stationary arm signal. This produces an interferogram that compares intensity to mirror position. The interferogram can be Fourier transformed (hence FTIR) into a spectrum. Figure 1.3 shows the setup for a basic Michaelson interferometer.

Spatially coherent sources are ideal for FTIR spectrometers because interferometers work best with collimated beams. Grating monochromators, in comparison, require the source to be focused through a slit before hitting a grating that separates

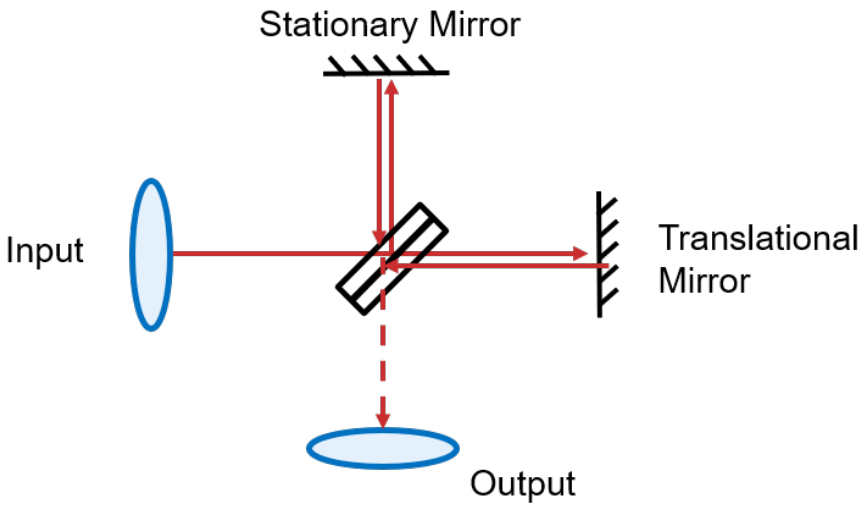


Figure 1.3: Simplified example of a Michaelson interferometer which modulates signal to create an interoferogram that can be Fourier transformed into the spectral regime.

the beam into it's component wavelengths. Wavelengths are scanned as the grating is rotated over a given angle, and the output is then focused through the output slit where it must be collimated to a target or detector.

Grating monochromators are slower than FTIR spectroscopy and creating spectra over several octaves requires bandpass or long-pass filters to prevent second order diffraction from short wavelengths from hitting the detector. Furthermore, only small percentage of the total energy is used at any given point of time, with the rest of the energy outside of the given slit wavelength lost within the spectrometer. The time required to take a full spectrum of our source with a commercial grating monochromator can take on the order of 8-10 minutes and requires a grating change and 2 filter changes. To take a spectrum with the standoff FTIR system described in Chap. III takes less than 2-minutes for a 1000 scan run, 69 seconds for collection and 40 seconds for processing, while commercial systems are even faster. The largest limitation for our prototype system is the transfer of data from the acquisition card to the memory of the computer that runs the processing, and through engineering optimization, this time can be improved.

Standoff spectroscopic techniques include photoacoustic spectroscopy, photothermal spectroscopy, and backscattered reflectance measurements. Photoacoustic spectroscopy involves illuminating samples with infrared energy to induce thermal expansion and create pressure waves that can be measured acoustically. This method works best in sealed environments and is in open air environments by ambient noise levels [15]. Likewise, in photothermal spectroscopy, sample temperature changes of ~1 K are measured via HgCdTe detectors and microbolometer arrays when targets are illuminated with QCLs at absorption wavelengths in the MWIR [16, 17]. This method is limited by ambient temperature differences that may already be present in the environment. Finally, backscattered reflectance involves illuminating a sample with LWIR energy and collecting scattered return, which is one of the foci of this dissertation.

Before the work in this dissertation, all three of the above-mentioned standoff techniques were performed with QCL illuminators and camera based measurement because SC sources did not provide enough power in the LWIR to measure spectral return. We describe how to harness the LWIR SC source in a standoff FTIR based sensor. While an example of an FTIR standoff sensor had been exhibited for a MWIR illuminator [18], our sensor is the first to be developed with LWIR illumination.

The LWIR SC source and FTIR based sensor presented in this dissertation facilitate standoff backscattered reflectance measurements. Scattering from trace particles on surfaces will be decrease with a $1/r^2$ dependence on distance. This makes incoherent blackbody sources unsuitable for standoff illumination because their incident intensity can drop to 1% of its initial value at 4.1 m. We present measurements at 3.6 m with theoretical measurement capabilities up to 16 m. Even at 3.6 m, we find that scattered intensity decreases by 3-4 orders of magnitude compared to the intensity incident on samples with moderate concentrations of ~30µg/cm$^2$. Standoff diffuse scattering measurements also produces spectra that will differ from commercial FTIR

based measurements because standoff measurements require low numerical aperture (NA) illumination and collection.

We provide modeling of trace particle scattering to interpret the results of measurements performed with our LWIR SC and FTIR based sensor. One of the major challenges associated with measuring trace chemicals is that the return spectra depends on not only the chemical in question, but the particle size distribution of the given sample and the substrate upon which the particles rest. In this dissertation we use Bobbert-Vlieger (BV) simulations [19] and log-normal particle size distributions to model trace particles on a surface as spheres of varying sizes. The spectra provided by BV modeling take particle size and substrate effects into account. Previous studies that measure trace detection at a distance have utilized a trans-reflection-based model [20], which uses Mie scattering to determine particle size effects on scattered return. Though accurate for particles on substrates with smoothly varying features, this model treats the substrate as a multiplicative factor for scattered return and does not accurately predict spectra for substrates with their own reflectance features. After we published measurement results using BV theory, new studies have begun to utilize a simplified version of the BV model that uses the Videen approximation [21], which is a near normal incidence approximation [22]. These studies average together the spectra from the entire return hemisphere to create spectra. While providing accurate spectra in the LWIR, the Videen approximation but does not show the oscillatory features that can be found in single size and narrow size distribution cases that are shown in experiment and simulation in Chapter IV.

BV theory, as described in this dissertation, can only model discrete particles on smooth substrates. If a given chemical has been dissolved or forms a bumpy film on the surface of a substrate, BV theory has no adjustable parameters to account for film thickness or particle spacing. Additionally, at very high concentrations, individual particles begin to aggregate and form larger clusters. BV theory assumes that each

particle on the surface is distinct and light that interacts with one particle will not also interact with another. Spectra that is measured with temporally coherent light sources might exhibit interference effects that could not be modeled using BV theory. The insights gained from the modeling efforts described in Chapter IV should help guide the future modeling of more complex targets.

The impact of this work is three-fold. First, we developed a SC source that extends into the LWIR at average powers an order of magnitude higher than any other source at the time to illuminate standoff targets. Next, we integrate the SC source into an FTIR sensor to measure the return infrared backscattered return of standoff targets. Finally, we model the effects of various target parameters to deepen the understanding of the types of spectra that can be measured with the sensor, and we develop a library of spectra for unknown trace chemical identification on smooth surfaces.

## References


[1] Barbara Stuart. Infrared spectroscopy. *Kirk-Othmer Encyclopedia of Chemical Technology*, 2000.

[2] Vinay V. Alexander, Ojas P. Kulkarni, Malay Kumar, Chenan Xia, Mohammed N. Islam, Fred L. Terry, Michael J. Welsh, Kevin Ke, Michael J. Freeman, Manickam Neelakandan, and Allan Chan. Modulation instability initiated high power all-fiber supercontinuum lasers and their applications. *Optical Fiber Technology*, 18(5):349–374, 2012.

[3] Christian Rosenberg Petersen, Uffe Møller, Irnis Kubat, Binbin Zhou, Sune Dupont, Jacob Ramsay, Trevor Benson, Slawomir Sujecki, Nabil Abdel-Moneim, Zhuoqi Tang, David Furniss, Angela Seddon, and Ole Bang. Mid-infrared supercontinuum covering the 1.4–13.3 $\mu$m molecular fingerprint region using ultra-high na chalcogenide step-index fibre. *Nature Photonics*, 8(11):830–834, 2014.

[4] Sergey Vasilyev, Viktor Smolski, Igor Moskalev, Jeremy Peppers, Mike Mirov, Yury Barnakov, Vladimir Fedorov, Dmitry Martyshkin, Andrey Muraviev, Kevin Zawilski, et al. Multi-octave infrared femtosecond continuum generation in cr: Zns-gase and cr: Zns-zgp tandems. In *Nonlinear Frequency Generation and Con-*

*version: Materials and Devices XIX*, volume 11264, page 1126407. International Society for Optics and Photonics, 2020.

[5] Yi Yu, Bin Zhang, Xin Gai, Chengcheng Zhai, Sisheng Qi, Wei Guo, Zhiyong Yang, Rongping Wang, Duk-Yong Choi, Steve Madden, and Barry Luther-Davies. 1.8-10 $\mu$m mid-infrared supercontinuum generated in a step-index chalcogenide fiber using low peak pump power. *Optics letters*, 40(6):1081–1084, 2015.

[6] Uffe Møller, Yi Yu, Irnis Kubat, Christian R. Petersen, Xin Gai, Laurent Brilland, David Méchin, Celine Caillaud, Johann Troles, Barry Luther-Davies, and Ole Bang. Multi-milliwatt mid-infrared supercontinuum generation in a suspended core chalcogenide fiber. *Optics express*, 23(3):3282–3291, 2015.

[7] Tonglei Cheng, Kenshiro Nagasaka, Tong Hoang Tuan, Xiaojie Xue, Morio Matsumoto, Hiroshige Tezuka, Takenobu Suzuki, and Yasutake Ohishi. Mid-infrared supercontinuum generation spanning 2.0 to 15.1 $\mu$m in a chalcogenide step-index fiber. *Optics letters*, 41(9):2117–2120, 2016.

[8] Christian Rosenberg Petersen, Rasmus D Engelsholm, Christos Markos, Laurent Brilland, Céline Caillaud, Johann Trolès, and Ole Bang. Increased mid-infrared supercontinuum bandwidth and average power by tapering large-mode-area chalcogenide photonic crystal fibers. *Optics Express*, 25(13):15336–15348, 2017.

[9] Darren D Hudson, Sergei Antipov, Lizhu Li, Imtiaz Alamgir, Tomonori Hu, Mohammed El Amraoui, Younes Messaddeq, Martin Rochette, Stuart D Jackson, and Alexander Fuerbach. Toward all-fiber supercontinuum spanning the mid-infrared. *Optica*, 4(10):1163–1166, 2017.

[10] Vinay V. Alexander, Zhennan Shi, Mohammed N. Islam, Kevin Ke, Michael J. Freeman, Agustin Ifarraguerri, Joseph Meola, Anthony Absi, James Leonard, Jerome Zadnik, Anthony S. Szalkowski, and Gregory J. Boe. Power scalable¿ 25 w supercontinuum laser from 2 to 2.5 $\mu$m with near-diffraction-limited beam and low output variability. *Optics letters*, 38(13):2292–2294, 2013.

[11] Ramon A Martinez, Genevieve Plant, Kaiwen Guo, Brian Janiszewski, Michael J Freeman, Robert L Maynard, Mohammed N Islam, Fred L Terry, Oseas Alvarez, Francois Chenard, Robert Bedford, Ricky Gibson, and Agustin I Ifarraguerri. Mid-infrared supercontinuum generation from 1.6 to >11 $\mu$m using concatenated step-index fluoride and chalcogenide fibers. *Optics letters*, 43(2):296–299, 2018.

[12] Yu Yao, Anthony J Hoffman, and Claire F Gmachl. Mid-infrared quantum cascade lasers. *Nature Photonics*, 6(7):432, 2012.

[13] Chris A Michaels, Tony Masiello, and Pamela M Chu. Fourier transform spectrometry with a near-infrared supercontinuum source. *Applied spectroscopy*, 63(5):538–543, 2009.

[14] Peter R Griffiths and James A De Haseth. *Fourier transform infrared spectrometry*, volume 171. John Wiley & Sons, 2007.

[15] Charles W Van Neste, Larry R Senesac, and T Thundat. Standoff photoacoustic spectroscopy. *Applied Physics Letters*, 92(23):234102, 2008.

[16] Robert Furstenberg, CA Kendziora, J Stepnowski, SV Stepnowski, M Rake, MR Papantonakis, V Nguyen, GK Hubler, and RA McGill. Stand-off detection of trace explosives via resonant infrared photothermal imaging. *Applied Physics Letters*, 93(22):224103, 2008.

[17] Xing Chen, Dingkai Guo, Fow-Sen Choa, Chen-Chia Wang, Sudhir Trivedi, A Peter Snyder, Guoyun Ru, and Jenyu Fan. Standoff photoacoustic detection of explosives using quantum cascade laser and an ultrasensitive microphone. *Applied Optics*, 52(12):2626–2632, 2013.

[18] Zhaowei Zhang, Rhea J Clewes, Christopher R Howle, and Derryck T Reid. Active ftir-based stand-off spectroscopy using a femtosecond optical parametric oscillator. *Optics letters*, 39(20):6005–6008, 2014.

[19] PA Bobbert and J Vlieger. Light scattering by a sphere on a substrate. *Physica A: Statistical Mechanics and its Applications*, 137(1-2):209–242, 1986.

[20] Robert Furstenberg, Christopher A Kendziora, Michael R Papantonakis, Viet Nguyen, and R Andrew McGill. The challenge of changing signatures in infrared stand-off detection of trace explosives. In *Chemical, Biological, Radiological, Nuclear, and Explosives (CBRNE) Sensing XV*, volume 9073, page 90730M. International Society for Optics and Photonics, 2014.

[21] Gorden Videen. Light scattering from a sphere on or near a surface. *JOSA A*, 8(3):483–489, 1991.

[22] Robert Furstenberg, Andrew Shabaev, Christopher A Kendziora, Christopher Breshike, Tyler J Huffman, Andrew Kusterbeck, Dawn Dominguez, Samuel G Lambrakos, and R Andrew McGill. Synthetic models for infrared reflectance signatures of micro-particle traces on surfaces. In *Chemical, Biological, Radiological, Nuclear, and Explosives (CBRNE) Sensing XX*, volume 11010, page 110100K. International Society for Optics and Photonics, 2019.

# CHAPTER II

# All-Fiber Supercontinuum Generation to >11 µm

## 2.1 Introduction

We pump an all fiber, ZBLAN to arsenic sulfide ($As_2S_3$) to arsenic selenide ($As_2Se_3$) cascade with a master oscillator power amplifier (MOPA) to generate supercontinuum (SC) from 1.6 to > 11 µm with an on-time average power of up to 417 mW at 33% duty cycle. The fiber cascade leads to high output power because each fiber reduces peak power and increases spectral expansion as SC generation is transferred to softer and more nonlinear fibers.

The experimental results point to several important features related to generating broad SC. First, the thulium amplifier absorbs residual 1553 nm light that reduces the damage threshold of $As_2Se_3$ glass. Second, the custom 0.76 NA step-index $As_2Se_3$ fiber achieves high confinement at longer wavelengths and shifts the zero-dispersion wavelength (ZDW) to ˜6.0 µm, which leads to more efficient long wavelength SC generation beyond 6 µm. Finally, the output beam is a single fundamental spatial mode over the full spectrum with a divergence angle that varies across wavelengths as determined by the fundamental mode field diameter (MFD) in the $As_2Se_3$ fiber.

## 2.2 Motivation and Background

Recently, there has been an increased interest in fiber-based SC sources that extend into the molecular fingerprint region in the mid-infrared (6.6 - 20 µm). Because long-wave infrared (LWIR) (7 - 12 µm) light interacts with the fundamental vibrations within molecular bonds, different molecules exhibit unique LWIR absorption spectra. Unfortunately, relatively low output powers have prevented LWIR SC sources from being used in applications such as remote sensing or in-line diagnostics [1]. We demonstrate a LWIR SC source that exhibits both the broad spectral coverage and high average power required for standoff applications.

Several studies in the literature use difference frequency generation or optical parametric generation (OPG) sources to pump chalcogenide fibers and generate SC light beyond 7 µm. However, these pumping schemes are complex and use bulk optics to achieve SC generation. By adjusting the chemical composition of chalcogenide fibers, changing the core structure, or altering the pump wavelengths, SC generated in short lengths of arsenic selenide fibers extends to various points in the mid-infrared at low powers, with some systems extending past 15 µm. [2–5]. Recently, higher power output is achieved by using tapered $As_2Se_3$ fibers. One study achieves 35.4 mW ($1< \lambda <11.5$ µm) and 57.3 mW ($1< \lambda <8$ µm) by pumping different lengths of tapered suspended core $As_2Se_3$ fiber with an OPG [1], while another achieves 30 mW ($1< \lambda <9.5$ µm) by pumping an $As_2Se_3$ taper with a $Ho^{3+}$, $Pr^{3+}$-co-doped ZBLAN laser [6].

Studies that cascade the output of a MOPA system to ZBLAN and suspended core $As_2Se_3$ fibers use bulk optics coupling and a 3.5 µm long pass filter to remove excess power from the ZBLAN output before free space coupling into a short, suspended core $As_2Se_3$ fiber. Reference [7] generates 54.5 mW with expansion to 7.2 µm. In contrast, our system is an all solid core fiber cascade that utilizes the shifting in previous fibers and an $As_2S_3$ to $As_2Se_3$ splice to increase the average output power.

Arsenic sulfide fibers exhibit higher damage thresholds than $As_2Se_3$ fibers and produce total SC power outputs as high as 565 mW, but with wavelength extents of ¡5 µm [8, 9]. The SC generation in $As_2S_3$ fiber is typically limited by a high S-H loss peak at 4 µm, but one study utilizes a tapered $As_2S_3$ fiber to increase nonlinearities and generate SC to 7.2 µm at ˜1mW power levels [10]. In our cascade, the $As_2S_3$ fiber is seeded with SC generated beyond the high 4 µm loss by our ZBLAN fiber and acts as an exceptional intermediary between the ZBLAN and $As_2Se_3$ fiber because of its high power tolerance.

## 2.3 Materials & Methods

### 2.3.1 Laser Design

Our experimental configuration comprises an all fiber, commercial, off-the-shelf, MOPA design to pump a cascade of fluoride and chalcogenide fibers. Figure 2.1 shows an optical block diagram for the SC source. Two Er/Yb doped fiber amplifiers amplify 1.1 ns pulses from a 1.553 µm seed laser operating at a pulse repetition frequency (PRF) between 100 kHz to 800 kHz. These pulses break into several hundred femtosecond pulses through modulation instability in 10 m of standard single mode fiber (SMF) and generate up to 3 W SC from 1.55-2.4 µm via Raman processes, as described in [11]. Then, a 25/400 double clad thulium amplifier absorbs the signal below 1.9 µm and amplifies the signal above 1.9 µm to increase the spectral density past 2 µm. Further details on this system can be found in [12]. The thulium amplifier reduces the average power that would lead to thermal damage of subsequent fibers and maximizes the power that contributes to SC generation. We find that pumping the fiber cascade without the thulium stage greatly reduces the damage threshold of the $As_2Se_3$ fiber and leads to poor spectral expansion. We attribute this effect to two photon absorption within the $As_2Se_3$ fiber [13] and conclude that a thulium amplifier

reduces damage to the $As_2Se_3$ fiber by absorbing 1.55 µm light. Finally, a mode field adapter (MFA) is spliced to the combiner fiber of the thulium amplifier to reduce the core size from a 25/400 fiber to a 0.2 NA, 7 µm core fused silica outputting up to ˜14 W at 800 kHz.

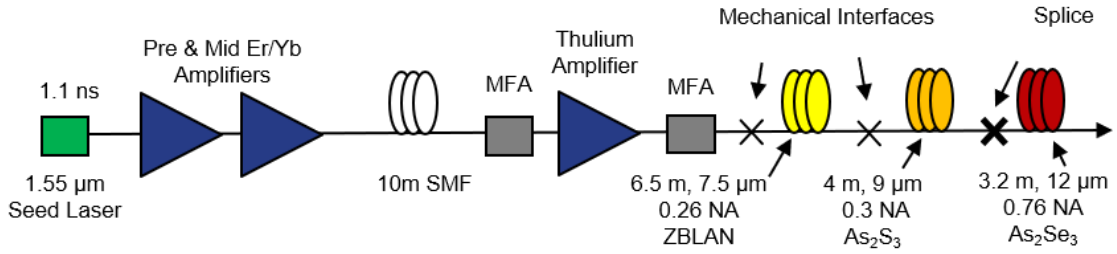


Figure 2.1: Optical block diagram of MOPA and cascade scheme. SMF: single-mode fiber, MFA: mode-field adapter

The thermal load of the system is reduced by connecting the thulium pump diodes in series with a MOSFET switch driven by a 33% duty cycle square wave at 100 Hz. This reduces the likelihood of damage to the final MFA where the intensity of light is increased by an order of magnitude. The average powers described in this study are measured using a thermal power meter then corrected for the 33 % system duty cycle to reflect the average power while the thulium amplifier is on.

The MOPA pump system is used to pump a cascade of fluoride and chalcogenide fibers. The fused silica fiber is angle cleaved and butt-coupled to 6.5m of 0.26 NA, 7.5µm core ZBLAN fiber with a coupling efficiency of >75% (at low peak powers, with background losses and Fresnel reflections taken into account). The output of the ZBLAN fiber is angle cleaved and butt-coupled to 4m of 0.3 NA, 9µm core $As_2S_3$ fiber at a coupling efficiency of >65%. Finally, the $As_2S_3$ fiber is spliced to a 4 m length of 0.76 NA, 12 µm core $As_2Se_3$ fiber using a filament based Vytran splicer (Thorlabs, LFS4000) with a coupling efficiency of >85% to complete the cascade. The $As_2S_3$-$As_2Se_3$ fusion splice works well because the fibers have similar chemical profiles and glass transition temperatures [14].

### 2.3.2 Fiber Interface Management

The optimizing the interface between fibers is the key to providing efficient SC generation. The fibers are first stripped of their outer coating by dipping the end in dichloromethane to soften the plastic. Then using a fiber cleaner cloth that has been dipped in acetone, the coating is gently rubbed off the fiber and discarded. The fibers are then angle cleaved with an angled tension cleaver (Newport FK12). Fused silica is cleaved with a tension of 120, while ZBLAN, $As_2S_3$, and $As_2Se_3$, are cleaved with 76, 60, and 40, respectively. The cleave tension of the ZBLAN must be adjusted dependent upon the humidity of a given day. Humid atmospheres tend to cause the fiber to break while being tightened into the groove and cleaving should happen quickly after fiber stripping to prevent excess water absorption. The fibers should be cleaved at no more than 6-degree angle with ZBLAN and sulfide fibers requiring shallower angles for similar end cleave angles. Steeper cleave angles are more likely to cause nonuniform fiber surfaces that can decrease the fiber damage thresholds, while cleave angles that are too shallow may allow back reflected light back into the pump system. It is also advisable to blow on the chalcogenide fibers gently before cleaving. It is unclear how this helps promote cleaner breakage, but we have found less hackle, less misting, and smoother cleaves on fibers that have been gently breathed upon. We take every pain to have a smooth clean face upon cleaving because it is difficult to polish the soft-fiber surfaces post cleaving, and small discrepancies in end face angles can lead to lower damage thresholds and less efficient expansion in subsequent fibers.

Rotational and translational alignment are critical for high efficiency supercontinuum generation. Before using a UV cure epoxy to fix cleaved fibers to a v-groove, the fibers must be rotated to match end face orientation. Typically, the output fiber is rotated such that the end face is face down under a microscope while the input fiber is rotated such that the end face is face down while looking under the same eyepiece. The binocular view of the microscope allows a second view angle under the second

eyepiece. This view typically shows a straight angle that under small rotations begins to angle. These orientations under the microscope allows for the best horizontal alignment between fibers. The vertical alignment must be monitored via the spectral output of the given fiber. Typically, total power is not enough for maximum expansion and a grating monochromator must be set to a sufficiently high wavelength that is not available from the output of the previous fiber.

In the lab setting, we align fibers that cannot be fusion spiced with 3-axis micron precision stages (Thorlabs, MAX313D nanomax) placed on large steel v-grooves (Thorlabs, HFV001). This allows for precision alignment that can be adjusted to compensate for slight drifts that may occur over time. Unfortunately, this is not a suitable solution for a packaged SC source, first because the nanomax alignment stages are heavy, unwieldy, and take up a great deal of space, but also because there is not a great way to freeze the alignment and maintain a sealed environment. To mitigate these limitations, we have worked with Omni Sciences to develop a tube-on-groove assembly. Small silicon v-grooves are vacuum mounted on custom built holders that fit onto the nanomax stages. Alignment proceeds as described above, but once the power is brought up power and translational alignment is maximized for SC output, sapphire rods are epoxied to the top of the silicon v-grooves to hold the alignment in place. Once curing is complete, the vacuum is turned off and the fixed assembly can be removed from the nanomax base. The tube-on-groove butt-couple is then fixed to a steel heat sink and sealed within a gasket sealed assembly with a molecular sieve desiccant inside. It is important to perform optimal alignment at operating powers because chalcogenide and fluoride fibers begin to expand and shift as they begin to heat up, and performing a "cold alignment" will shift out of alignment at operating temperatures.

### 2.3.3 $As_2Se_3$ Fiber

The high NA $As_2Se_3$ step index fiber is designed to maximize the SC long wavelength edge. The core preform comprises $As_{40}Se_{60}$, while the cladding comprises germanium-doped arsenic selenide. The germanium doping is selected to obtain the index of refraction difference required for a 0.76 NA while maintaining comparable glass transition temperatures during the fiber drawing. The preform is drawn into fibers with 10 µm, 12 µm, and 14 µm core diameters using a double crucible method [14]. Loss measurements, as shown in Fig. 2.2 for the 14 µm fiber, are performed via the cut-back method. The 14µm core $As_2Se_3$ fiber is used in these measurements to maximize coupling from external cavity quantum cascade laser sources (Daylight Solutions, MN 21045 and MN 31090-UT) at wavelength ranges of 4.57-4.76 µm and 7.87-10.53 µm. For comparison, the solid blue curve is the typical loss curve for a 0.3 NA multimode $As_2Se_3$ fiber [15]. Because both fibers exhibit similar loss beyond 8 µm, the background loss of the 0.76 NA fiber may be extrapolated to be $< 0.5$ dB/m. The bump in absorption near 9 µm corresponds to As-O absorption in $As_2Se_3$ glass, the long wavelength absorption tail beyond 9.5 µm is from Se-O absorption, and the higher Se-H absorption loss near 4.5 µm may be due to excess -OH impurities in the fiber [2].

The $As_2Se_3$ parameters are selected based on MFD and dispersion calculations. The Sellmeier equation and coefficients for the $As_2Se_3$ fiber are used with a 1D finite element method based numerical strategy, described in [16], to determine the propagation constants and mode fields of the fiber. The fundamental mode propagation constant is then Taylor series expanded and the second derivate of beta is used to determine dispersion. Figure 2.2 shows the theoretical fundamental MFD and dispersion for the 12 µm 0.76 NA $As_2Se_3$ fiber. The high NA reduces the ZDW to ˜6 µm in all three core diameters. The minimal variation in MFD and shifted ZDW improve SC generation by reducing confinement losses, maintaining a small mode area over

the spectral range, and facilitating soliton formation [11].

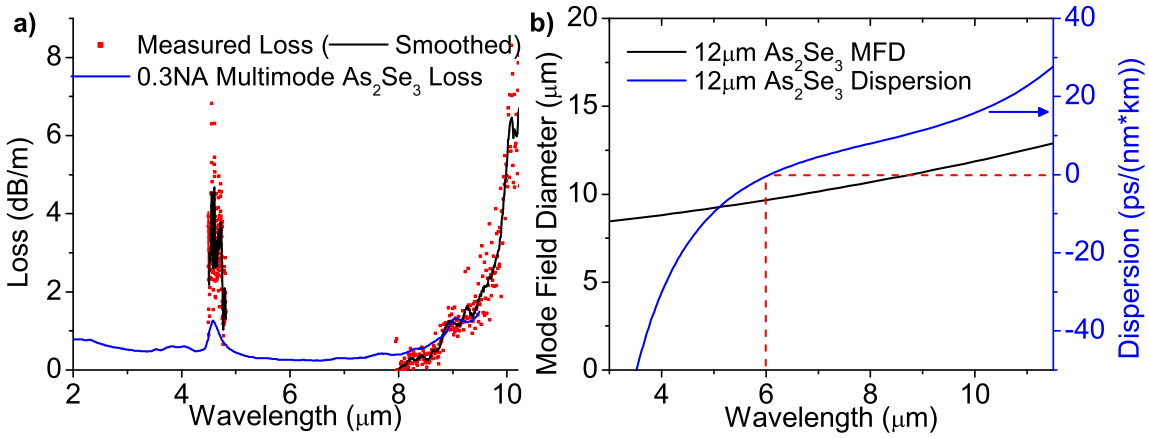


Figure 2.2: a) 0.76 NA, 14µm $As_2Se_3$ fiber loss measured via QCL and typical multimode $As_2Se_3$ loss show high Se-H, As-O and Se-O losses. b) ZDW at ˜6µm and MFD well confined for 0.76 NA, 12µm core $As_2Se_3$ fiber.

### 2.3.4 Laser Characterization

To characterize the performance of our system, we measure the spectral output and beam quality of the pumped fiber cascade. The wavelength expansion of each fiber is measured by coupling their output to a grating based monochromator (Princeton Instruments, SP2150) and detected using a thermoelectrically cooled HgCdTe photoconductive detector (Vigo System S.A. PCI-4TE-13) followed by a lock-in amplifier (Stanford Research Systems, SR865A) with various long pass filters to remove higher order diffraction. The spectra are then corrected for grating efficiency, detector responsivity, and filter losses. The output beam profile of the $As_2Se_3$ fiber is imaged using an InSb based camera (FLIR Systems, Inc. FLIR A6700sc) to view the beam profile at $1 < \lambda < 5$µm and a microbolometer (BAE Systems, Inc. TWV-640) to image $\lambda > 7.5$ µm.

## 2.4 Results

### 2.4.1 Spectral Expansion

Four meters of 12 µm core diameter $As_2Se_3$ fiber provides a compromise between power output and wavelength expansion, with $> 16\%$ of the total power past 7.5 µm and expansion to 11 µm. Figure 2.3 shows the spectral density of the output from the 12 µm $As_2Se_3$ fiber and that the spectrum extends from 1.57 to 11 µm (measured 20 dB down from the plateau in the spectrum, as shown by the red lines). Of the three $As_2Se_3$ fibers pulled, 10 µm core generates SC to 11.4 µm but with 20-25% lower power transmission than the 12 µm core fiber. On the other hand, the 14 µm core fiber shows a -20dB wavelength edge of 10.3 µm, but with 15-20% higher power transmission than the 12 µm core fiber.

Figure 2.4 shows that the generated SC spectra steps out further with each subsequent fiber type while reducing total power. The output of the ZBLAN fiber extends to ˜4.5 µm when pumped with ˜15kW peak power out of the fused silica. Although the pulse breaks into many high-power solitons [11] we estimate the 1.1 ns pulse peak power by dividing the average power out of the fused silica by the product of the pulse width and PRF. When the ZBLAN output is butt-coupled to the step index $As_2S_3$ fiber, the SC extends to just past ˜6.5 µm. Figure 2.4 also shows the spectral shape of the 10 µm $As_2Se_3$ output. The -20dB long wavelength edge for this fiber is 11.4 µm. We believe the dips in the $As_2S_3$ spectrum at 2.7 µm and 4 µm are caused by O-H and S-H impurities in the $As_2S_3$ fiber [8]. The minimum at 3.38 µm in the $As_2Se_3$ fiber seems to correspond to two Raman shifts [17] of the O-H minimum from the $As_2S_3$ output, and the minimum at 4.5 µm corresponds to the Se-H loss peak shown in Fig. 2.2.

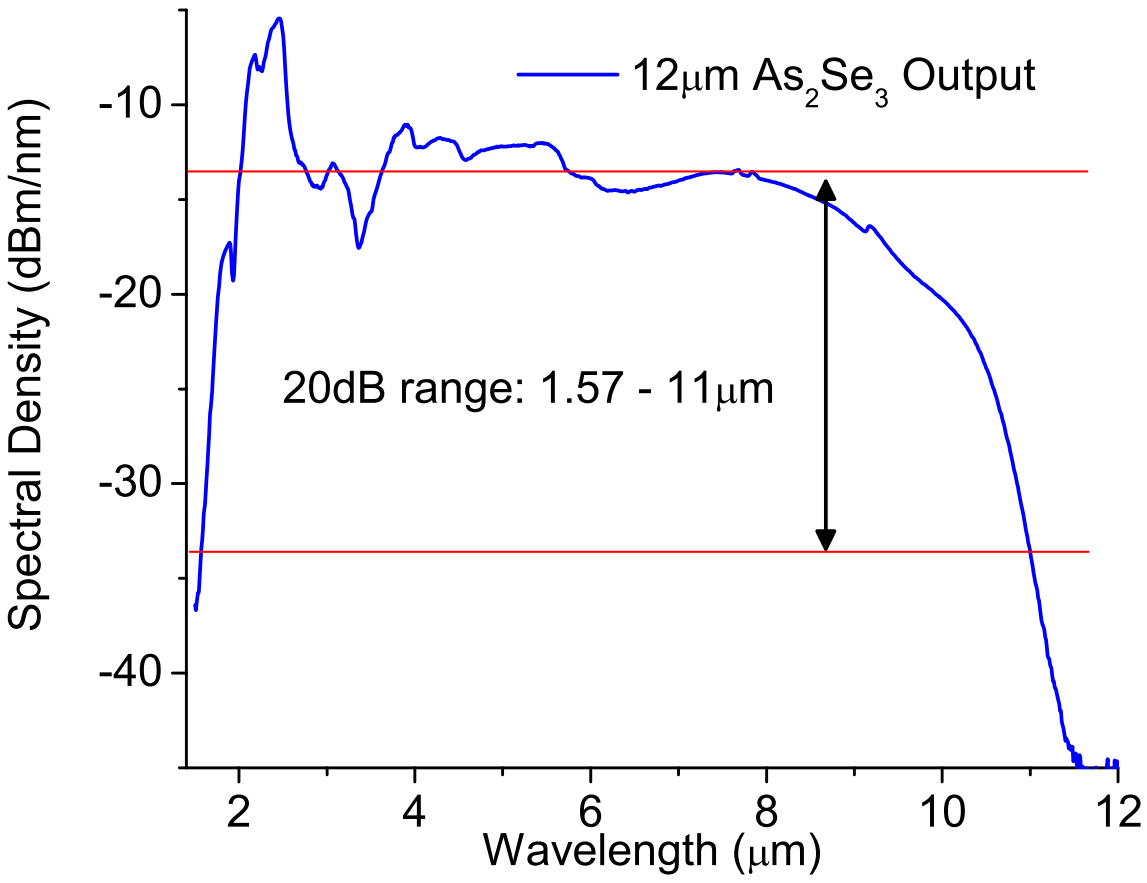


Figure 2.3: 12 µm $As_2Se_3$ output extends to 11 µm.

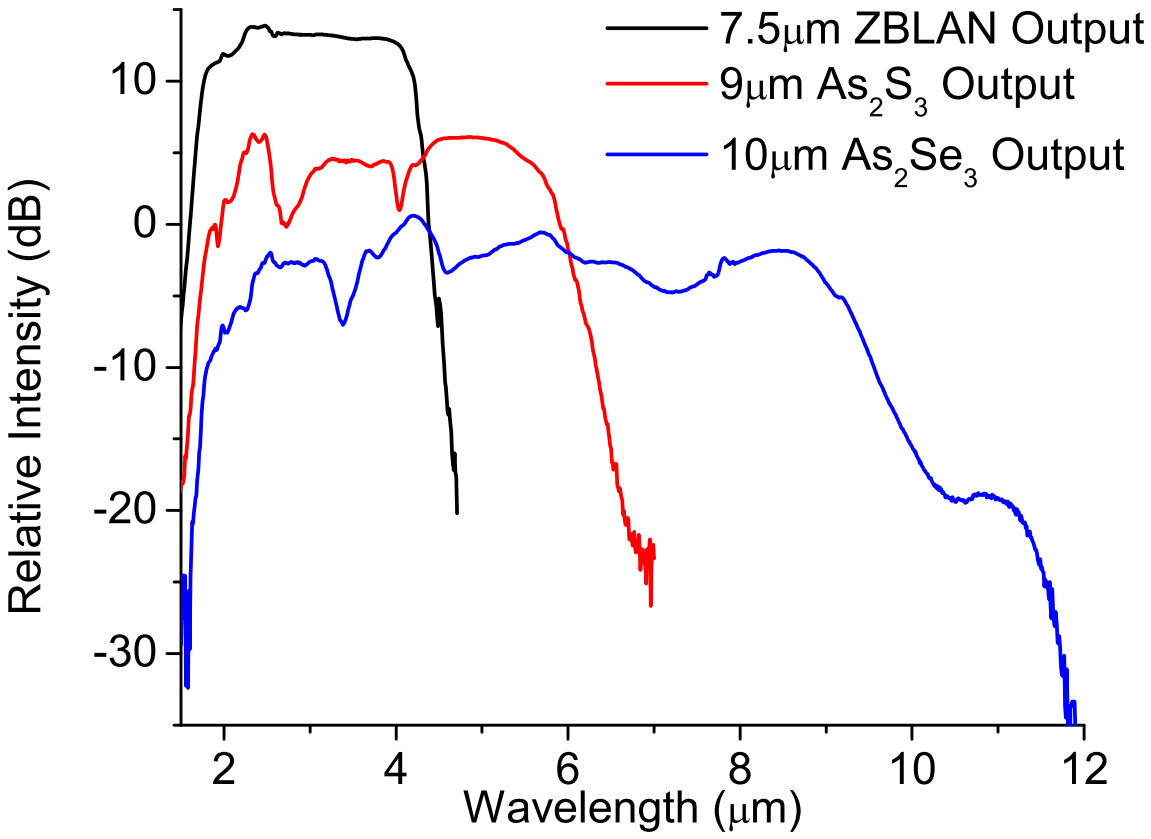


Figure 2.4: Typical spectra after 6.5m of 7.5 µm core ZBLAN, 4m of 9 µm core $As_2S_3$, and 4m of 10 µm $As_2Se_3$ fibers. Power steps down and SC edge increases in successive cascade fibers.

### 2.4.2 Power Scalability

The total power out of the 12 µm $As_2Se_3$ fiber is power scalable by adjusting PRF and thulium pump power. The peak power out of the fused silica fiber determines the SC spectral width, while the number of pulses determines the average power. We increase average power by increasing PRF while adjusting the thulium pump power to maintain near constant peak power. The left-hand side of Fig. 2.5 shows the spectral shape as PRF is increased, and the right-hand side of Fig. 2.5 shows the power in different wavelength bands, which scale linearly with repetition rate. The on-time average power is scalable up to 417 mW at 800 kHz PRF (i.e. The system outputs an average power of 417 mW during the 33% on-time of the 100 Hz modulation). The power between 4.5 - 8 µm, beyond 6.5 µm, and beyond 7.5 µm scale up to 142.5 mW, 108.7 mW, and 69.7 mW, respectively. Furthermore, at 800 kHz PRF the power out of the ZBLAN fiber is 4.88 W, and the power out of the $As_2S_3$ fiber is 1.39 W. To the best of our knowledge, 1.39 W out of $As_2S_3$ and 417 mW out of $As_2Se_3$ are the highest reported SC powers from each fiber type. As shown in Chapter III, these high powers enable stand off sensing in the LWIR.

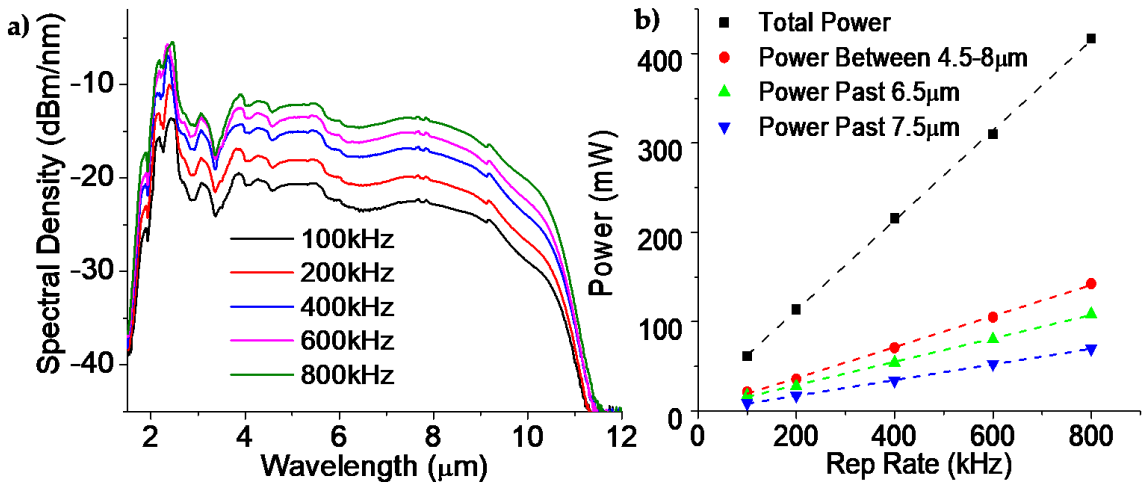


Figure 2.5: a) 12 µm $As_2Se_3$ spectrum scales with PRF. b) Output power scales linearly from 100kHz to 800kHz

### 2.4.3 Beam Profile

The output of our 12 µm core $As_2Se_3$ fiber exhibits a single fundamental spatial mode over the entire wavelength range, but the beam divergence depends on wavelength. This is a somewhat unexpected result, as the $As_2Se_3$ fiber should be multimode over our entire SC range, and may be a result of large differences between the propagation constants of different modes. The beam profile filtered from 3.3-5 µm displays a $1/e^2$ divergence half-angle of ˜16.3°. Figure 2.6 shows a typical 3.3-5 µm beam profile imaged on diffuse reflective aluminum at 75mm from the fiber tip. At wavelengths longer than 7.5 µm, the divergence angle is ˜27.3°. These divergence angles correspond to an $M^2$ value of ˜1.2 when compared to the theoretical Gaussian divergence determined by the MFD within the $As_2Se_3$ fiber at a given wavelength. The single spatial mode output from our light source would provide uniform illumination for standoff applications.

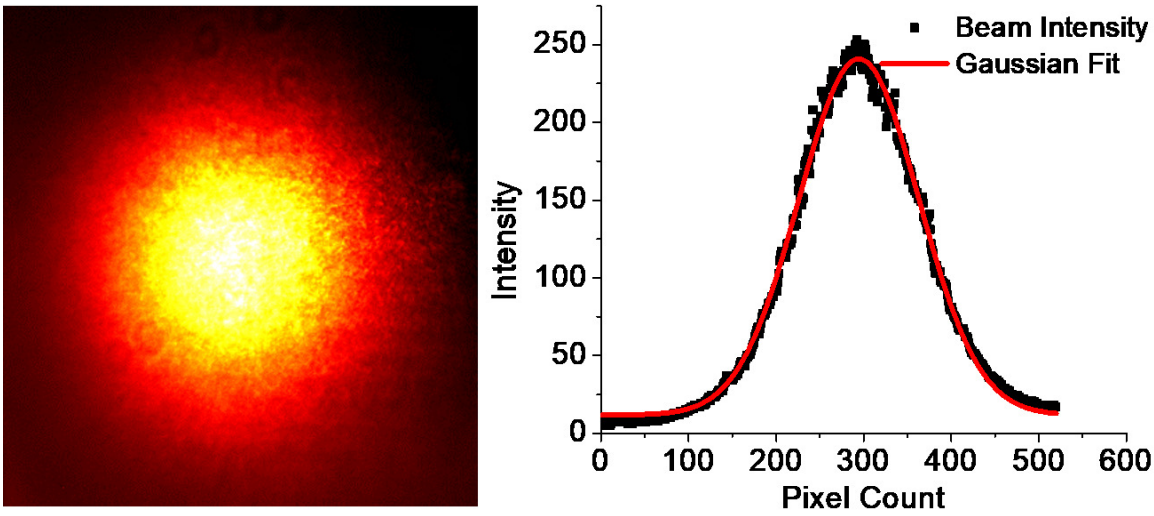


Figure 2.6: Raw image of 3.3-5 µm light incident on scattering aluminum at a distance of 75mm and intensity distribution along the vertical center line fit with a Gaussian profile.

## 2.5 Discussion

### 2.5.1 Cascading Spectral Expansion

In our fiber cascade, each fiber overcomes the shortcomings of the fibers following it. Each fiber has a lower damage threshold than the fiber preceding it. Fused silica fiber is capable of handling high average and peak power outputs, but SC generation is limited by its high loss edge at 2.5 µm. $As_2S_3$ fibers would damage at the ˜15 kW peak powers coming out of the fused silica fiber and provide only minimal shifting at lower peak powers because of their high S-H loss peak at 4 µm. The ZBLAN fiber, however, handles the high peak power and shifts light to 4.5 µm, which is past the high 4 µm loss in the $As_2S_3$ fiber. Although pumped below its calculated ZDW at ˜6.5 µm, the high peak power out of ZBLAN and the high nonlinearity of the $As_2S_3$ fiber [14] allow the SC to expand to 6.5 µm. The $As_2S_3$ fiber shields the $As_2Se_3$ fiber from the high peak power ZBLAN output and shifts energy past the high 4.5 µm Se-H loss and the ˜6 µm ZDW of our 0.76 NA fiber. Light beyond 6 µm in our $As_2Se_3$ fiber improves SC generation through soliton formation [11]. Because of these features, concatenated SC generation yields high output power and broad spectral expansion.

The length of each fiber is optimized to be long enough to maximize spectral expansion, but short enough to prevent excess long wavelength loss. If any fiber in the cascade is too short, we find that too little energy is shifted to longer wavelengths, which causes inefficient SC generation in subsequent fibers and an increased likelihood of damage to the next fiber's input tip. On the other hand, as fiber length increases beyond the optimal length, we observe diminishing returns in spectral expansion, and a decrease in power output as loss increases.

### 2.5.2 Fiber Interfaces

Cascading multiple soft glass fibers introduces the challenge of requiring interfaces between fibers that are environmentally stable and capable of tolerating high powers. The butt-coupled interface between ZBLAN and $As_2S_3$ is particularly sensitive to high average and peak powers and is one of the current challenges limiting higher output powers. The output wavelengths of the ZBLAN fiber extend into water and $CO_2$ absorption bands leading to ZBLAN tip degradation over time. We use a nitrogen purged enclosure to reduce this effect, but an $As_2S_3$ to ZBLAN splice could mitigate this limitation. However, efforts to splice these fibers have not been successful as there seems to be a lack of bonding between the fiber types and all splices lack mechanical strengths. Ball and joint type splices have been carefully created, but they are very difficult to achieve and have very low damage thresholds compared to mechanical butt-coupling methods.

While not as enduring as a constant purge, the tube-on-groove assembly can protect the $SiO_2$ to ZBLAN interface for at least six months and ZBLAN to $As_2S_3$ interface for at least two months before major degradation occurs. we have found that the tube-on-groove assemblies are not air-tight and without the molecular sieve can reach ambient humidity levels over the course of a few days.

The splice between the $As_2S_3$ and $As_2Se_3$ fibers improves long wavelength SC generation and allows power scaling to higher PRF. First, the splice improves the efficiency of SC generation by reducing the 17% back reflection at the sulfide-air interface and the 21% back reflection at the selenide-air interface to a calculated 0.3% back reflection between the two fibers ($As_2Se_3$ index of refraction is 2.7, $As_2S_3$ index of refraction is 2.4). Additionally, the splice prevents heat induced misalignments caused by the fibers' low glass transition temperatures.

One of the reasons this configuration enables such high output powers is because it is an all-solid-core-fiber configuration. Some of the other fiber-based SC generation

schemes include a suspended core or structured selenide fiber for SC generation into the LWIR [2, 4, 5]. While this removes the need of intermediary fibers by shifting the zero-dispersion wavelength to near that of the ZBLAN output, the damage threshold of structured $As_2Se_3$ fibers is limited to near 100 mW average power. Furthermore, there are no lenses or free space optics that may shift in alignment. Chromatic aberrations in lenses limit their usefulness in coupling SC electromagnetic radiation into fibers. Off axis parabolic mirrors must instead be used and alignment typically is plagued by aberrations such as coma and astigmatism. By butt-coupling and splicing fiber sources we prevent high temperature zones which might result from these aberrations.

### 2.5.3 Alternative Configurations

In the process of developing the supercontinuum source with a high efficiency output, several alternate fiber configurations were attempted, and some were found to have merit. We attempted cascade configurations without the sulfide fiber, with $InF_3$ replacing the ZBLAN fiber, and with a fiber configuration called a ZBLAN attenuator.

Supercontinuum generation in a configuration without the $As_2S_3$ fiber proved to provide spectra with little expansion. The major challenge comes from the nature of the supercontinuum generation. At lower peak and average powers there is little to no supercontinuum generation in the $SiO_2$ or ZBLAN fibers. As the Thulium amplifier pumps are increased, peak power and spectra increase hand-in-hand. With the low damage threshold of the $As_2Se_3$ fiber, the end face would be destroyed before any expansion could be seen beyond that of ZBLAN. To mitigate this effect, we developed the ZBLAN attenuator. The ZBLAN attenuator is a short length of ZBLAN fiber that is aligned with the output of the original ZBLAN fiber. The pump power can be increased for maximum supercontinuum generation in the original ZBLAN fiber,

then the ZBLAN attenuator can be retracted from the tip and the distance between tips can be recorded for a set decrease in power typically 20 - 100 mW steps. In this way, we can supply the $As_2Se_3$ with broadband energy while keeping the peak power below the damage threshold of the fiber. Unfortunately, even with this advancement, the spectra output was damage threshold limited to ˜6 µm.

The use of the ZBLAN attenuator has several advantages. Once the ZBLAN fiber length decreases below 4 m, as can happen with subsequent damage and re-cleaves, the output from the ZBLAN fiber does not expand as far spectrally and outputs too high of a power for the input face of the $As_2S_3$ fiber. This happens because the ZBLAN fiber SC generation and background loss are both functions of length. When the fiber is too short, there is not enough SC generation and not enough loss to prevent damage. By adding a ZBLAN attenuator to the shortened original fiber, we can guarantee maximum SC generation in the first ZBLAN fiber and then attenuate the overall peak power output to within the damage threshold of the subsequent sulfide fiber. This typically increases the amount of pump required from the power amplifier but allows us to use shorter fibers for stable SC output.

We tested an $InF_3$ fiber to as a replacement for the ZBLAN fiber in the SC cascade. While the fiber can provide SC expansion to ˜5.5 µm, the output tip of the $InF_3$ is much more likely to damage. The $InF_3$ fiber is also much more prone to damage than ZBLAN fibers. The coating of the $InF_3$ is not rigid enough to prevent damage from even light handling. This even caused the fiber to be damaged during shipping on multiple occasions. Overall, it is currently much more robust to utilize ZBLAN fiber.

Tellurite ($TeO_2$), telluride, and chalcohalide fibers may be useful additions to cascaded supercontinuum generation in the future. While both fibers are still in development, $TeO_2$ fibers may become a replacement for ZBLAN fibers as they are not hydroscopic and can withstand high input and output powers with similar spectral range as fluoride-based fibers [18–20]. Less fiber length may be needed as they also

tend to have much higher non-linearity than ZBLAN fibers. There have also been shown to be able to be effectively spliced to fused silica fibers with very low loss [21]. Telluride fibers would extend the high wavelength edge of the cascade as well. Though with slightly higher background loss profiles than selenide-based fibers, the transparency band for telluride based fibers extends past 14 µm. Instances of low power SC generation to 16 µm in telluride [22] and 15 µm in chalcohalides [23] have been shown in the literature.

### 2.5.4 Intensity at Standoff Distances

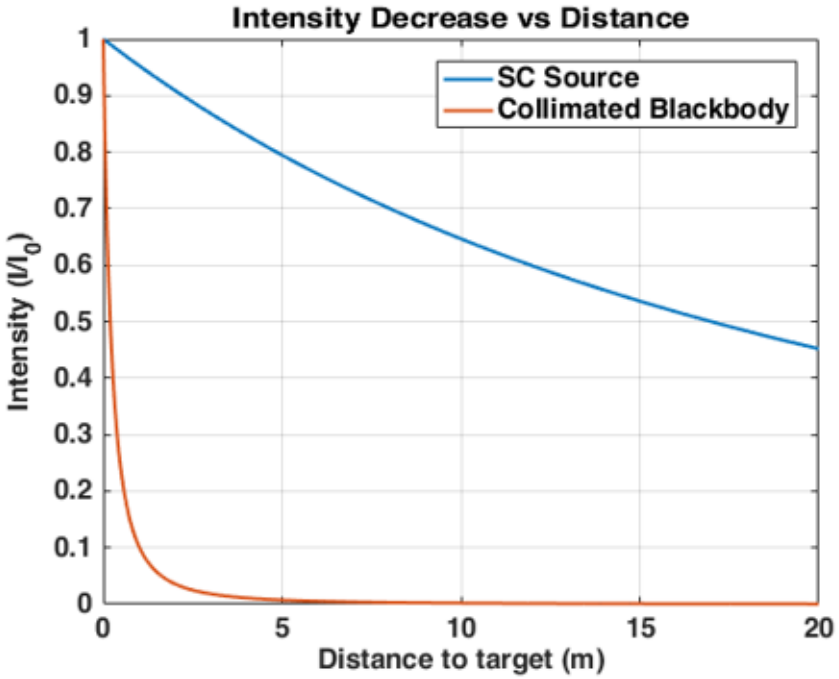


Figure 2.7: Intensity vs distance of a commercial collimated broadband source and that of the LWIR SC source when collimated to a one-inch spot

The near-diffraction-limited beam output provides the high intensity illumination pivotal to increasing scattering from standoff targets. Figure 2.7 shows the intensity decrease of a commercially available broadband source (Thorlabs, SLS203L) with a divergence half angle of 1.3°and that of our LWIR SC source with an initial beam diameter of 1". Although measured $M^2$ values are below 1.3, these calculations show

that even at a worst case $M^2 = 2$ at 5 µm, the intensity of LWIR source only decreases by half at 16 m. In comparison, the blackbody source decreases to 1% of its initial intensity by 4.1 m.

## 2.6 Summary

In summary, we use an all-fiber integrated configuration with concatenated fluoride and chalcogenide fibers to generate high power SC from 1.57 µm to >11 µm. We cascade the SC generation through progressively softer glasses to mitigate the peak power handling limitations of chalcogenide fibers. Concatenated SC generation produces the highest power out of $As_2S_3$ (1.39W) and $As_2Se_3$ (417mW) step index fibers. With 69mW past 7.5 µm, this SC source delivers significant powers and a Gaussian beam profile that can be utilized in standoff applications.

## References


[1] Christian Rosenberg Petersen, Rasmus D Engelsholm, Christos Markos, Laurent Brilland, Céline Caillaud, Johann Trolès, and Ole Bang. Increased mid-infrared supercontinuum bandwidth and average power by tapering large-mode-area chalcogenide photonic crystal fibers. *Optics Express*, 25(13):15336–15348, 2017.

[2] Christian Rosenberg Petersen, Uffe Møller, Irnis Kubat, Binbin Zhou, Sune Dupont, Jacob Ramsay, Trevor Benson, Slawomir Sujecki, Nabil Abdel-Moneim, Zhuoqi Tang, David Furniss, Angela Seddon, and Ole Bang. Mid-infrared supercontinuum covering the 1.4–13.3 $\mu$m molecular fingerprint region using ultra-high na chalcogenide step-index fibre. *Nature Photonics*, 8(11):830–834, 2014.

[3] Yi Yu, Bin Zhang, Xin Gai, Chengcheng Zhai, Sisheng Qi, Wei Guo, Zhiyong Yang, Rongping Wang, Duk-Yong Choi, Steve Madden, and Barry Luther-Davies. 1.8-10 $\mu$m mid-infrared supercontinuum generated in a step-index chalcogenide fiber using low peak pump power. *Optics letters*, 40(6):1081–1084, 2015.

[4] Uffe Møller, Yi Yu, Irnis Kubat, Christian R. Petersen, Xin Gai, Laurent Brilland, David Méchin, Celine Caillaud, Johann Troles, Barry Luther-Davies, and Ole Bang. Multi-milliwatt mid-infrared supercontinuum generation in a suspended core chalcogenide fiber. *Optics express*, 23(3):3282–3291, 2015.

[5] Tonglei Cheng, Kenshiro Nagasaka, Tong Hoang Tuan, Xiaojie Xue, Morio Matsumoto, Hiroshige Tezuka, Takenobu Suzuki, and Yasutake Ohishi. Mid-infrared supercontinuum generation spanning 2.0 to 15.1 $\mu$m in a chalcogenide step-index fiber. *Optics letters*, 41(9):2117–2120, 2016.

[6] Darren D Hudson, Sergei Antipov, Lizhu Li, Imtiaz Alamgir, Tomonori Hu, Mohammed El Amraoui, Younes Messaddeq, Martin Rochette, Stuart D Jackson, and Alexander Fuerbach. Toward all-fiber supercontinuum spanning the mid-infrared. *Optica*, 4(10):1163–1166, 2017.

[7] Christian R Petersen, Peter M Moselund, Christian Petersen, Uffe Møller, and Ole Bang. Mid-ir supercontinuum generation beyond 7 $\mu$m using a silica-fluoride-chalcogenide fiber cascade. *SPIE BiOS*, page 97030, 2016.

[8] Rafael R Gattass, L Brandon Shaw, VQ Nguyen, PC Pureza, Ishwar D Aggarwal, and Jasbinder S Sanghera. All-fiber chalcogenide-based mid-infrared supercontinuum source. *Optical Fiber Technology*, 18(5):345–348, 2012.

[9] Stefan Kedenburg, Tobias Steinle, Florian Mörz, Andy Steinmann, and Harald Giessen. High-power mid-infrared high repetition-rate supercontinuum source based on a chalcogenide step-index fiber. *Optics letters*, 40(11):2668–2671, 2015.

[10] Yingying Wang, Shixun Dai, Guangtao Li, Dong Xu, Chenyang You, Xin Han, Peiqing Zhang, Xunsi Wang, and Peipeng Xu. 1.4–7.2 $\mu$m broadband supercontinuum generation in an as-s chalcogenide tapered fiber pumped in the normal dispersion regime. *Optics Letters*, 42(17):3458–3461, 2017.

[11] Vinay V. Alexander, Ojas P. Kulkarni, Malay Kumar, Chenan Xia, Mohammed N. Islam, Fred L. Terry, Michael J. Welsh, Kevin Ke, Michael J. Freeman, Manickam Neelakandan, and Allan Chan. Modulation instability initiated high power all-fiber supercontinuum lasers and their applications. *Optical Fiber Technology*, 18(5):349–374, 2012.

[12] Vinay V. Alexander, Zhennan Shi, Mohammed N. Islam, Kevin Ke, Michael J. Freeman, Agustin Ifarraguerri, Joseph Meola, Anthony Absi, James Leonard, Jerome Zadnik, Anthony S. Szalkowski, and Gregory J. Boe. Power scalable¿ 25 w supercontinuum laser from 2 to 2.5 $\mu$m with near-diffraction-limited beam and low output variability. *Optics letters*, 38(13):2292–2294, 2013.

[13] Alaa Al-kadry, Chams Baker, Mohammed El Amraoui, Younès Messaddeq, and Martin Rochette. Broadband supercontinuum generation in as 2 se 3 chalcogenide wires by avoiding the two-photon absorption effects. *Optics letters*, 38(7):1185–1187, 2013.

[14] GE Snopatin, VS Shiryaev, VG Plotnichenko, EM Dianov, and MF Churbanov. High-purity chalcogenide glasses for fiber optics. *Inorganic materials*, 45(13):1439, 2009.

[15] IRflex. Irf-se series chalcogenide nonlinear longwave mid-infrared fiber. http://irflex.com/products/irf-se-series-chalcogenide-nonlinear-longwave-mid-infrared-fiber.

[16] JA Mores, GN Malheiros-Silveira, HL Fragnito, and HE Hernández-Figueroa. Efficient calculation of higher-order optical waveguide dispersion. *Optics express*, 18(19):19522–19531, 2010.

[17] Richart E Slusher, Gadi Lenz, Juan Hodelin, Jasbinder Sanghera, L Brandon Shaw, and Ishwar D Aggarwal. Large raman gain and nonlinear phase shifts in high-purity as 2 se 3 chalcogenide fibers. *JOSA B*, 21(6):1146–1155, 2004.

[18] Stefan Kedenburg, Clément Strutynski, Bertrand Kibler, Paul Froidevaux, Frédéric Désévédavy, Grégory Gadret, Jean-Charles Jules, Tobias Steinle, Florian Mörz, Andy Steinmann, et al. High repetition rate mid-infrared supercontinuum generation from 1.3 to 5.3 $\mu$m in robust step-index tellurite fibers. *JOSA B*, 34(3):601–607, 2017.

[19] Chuanfei Yao, Zhixu Jia, Zhenrui Li, Shijie Jia, Zhipeng Zhao, Lei Zhang, Yan Feng, Guanshi Qin, Yasutake Ohishi, and Weiping Qin. High-power mid-infrared supercontinuum laser source using fluorotellurite fiber. *Optica*, 5(10):1264–1270, 2018.

[20] Zhenrui Li, Zhixu Jia, Chuanfei Yao, Zhipeng Zhao, Nan Li, Minglie Hu, Yasutake Ohishi, Weiping Qin, and Guanshi Qin. 22.7 w mid-infrared supercontinuum generation in fluorotellurite fibers. *Optics Letters*, 45(7):1882–1885, 2020.

[21] Yongjing Wu, Pingxue Li, and Chuanfei Yao. High-efficiency fusion splicing of mid-infrared special fibers with the silica fibers. In *2019 Photonics & Electromagnetics Research Symposium-Fall (PIERS-Fall)*, pages 656–662. IEEE, 2019.

[22] Zheming Zhao, Bo Wu, Xunsi Wang, Zhanghao Pan, Zijun Liu, Peiqing Zhang, Xiang Shen, Qiuhua Nie, Shixun Dai, and Rongping Wang. Mid-infrared supercontinuum covering 2.0–16 $\mu$m in a low-loss telluride single-mode fiber. *Laser & Photonics Reviews*, 11(2), 2017.

[23] Kai Jiao, Jinmei Yao, Xian-ge Wang, Xunsi Wang, Zheming Zhao, Bin Zhang, Nian Si, Jia Liu, Xiang Shen, Peiqing Zhang, et al. 1.2–15.2 $\mu$m supercontinuum generation in a low-loss chalcohalide fiber pumped at a deep anomalous-dispersion region. *Optics letters*, 44(22):5545–5548, 2019.

# CHAPTER III

# LWIR SC and FTIR Sensor for Stand-Off Spectral Measurements

## 3.1 Introduction

This chapter describes a Fourier transform infrared (FTIR) spectroscopy-based sensor that measures spectra at 3.6 m with an all-fiber, 1.6 - 11 µm supercontinuum (SC) source for high brightness illumination and a rotational, refraction-based FTIR for high throughput spectral scanning. The testbed sensor was created to study the challenges of standoff chemical detection with an active mid-wave (3 - 8 µm) to long-wave (8 - 14 µm) (MW/LWIR) sensor, and support the creation of a high-speed, portable Supercontinuum Wideband Infrared Fourier Transform (SWIFT) sensor. We establish that the pulsed LWIR SC source can work as an illumination source for a conventional FTIR system. We demonstrate a LWIR and FTIR based sensor for standoff scattering and specular measurements. To demonstrate the linearity of our system, specular return from thin films down to 2 µm thicknesses on wedged silicon substrates are measured at 3.6 m. We also measure the backscatter from various targets and compare those spectra with measurements performed with conventional FTIR spectrometers. The measurements performed in this chapter highlight the feasibilty of measuring backscattered spectra with a pulsed SC source using Fourier

transform infrared spectroscopy to create spectra from collected interferograms.

## 3.2 Motivation & Background

FTIR spectroscopy is commonly used for measuring the MW/LWIR properties of materials, as most chemicals have strong and unique chemical signatures between 3 - 12 µm [1]. Many applications, such as smokestack emissions monitoring [2], food quality control [3], and on-line process monitoring [4], can benefit from active MW/LWIR standoff measurement. However, most common light sources in FTIR spectroscopy are thermal emitters that radiate in all directions. This non-directional radiation often limits the ability to utilize FTIR systems in standoff applications because they are difficult to collimate with appreciable spectral density. Broadband, open-path FTIR systems have been demonstrated, both in passive configurations [5, 6], where a difference in temperature creates spectral differences, and in active sensors, where a retroreflecting element in the location of interest is required to have high optical return [7]. Neither of these techniques are ideal, as the first is limited by the temperature difference between the background and target, and the second depends on the placement of reflective optical elements and can typically only be used to study gases. Some studies have utilized optical parametric amplifiers or external cavity quantum cascade lasers as active light sources for standoff spectroscopy but the light sources used were narrow band [8, 9], or require wavelength tuning and IR imaging cameras that have a limited resolution [10, 11]. In using a MW/LWIR SC source and FTIR configuration, our sensor illuminates with a modulated broadband beam, and provides ˜16 scans per second with the potential for faster acquisitions.

There have been several demonstrations of FTIR-based measurements with SC sources [12–14]. These studies operate in the short-wave (0.7 -2.5 µm) to mid-wave infrared and do not explore a standoff detection scheme but note that SC sources exhibit higher variation than blackbody sources. Recent MW/LWIR SC sources provide

high output power and spectral coverage rivaling that of blackbody emitters in the MW/LWIR [15–17], where unique chemical signatures are much stronger than in the short-wave infrared [1]. In our study, we perform active standoff FTIR spectroscopy with the MW/LWIR SC illuminator described in Chapter II.

## 3.3 LWIR SC Illumination in a Commercial FTIR system

In this section, we wish to test the suitability of a pulsed LWIR SC source for FTIR spectroscopy, independent of the other experimental system components. The reason we perform these experiments is to determine if the fs pulses within the ns pulse envelope correctly interfere and produce consistent spectra that is comparable to conventional blackbody light sources upon Fourier Transform. HgCdTe detectors are notorious for having very small linear ranges [1] and the high peak power in the fs pulses could push the detector into the non-linear regime. Furthermore, liquid nitrogen cooled HgCdTe detector bandwidth limits can force the 1.5 ns input pulse to spread into a quasi-continuous intensity change.

The output from the source described in Chapter II is launched into a commercial, Michelson interferometer based FTIR (JASCO, Inc, USA, FT/IR-6300), and the transmission spectra of various materials are measured. The measurements in the FT/IR-6300 are performed in continuous scan mode with a scan rate of 1 mm/sec, an aperture of 3.5 mm, and a 4 $cm^{-1}$ resolution. The SC source is operated at 100 kHz pulse repetition frequency and 100% duty cycle to adjust the average output power to ˜50 mW. Transmission spectra are compared to measurements taken with the interferometer's default internal globar. Although the FTIR in use is not optimized for pulse acquisition, the slow scan speed allowed the internal software to average over several hundred nanosecond pulses for a given interference position. The spectra in Fig. 3.1 are created by averaging 256 target scans and performing a ratio between them and the average of 256 background scans.

Along with the transmission measurements through solids, volatile gas measurements are performed by placing a 10 cm path length gas cell with AR coated, wedged ZnSe windows within the sample chamber of the commercial FTIR spectrometer. Background scans are performed with the gas cell in place in the chamber with no volatile solvent present.

### 3.3.1 Results of Globar and MW/LWIR SC Source Measurements

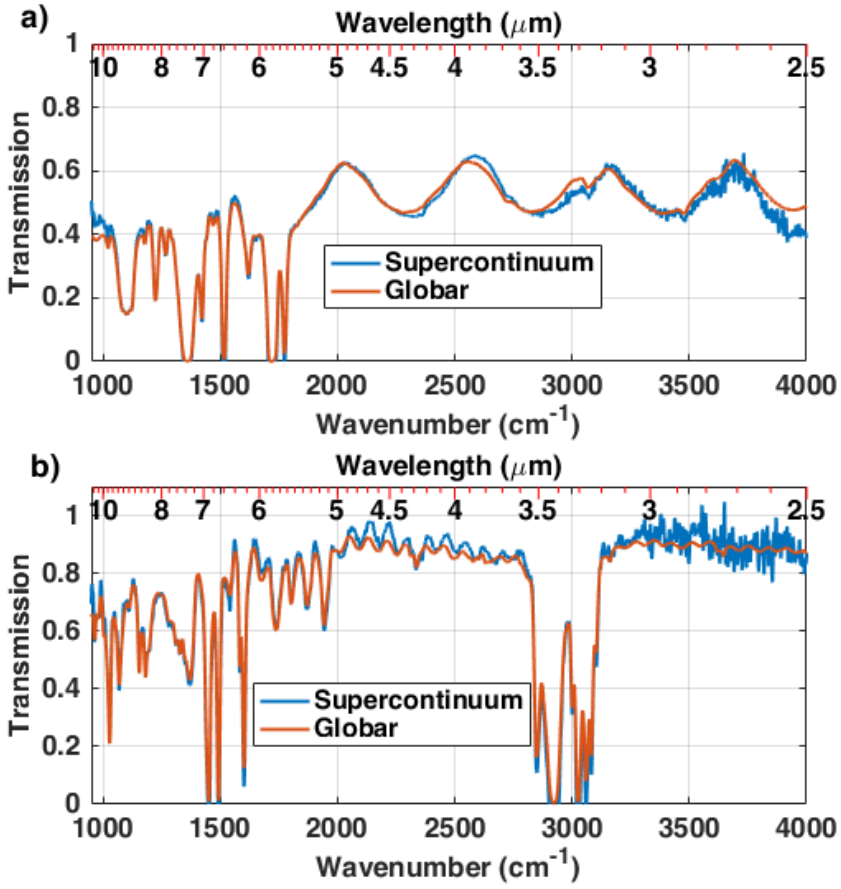


Figure 3.1: Comparison of transmission spectra using a blackbody source vs a SC source in a Michelson interferometer FTIR system of a) polyimide on wedged silicon and b) polystyrene.

Transmission spectra are performed within a single FTIR with a blackbody and SC source. Fig. 3.1 shows a comparison of the transmission spectra of a) polyimide on

silicon and b) polystyrene using illumination by a globar versus that of our SC source. With all other parameters and optics kept constant, the SC produces matching spectra and requires an additional 10 dB attenuation to achieve interferogram magnitudes that matched that of the blackbody source. Because this is a purged setup, the measured spectra do not exhibit water or $CO_2$ based atmospheric losses. However, there are is a relatively low spectral density per wavenumber above 3000 $cm^{-1}$.

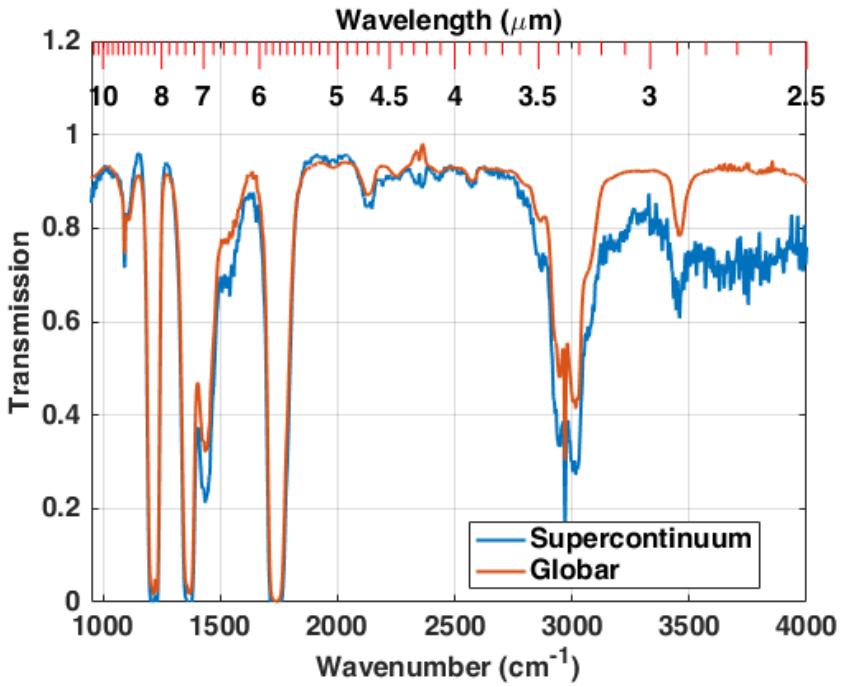


Figure 3.2: Comparison of transmission spectra using a blackbody source vs a SC source in a Michelson interferometer FTIR system of acetone gas.

Figure 3.2 shows the comparison between a gas cell measurement performed in the Michaelson interferometer. To perform these measurements, a scan is taken with a purged 10 cm path length gas cell. After the background scan, 50 µL of acetone is transferred to the gas cell and allowed to evaporate for 10 s before the scan begins. The gas cell needs to be removed between scans to purge the chamber for the next light source type and to add the volatile solvent. Unfortunately. the wedged windows of the gas cell cause slight beam deviations when the cell is replaced that correspond to baseline shifts in spectra.

These measurements show that although the commercial FTIR detection scheme is not optimized for pulsed sources, we are able to measure matching spectra with differing illumination sources as long as the we correctly attenuate the signal to within the linear regime of the HgCdTe detector.

## 3.4 Development of Standoff LWIR FTIR Sensor

After we have determined

### 3.4.1 SC source Parameters

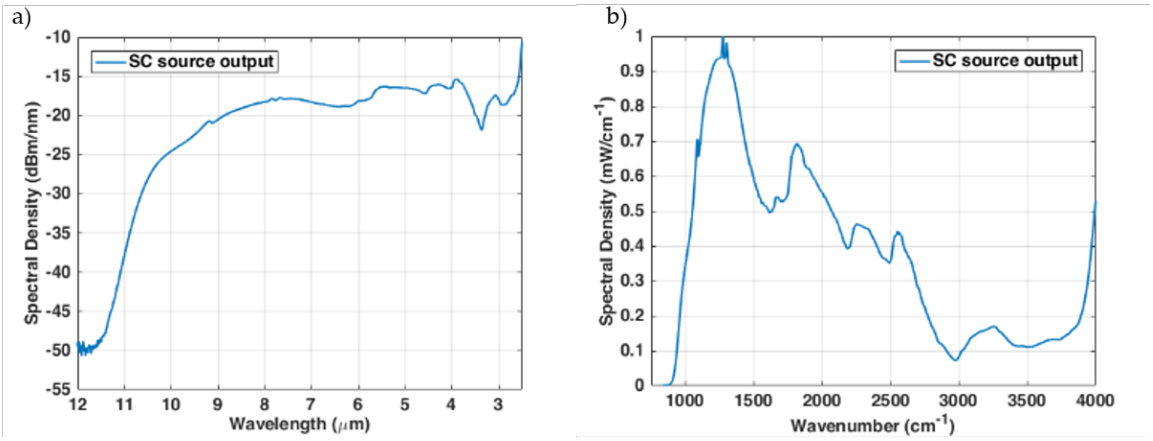


Figure 3.3: Spectral density of the SC source in (a) dBm/nm and (b) mW/cm$^{-1}$ at 300 kHz pulse repetition frequency.

The standoff LWIR FTIR sensor begins with the LWIR SC source. The LWIR SC source from Chapter II is run with 1.5 ns pulses emitted at a 300 kHz pulse repetition frequency and a 33% duty cycle, outputting an on-time power of 150 mW and 15 mW above 7.5 µm. A trigger signal from the FTIR spectrometer is used to modulate the SC source such that the source provides LWIR light only during the time when interferograms can be generated. The source outputs an electronic trigger signal with every optical pulse to trigger pulse acquisition. Fig. 3.3 the output

spectra of the LWIR SC source in dBm/nm and mW/cm$^{-1}$. Where the spectrum is relatively smooth in dB/m, because wavenumber and wavelength are inverses, the spectral density is much lower above 3000 cm$^{-1}$ in mW/cm$^{-1}$.

### 3.4.2 Turbo FT Interferometer

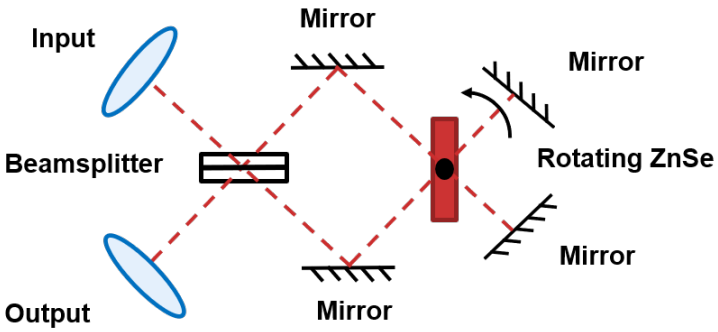


Figure 3.4: Block diagram depicting the beam path through the Turbo FT with a rotating ZnSe wedge generating the optical path difference between interferometer paths.

We use an FTIR interferometer to modulate the output from the LWIR SC source so that we can produce spectra from collected interferograms. The FTIR used in the testbed sensor (D & P Instruments, Inc. USA, Turbo FT), unlike traditional Michelson interferometer based FTIR spectrometers, utilizes a rotating window of ZnSe to create an optical path difference between separate interferometer arms. A block diagram of the beam path within the Turbo FT is shown in Fig. 3.4. Although the rotating slab of ZnSe introduces wavelength and angle dependent dispersion, this can be accounted for in the Fourier transform matrix described in section 3.4.4. The Turbo FT is chosen because it has a small form factor, has adjustable rotation speeds, is durable, and provides an optical throughput of up to 40% [18]. In this study, the ZnSe window rotates at 3.9 rev/s and produces 4 interferograms per revolution.

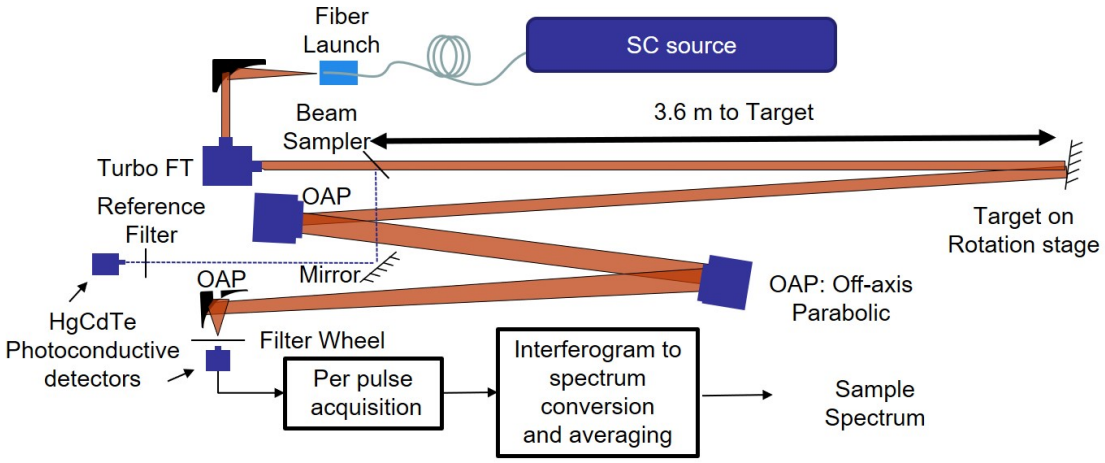


Figure 3.5: Schematic diagram of FTIR sensor actively illuminated by the collimated MW/LWIR SC source.

### 3.4.3 Testbed Sensor Optical Configuration

Fig. 3.5 depicts an overview of the testbed FTIR sensor. Light from the 1.6 - 11 µm SC source is collimated by an off axis parabolic mirror and directed into the Turbo FT. The modulated output from the FTIR is then split into reference (dotted line) and target paths (orange path). A broadband-coated ZnSe window placed after the output of the FTIR, samples ˜3% of the light and reflects it towards a pair of steering mirrors which guides the light through a hole in the final off axis parabolic mirror. The remaining target path light travels 3.6 m to hit scattering and specular return targets. The target arm return is collected using 3 off-axis parabolic mirrors. Two 6", 15° off-axis parabolic mirrors and a 4", 90° off-axis parabolic mirror, focus scattering or specular return onto a an optically immersed photoconductive HgCdTe detector (Vigo System S.A, POL, PCI-4TE-13) with a 1x1 $mm^2$ active area and detectivity, D* = 5.2 x $10^8$ cm$\sqrt{\text{Hz}}$/W. For standoff measurements, the scattered solid angle decreases with distance because of the finite size of the receiving optics. For 3.6 m, our receiving optics have a numerical aperture (NA) of approximately 0.0375.The reference arm spectrum is used to monitor variations in SC source output

or atmospheric conditions that may affect target spectra.

The optical configuration varies slightly for specular or scatter return measurements. For specular return samples, a 2" holographic wire grid on KRS-5 broadband polarizer (Thorlabs, Inc. USA, WP50H-K) is placed in the target path to act as a variable attenuator for the signal, and a 30 dB, NiCr on ZnSe, reflective neutral density filter (Thorlabs, Inc. USA, NDIR30A) is placed at the detector to further reduce the return signal to within the dynamic range of the detector. A Si wedge is used as a background for specular return measurements. For scattering samples, the broadband polarizer is removed to maximize the signal incident on the sample. 3 dB and 10 dB neutral density filters (Thorlabs, Inc. USA, NDIR03A, NDIR10A) are used to reduce the signal of high return samples to within the dynamic range of the detector. When samples produce a low return, the 10 dB filter is placed only in the reference arm to prevent reference arm saturation. A $BaF_2$ wedge with the 30 dB filter is used as a background for scattering measurements. The wedged background substrates return a spectrally flat, smoothly varying reflectance at ˜30% for Si and ˜3% for $BaF_2$ in the wavelength range of interest and reduce the risk of detecting back surface reflections.

To produce reflectance measurements, sample spectra are divided to their corresponding backgrounds and corrected for wavelength dependent neutral density filter absorption and background reflection. Fig. 3.6, shows the return spectra from an uncoated silicon wedge and a $BaF_2$ wedge used as backgrounds for specular and scattering samples, respectively. Most of the wavelength variation comes from the MW/LWIR SC source. The sharp features between 1250 - 2100 $cm^{-1}$ and above 3500 $cm^{-1}$ are from atmospheric water absorption lines and drop in signal at 2350 $cm^{-1}$ is caused by atmospheric $CO_2$. The figure also shows agreement between the different background reference substrates. The mechanical interfaces between dissimilar fibers will shift and change over time and cause variations in source and system

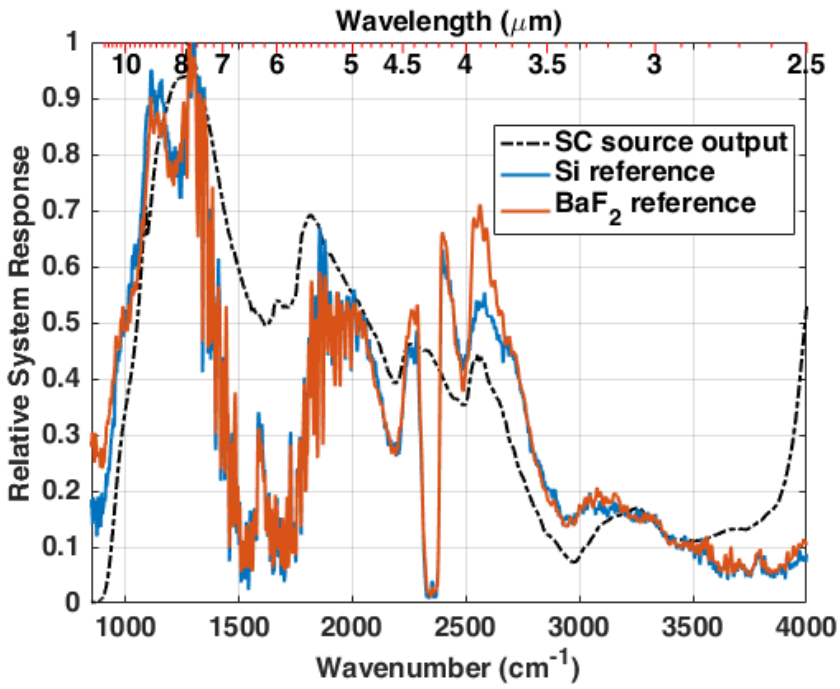


Figure 3.6: Normalized background spectra for Si and $BaF_2$ compared to the MW/LWIR SC source output in power/cm$^{-1}$.

calibration curves (such as Fig. 3.6) over time. The SC source output spectra may be stable for several weeks or months, but atmospheric and temperature variations can cause fibers to shift and spectral output to alter. System recalibration successfully mitigates these effects.

### 3.4.4 Testbed Sensor Signal Acquisition and Processing

An overview of the pulse processing is shown in Fig. 3.7. A pulsed acquisition schema is utilized where the SC source outputs an electronic signal with each optical pulse. This signal initiates the collection of the reference and target pulse pair on one analog-to-digital converter channel on a 2 channel, 12-bit, 2GS/s digitizer (Keysight Technologies, USA, U5303A). The pulses are separated in time by the difference in travel distance between the reference and target arms. The time difference can be utilized to estimate the range of the target. The second channel of the acquisition card collects the signal from an internal 850 nm reference diode located within the

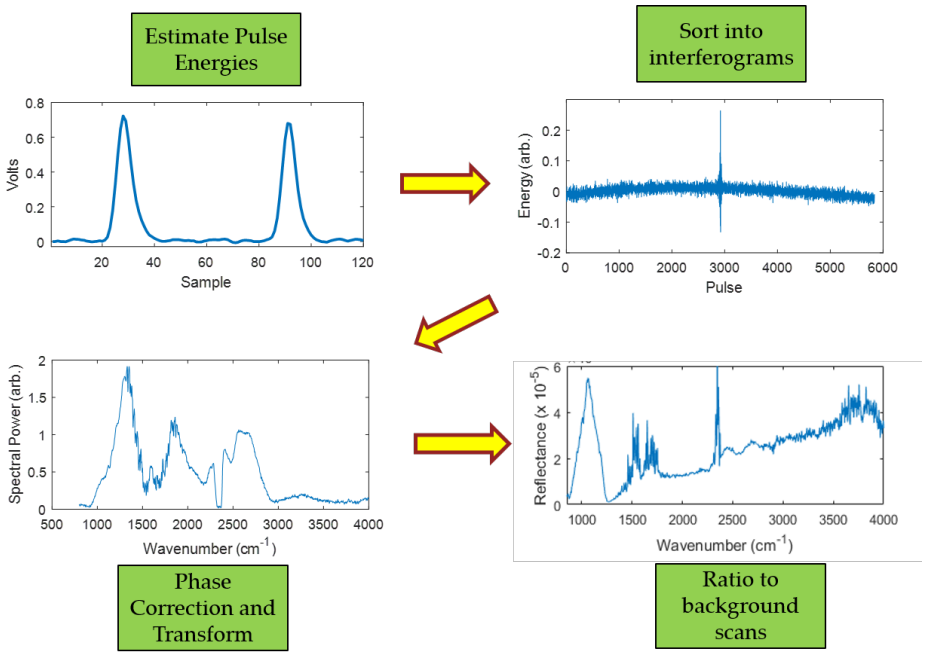


Figure 3.7: Overview of processing required to create spectra from the measurement of diffusely scattered pulses.

Turbo FT and is used to estimate the optical path difference of collected pulses.

Limits in sampling and electronic bandwidth prevent the direct measurement of pulse energy. Although the SC source outputs 1.5 ns optical pulses, distortion from multi-surface reflections and the 200 MHz preamplifier bandwidth of the detector result in ˜5 ns digitized pulses. The energy of each pulse is estimated by averaging the points measured along the pulse.

Pulses are recorded via triggered simultaneous acquisition and record. This collection mode places pulse data in a rotating memory buffer that allows for immediate retrieval, thus speeding our acquisition and minimizing the collection of incomplete interferograms. The data acquisition time to collect 1000 scans of ˜ 6000 pulse pairs is 69 seconds with an additional 40 seconds devoted to estimating pulse energy and transforming interferograms into sample spectra. These 1000 interferograms are separated by quadrant and aligned according to the position of their centerburst. A full Fourier transform matrix is applied to the interferograms by quadrant. Each term in

the matrix, $F(\tilde{v}, \alpha)$, is given by

$$F(\tilde{v}, \alpha) = e^{-i2\pi\tilde{v} \cdot OPD(\alpha, n(\tilde{v}))} \tag{3.1}$$

where $\tilde{v}$ and $\alpha$ are the wavenumber and rotation angle, respectively, and the optical path difference, $OPD(\alpha, n(\tilde{v}))$ is a function of the ZnSe angle and refractive index, $n(\tilde{v})$. The calculation of the energy spectrum follows the Mertz method [19], with triangular apodization and phase correction to account for the asymmetry of our interferograms. The resulting spectra from each quadrant are averaged together to form a final spectrum with a 4 $cm^{-1}$ resolution.

SC sources have been shown to have higher shot to shot variability compared to thermal emitters due to the high intensity pulses required to induce nonlinearities in nonlinear fibers [12, 13]. By averaging 1000 scans, the differences in pulse spectra that may result from modulation instability-initiated SC generation are mitigated.

### 3.4.5 Specular Measurements

Specular measurements are performed on thin film samples to verify the linearity of the SC FTIR based sensor. By matching the spectra to that derived from thin film theory we can be assured that the sensor does not suffer from nonlinear effects that can occur when high intensity pulses hit photoconductive HgCdTe detectors. These detectors are known to have a very small linear range, which can distort the interferogram near the centerburst pulses that are most important for spectrum generation. The targets measured in this study are 2 µm thick $SiO_2$ on a silicon wedge and 5.05 µm thick polyimide on a silicon wedge.

### 3.4.6 SC FTIR Measurements of Bulk and Gas Samples

Once we have verified that the SC source is suitable for FTIR based measurements in a commercial system and that the spectra that we create do not suffer from non-

linear effects, we can begin to use the SC FTIR sensor for scattering based stand-off measurements. For these measurements, we have several bulk samples that have been first measured with a handheld FTIR system that requires places the aperture directly on the surface of the sample. There will be slight differences in spectra because the illumination and collection optics of the handheld system have a relatively large numerical apertures compared to the standoff system. Specular scans have signals on the same order of magnitude as those of the background scans, but the scattering samples are 2-3 order of magnitude lower signal. Scattering magnitude will decrease with distance by a factor of $1/r^2$.

We also measure samples placed within a gas cell along the path. For these measurements, the 10 cm path length gas cell is placed along the beam path between the output of the FTIR spectrometer and before a gold scattering target. Because the windows of the gas cell are wedged ZnSe and the collection optics measure scattered return off of the gold scatterer, this is a single path measurement with a path length of only 10 cm, similar to that performed in the Michaelson interferometer. A background scan is measured with the purged gas chamber, then a target scan is measured after depositing 50 µL of acetone into the gas cell. The results are divided by the purged gas chamber scan and we create a transmission spectrum for the given gas.

## 3.5 Results

### 3.5.1 Testbed Sensor Specular Measurements

We verify the linearity of the testbed sensor by measuring the specular reflectance of thin films deposited on silicon wafers at 3.6 m. Fig. 3.8 shows specular measurements of a) a 2 µm layer of $SiO_2$ on a wedged silicon wafer and b) a 5.05 µm layer of polyimide on a wedged silicon wafer. The experimental results are compared to a thin film model derived from their refractive index values shown in Fig. 3.9 [20, 21].

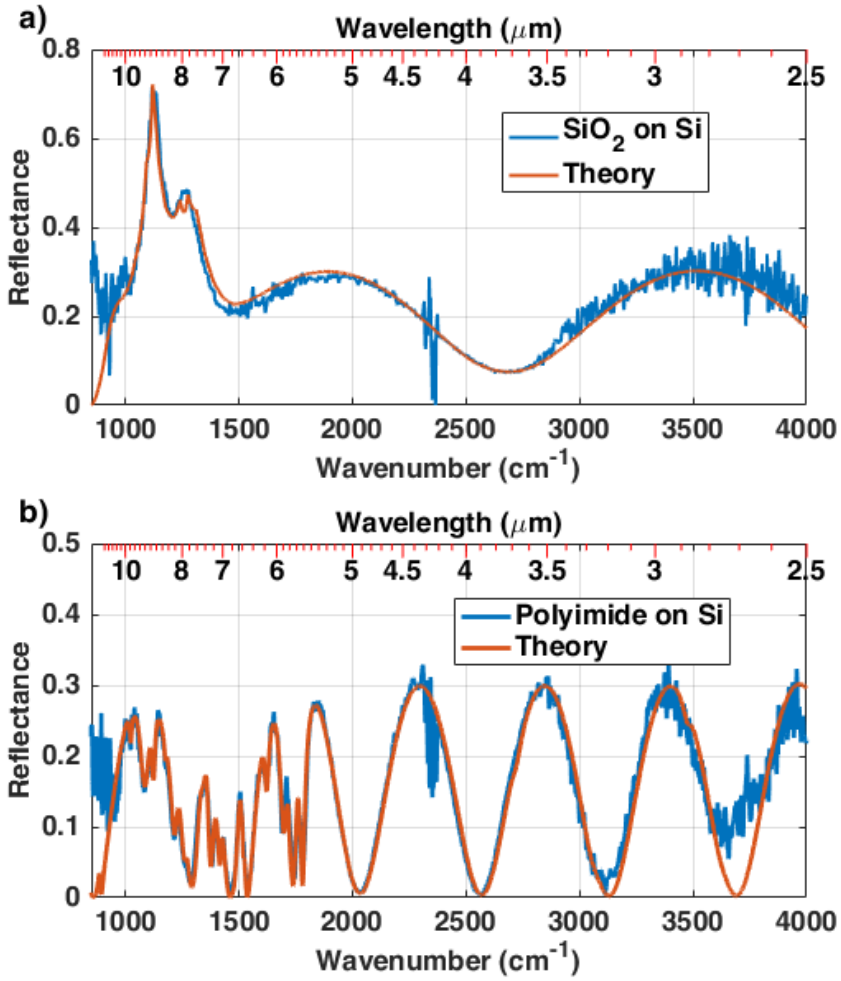


Figure 3.8: a) Specular return of a 2 µm layer of $SiO_2$ on a wedged silicon wafer and b) a 5.05 µm layer of polyimide on a wedged silicon wafer compared to theoretical prediction.

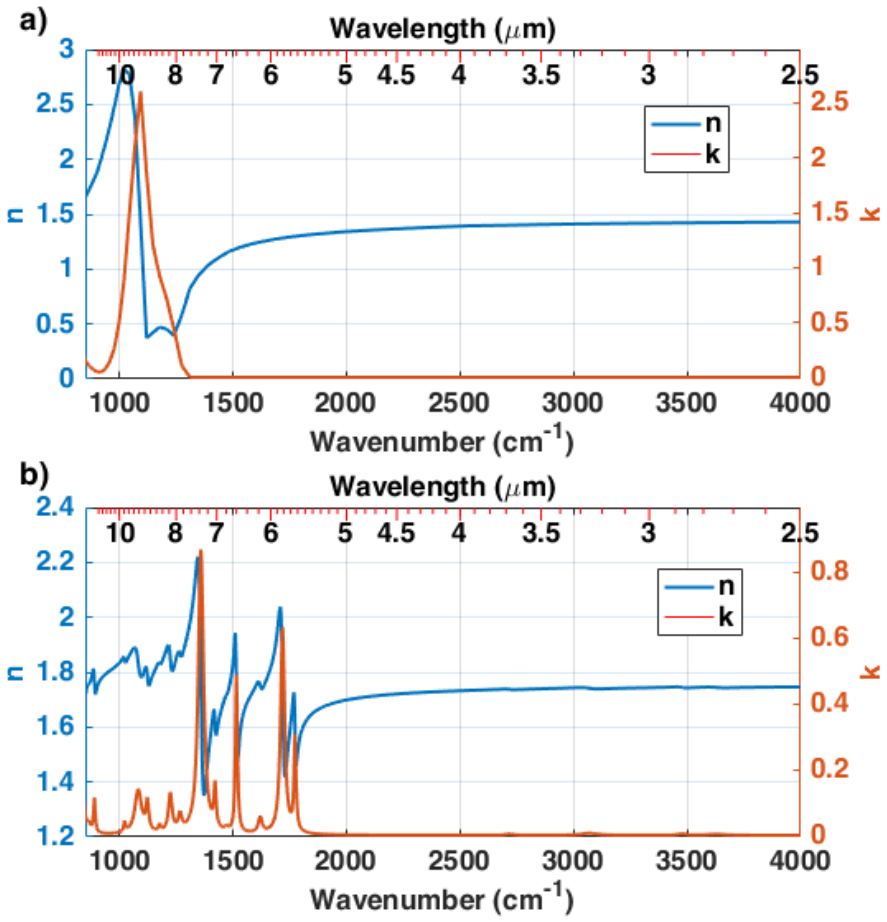


Figure 3.9: a) $SiO_2$ and b) polyimide refractive index n- and k- values for modeling thin film returns.

Although strong peaks caused by atmospheric $CO_2$ and $H_2O$ can be seen in the raw signal in Fig. 3.6, the lines ratio out and produce a small reduction in signal-to-noise ratio (SNR) in the reflectance spectra. Thicker samples provide more oscillations as expected from thin film interference. The fine features in the polyimide spectra are very well exhibited in measured spectra. Both reference and target scans required 30 dB attenuation to prevent overloading the detector.

### 3.5.2 Scattering from Bulk Materials

Figure 3.10 shows the SC FTIR measurements of (a) cardboard, (b) brick, (c) and canvas materials. There are slight differences in spectra that may be attributed to atmospheric effects and the small collection NA of the system. The brick spectra has the largest discrepancy between standoff measurement and commercial measurements. The absorption lines near 3000 $cm^{-1}$ are associated with $H_2O$ and so the clay brick may have absorbed some atmospheric water between measurements.

Wavelengths below the LWIR, above 1500 $cm^{-1}$ are prone to geometry related variations [22]. The backscattered spectra in the MWIR is likely to differ with collection and illumination optics. The handheld FTIR has a large illumination NA and a large collection NA, whereas the standoff sensor provides only a narrow illumination NA and a 0.0375 collection NA. The geometry related variations will average out in the handheld measurements and be much more pronounced in standoff measurements. The canvas sample likely has high agreement because of the woven nature of the surface, which will scatter along many different angles and average into a spectrum similar to high NA illumination and collection.

### 3.5.3 SC FTIR Sensor Gas Cell Measurements

We measure the transmission spectra of acetone gas that has been allowed to evaporate within a 10 cm path length gas cell and compare the resulting spectra to

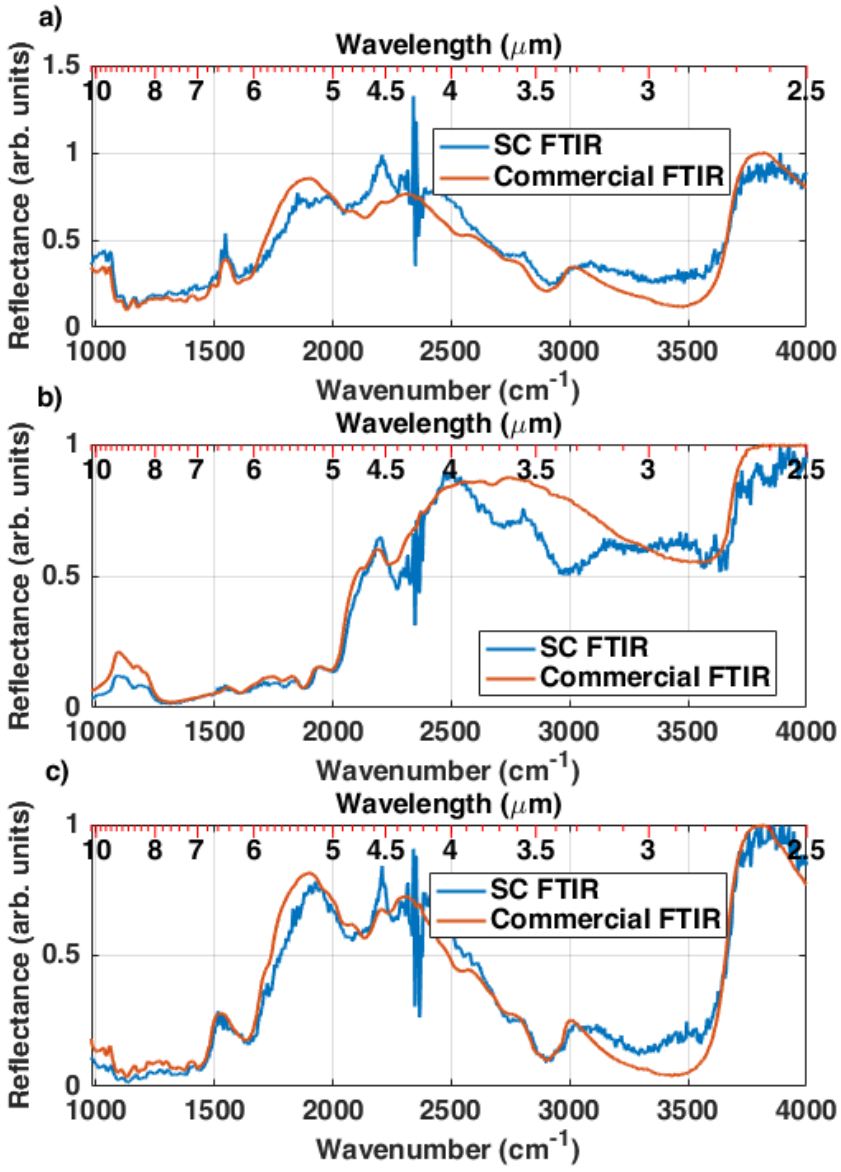


Figure 3.10: Bulk scattering from a) cardboard, b) brick, and c) canvas samples compared to the same samples measured with a commercial handheld FTIR system. Note atmospheric effects due to the long path length.

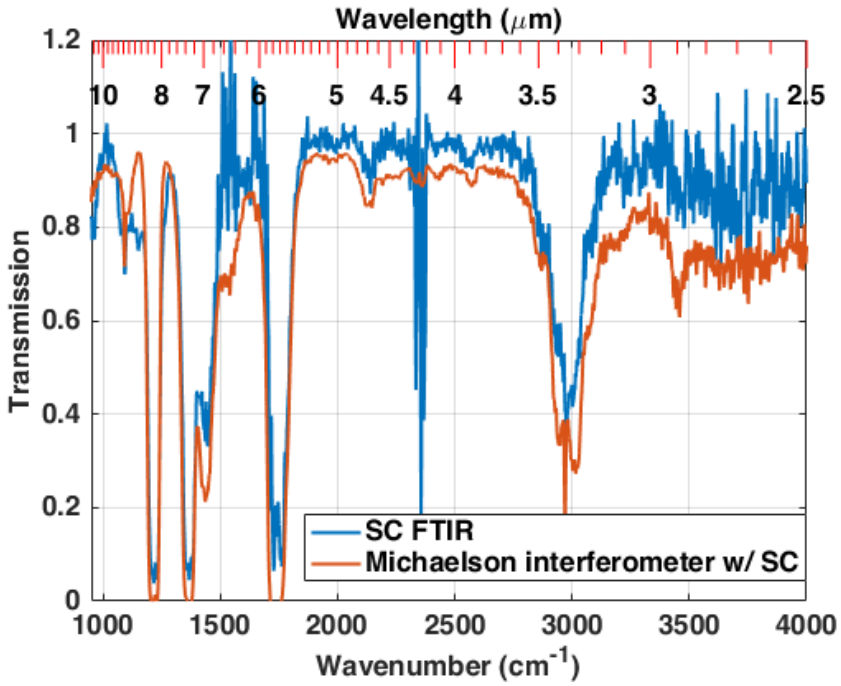


Figure 3.11: Acetone measurements from the SC FTIR based sensor measured from the diffuse reflectance off of a gold scatterer compared to Michaelson interferometer measurements.

that measured within a purged Michaelson interferometer. The noise of the resulting spectra in Fig. 3.11 is higher than that of the Michaelson interferometer because of atmospheric effects. Atmospheric water increases the noise from 1450 - 1700 cm$^{-1}$ and atmospheric $CO_2$ increases noise near 2350 cm$^{-1}$.

## 3.6 Discussion

### 3.6.1 Atmospheric and Source Contributions to Noise

Although Fig. 3.6, shows strong water absorption (1250 - 2100 cm$^{-1}$ and above 3500 cm$^{-1}$) and $CO_2$ absorption (near 2350 cm$^{-1}$) lines, the spectra in Fig. 3.8 exhibit minimal noise in the water bands. This shows that the testbed sensor factors out atmospheric effects in high return samples. As long as there are no significant atmospheric fluctuations, a single background scan can serve as the reference for a

day's worth of target measurements.

The LWIR SC source seems to stay relatively stable while in operation. If the purging between fibers is lost for any reason, the long-wavelength edge of the spectra will begin to decrease to a point that can become unusable. We use the reference arm spectra to monitor the long wavelength edge of the source and if any significant loss is seen, the laser is powered down and analyzed for alignment and purging. The long wavelength edge decreasing between power cycles is a more often occurrence which happens in the tube-on-groove system. The spectra may decrease because a large flux of photons upon hitting an unpurged $As_2S_2$ face may heat the surface and cause imperfections on the fiber face.

The LWIR SC source provides relatively low signal above 3000 $cm^{-1}$. This is evidenced by a lower signal to noise ratio in this regime. The discrepancy comes from the differences in spectral density when converting from dBm/nm to $mW/cm^{-1}$. A given response in mW/nm will have a $1/wn^2$ scaling factor in the $mW/cm^{-1}$ scale.

### 3.6.2 Background Scans and Calibration

Using specular return for background requires precise alignment for the initial background scans, followed by adjustment to an off specular angle of choice. To prevent this originally, a gold scattering target was used for the background scan to decrease the angular dependence of the return. Unfortunately, this did not work well because the gold scatterer has sharp features that are difficult to ratio out and may shift with angle. Figure 3.12 shows the ratio between a silicon scan and a gold reference scan. Specifically, the features in the molecular fingerprint regime between 980 $cm^{-1}$ and 1800 $cm^{-1}$ would disrupt any chemical reflectance lines that may be useable for chemical identification. Unfortunately, using a wavelength-based conversion from gold scatterer to silicon did not always provide reliable results because gold scattering magnitudes may shift as different parts of the roughened substrate are

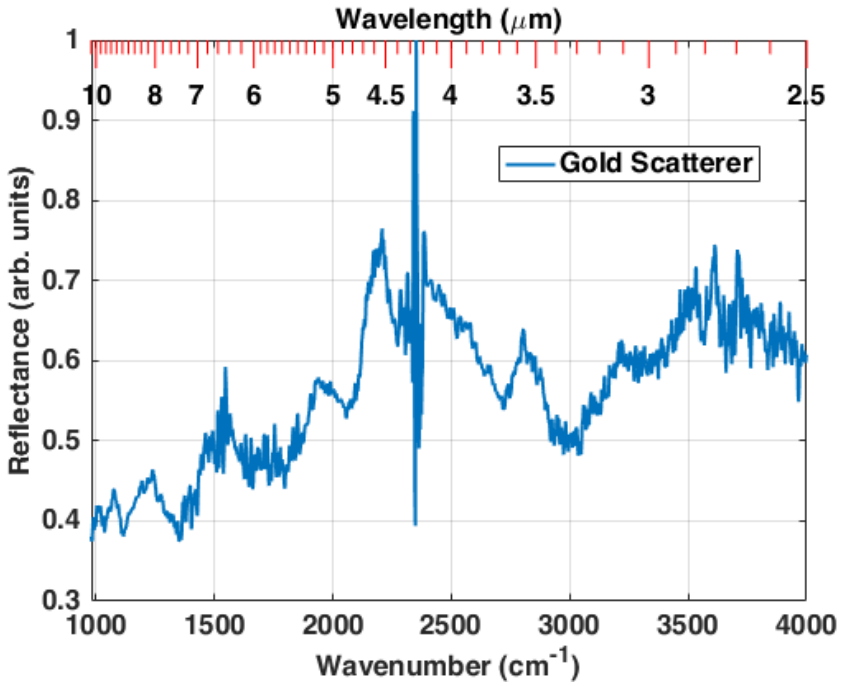


Figure 3.12: Gold scattering return when divided by the specular return of a Si wafer.

illuminated.

### 3.6.3 Speed Scalability

The acquisition time for a single run in the testbed system is determined by the number of scans per run and spin rate of the Turbo FT. The acquisition time of 69 seconds can be decreased by a multiplicative factor while maintaining similar performance by increasing the spin rate of the Turbo FT and the pulse repetition frequency of the SC source by that factor. This study is limited to a 300 kHz pulse repetition frequency from the SC source by the data transfer speed from the acquisition card to system memory, but custom electronics and adjustments to the acquisition script can prevent this bottleneck. With a maximum SC source pulse repetition frequency of 800 kHz, the 69 s acquisition time could be dropped to 26 s for 1000 scans and potentially lower if fewer scans are needed. Furthermore, if the estimation of pulse energy can be made to occur before data transfer, this would reduce amount of data

transferred by an order of magnitude and reduce the 40 s processing time accordingly.

If a shorter wavelength range is required, the acquisition speed can be increased by another factor of 2. Currently, over 6000 pulses are collected to create each interferogram and maintain a 4 $cm^{-1}$ resolution and spectra down to 2.5 µm. As will be shown in the next chapter, it may be only necessary to measure spectra to 5 µm or 2000 $cm^{-1}$. In this case, we would only need 3000 pulses over the interferogram and could increase the rotation speed of the rotor by a factor of 2 without losing resolution or SNR. This may even prove to be more stable as there should be less wobble in the rotor shaft at higher speeds.

### 3.6.4 Turbo FT Internal Alignment

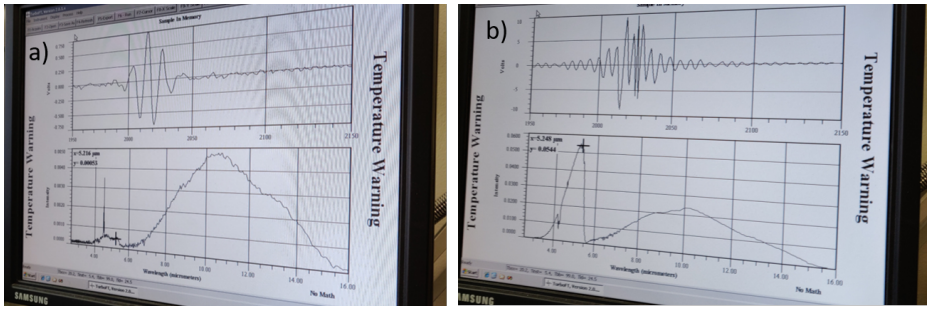


Figure 3.13: Interferogram and blackbody spectra (a) prior to and (b) after FTIR mirror realignment

Over the course of my work, we found that there was a source independent loss of the short wavelength edge of the LWIR SC spectrum when measured with the FTIR-based sensor. Measurements with a grating monochromator did not show the same loss of spectrum. We found that the short wavelength edge of the spectrum is most sensitive to mirror misalignments within the FTIR. Fig. 3.13 shows the extent of the misalignment by illustrating a spectrum and interferogram taken of a blackbody source prior-to and after mirror alignment. Misalignment to the FTIR system may have occurred during shipping or by accidental rotation of the hubcaps that control mirror tilt.

The four interferograms produced per revolution transform into slightly different spectra. Though the differences are minimal, they are significant enough for single scans that each quadrant should be averaged independently before averaging into the total signal. Spectra created using a single quadrant produce noisier spectra at low signal locations. The advantages of averaging the quadrants together outweigh the slight differences in quadrant spectra. The differences in spectra can be compensated for by performing calibration scans with standardized PS samples that are commercially available with spectra measured by National Institute of Standards and Technology.

### 3.6.5 The Impact of Target Distance on Signal-to-Noise Ratio

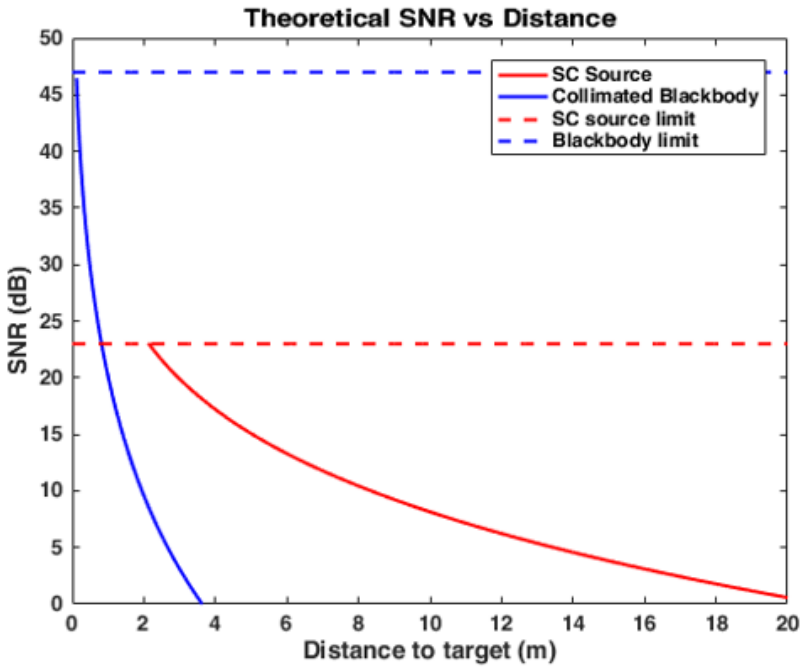


Figure 3.14: Decrease in SNR for a blackbody source vs that of the LWIR SC for collimated beams assuming a scattering dependence of $1/r^2$.

From the measurements performed in this chapter, we can develop a model for the decrease in SNR compared to the distance to a given target with average reflectance. For high return samples, the signal hitting the detector must be attenuated to prevent

nonlinearites in the HgCdTe detector. This along with pulse-to-pulse variations in MI initiated sources limits the SNR of the SC source to 23 dB for the collection parameters described in Section 3.4.4. In a commercial FTIR system, the scan parameters and optics have been optimized to provide SNRs of at least 47 dB. If we assume a $1/r^2$ dependence on the scattered return from the target and use the illumination intensities shown in Fig. 2.7, the theoretical decrease in SNR over distance can be derived as shown in Fig. 3.14.

With the SNR limit caused by the SC source and detector limits, a collimated blackbody source would provide higher SNR spectra for targets within 1.6 m, beyond this range, the near-diffraction limited beam properties of the LWIR SC source provide much higher illumination intensity and therefore SNR.

## 3.7 Summary

The LWIR SC source can be used in traditional FTIR systems despite the 1.5 ns pulses breaking up into solitons that vary pulse to pulse. We find that we can measure transmission spectra from gases and through samples in commercial systems, even though the detection schema is not optimized for these measurements. We demonstrate a testbed sensor that collects specular and diffusely scattering spectra from thin film coated and bulk samples at 3.6 m. The high beam quality of the SC source can allow for standoff measurements at up to 5 m in the lab setting but can theoretically measure scattering samples much further. With its directionality, high brightness, and scalable acquisition time, the SC illumination based FTIR sensor is suitable for standoff gas and bulk scattering measurements.

## References


[1] Peter R Griffiths and James A De Haseth. *Fourier transform infrared spectrometry*, volume 171. John Wiley & Sons, 2007.

[2] Kevin C Gross, Kenneth C Bradley, and Glen P Perram. Remote identification and quantification of industrial smokestack effluents via imaging fourier-transform spectroscopy. *Environmental science & technology*, 44(24):9390–9397, 2010.

[3] RH Wilson and HS Tapp. Mid-infrared spectroscopy for food analysis: recent new applications and relevant developments in sample presentation methods. *TrAC Trends in Analytical Chemistry*, 18(2):85–93, 1999.

[4] Ulrike Willer, Mohammad Saraji, Alireza Khorsandi, Peter Geiser, and Wolfgang Schade. Near-and mid-infrared laser monitoring of industrial processes, environment and security applications. *Optics and Lasers in Engineering*, 44(7):699–710, 2006.

[5] Mark L Polak, Jeffrey L Hall, and Kenneth C Herr. Passive fourier-transform infrared spectroscopy of chemical plumes: an algorithm for quantitative interpretation and real-time background removal. *Applied optics*, 34(24):5406–5412, 1995.

[6] Roland Harig. Passive remote sensing of pollutant clouds by fourier-transform infrared spectrometry: signal-to-noise ratio as a function of spectral resolution. *Applied Optics*, 43(23):4603–4610, 2004.

[7] David A Kirchgessner, Stephen D Piccot, and Ajay Chadha. Estimation of methane emissions from a surface coal mine using open-path ftir spectroscopy and modeling techniques. *Chemosphere*, 26(1-4):23–44, 1993.

[8] Zhaowei Zhang, Rhea J Clewes, Christopher R Howle, and Derryck T Reid. Active ftir-based stand-off spectroscopy using a femtosecond optical parametric oscillator. *Optics letters*, 39(20):6005–6008, 2014.

[9] HD Tholl, F Münzhuber, J Kunz, M Raab, M Rattunde, S Hugger, F Gutty, A Grisard, C Larat, D Papillon, M Schwarz, E Lallier, M Kastek, T Piatkowski, F Brygo, C Awanzino, F Wilsenak, and A Lorenzen. Active multispectral reflection fingerprinting of persistent chemical agents. In *Electro-Optical Remote Sensing XI*, volume 10434, page 104340C. International Society for Optics and Photonics, 2017.

[10] Christopher J Breshike, Christopher A Kendziora, Robert Furstenberg, Viet Nguyen, Andrew Kusterbeck, and R Andrew McGill. A system for rapid chemical identification based on infrared signatures. In *Micro-and Nanotechnology Sensors, Systems, and Applications X*, volume 10639, page 1063927. International Society for Optics and Photonics, 2018.

[11] Christopher J Breshike, Christopher A Kendziora, Robert Furstenberg, Viet Nguyen, Andrew Kusterbeck, and R Andrew McGill. Using infrared backscatter imaging spectroscopy to detect trace explosives at standoff distances. In *Chemical, Biological, Radiological, Nuclear, and Explosives (CBRNE) Sensing XIX*, volume 10629, page 106290N. International Society for Optics and Photonics, 2018.

[12] Chris A Michaels, Tony Masiello, and Pamela M Chu. Fourier transform spectrometry with a near-infrared supercontinuum source. *Applied spectroscopy*, 63(5):538–543, 2009.

[13] Vasily V Goncharov and Gregory E Hall. Supercontinuum fourier transform spectrometry with balanced detection on a single photodiode. *The Journal of chemical physics*, 145(8):084201, 2016.

[14] F Borondics, M Jossent, C Sandt, Laure Lavoute, Dmitry Gaponov, Ammar Hideur, Paul Dumas, and S Février. Supercontinuum-based fourier transform infrared spectromicroscopy. *Optica*, 5(4):378–381, 2018.

[15] Bin Zhang, Yi Yu, Chengcheng Zhai, Sisheng Qi, Yuwei Wang, Anping Yang, Xin Gai, Rongping Wang, Zhiyong Yang, and Barry Luther-Davies. High brightness 2.2–12 $\mu$m mid-infrared supercontinuum generation in a nontoxic chalcogenide step-index fiber. *Journal of the American Ceramic Society*, 99(8):2565–2568, 2016.

[16] Kaiwen Guo, Ramon A Martinez, Genevieve Plant, Lukasz Maksymiuk, Brian Janiszewski, Michael J Freeman, Robert L Maynard, Mohammed N Islam, Fred L Terry, Robert Bedford, Ricky Gibson, Francois Chenard, Stephane Chatigny, and Agustin I Ifarraguerri. Generation of near-diffraction-limited, high-power supercontinuum from 1.57 $\mu$m to 12 $\mu$m with cascaded fluoride and chalcogenide fibers. *Applied optics*, 57(10):2519–2532, 2018.

[17] Ramon A Martinez, Genevieve Plant, Kaiwen Guo, Brian Janiszewski, Michael J Freeman, Robert L Maynard, Mohammed N Islam, Fred L Terry, Oseas Alvarez, Francois Chenard, Robert Bedford, Ricky Gibson, and Agustin I Ifarraguerri. Mid-infrared supercontinuum generation from 1.6 to >11 $\mu$m using concatenated step-index fluoride and chalcogenide fibers. *Optics letters*, 43(2):296–299, 2018.

[18] Winthrop Wadsworth and Jens-Peter Dybwad. Rugged high-speed rotary imaging fourier transform spectrometer for industrial use. In *Vibrational Spectroscopy-based Sensor Systems*, volume 4577, pages 83–89. International Society for Optics and Photonics, 2002.

[19] Avishai Ben-David and Agustin Ifarraguerri. Computation of a spectrum from a single-beam fourier-transform infrared interferogram. *Applied optics*, 41(6):1181–1189, 2002.

[20] Rei Kitamura, Laurent Pilon, and Miroslaw Jonasz. Optical constants of silica glass from extreme ultraviolet to far infrared at near room temperature. *Applied optics*, 46(33):8118–8133, 2007.

[21] ZM Zhang, G Lefever-Button, and FR Powell. Infrared refractive index and extinction coefficient of polyimide films. *International journal of thermophysics*, 19(3):905–916, 1998.

[22] Robert Furstenberg, Andrew Shabaev, Christopher A Kendziora, Christopher Breshike, Tyler J Huffman, Andrew Kusterbeck, Dawn Dominguez, Samuel G Lambrakos, and R Andrew McGill. Synthetic models for infrared reflectance signatures of micro-particle traces on surfaces. In *Chemical, Biological, Radiological, Nuclear, and Explosives (CBRNE) Sensing XX*, volume 11010, page 110100K. International Society for Optics and Photonics, 2019.

# CHAPTER IV

# Scattering From Sparse Particles on Smooth Surfaces Illuminated With a LWIR SC and FTIR Source

## 4.1 Introduction

This chapter of the dissertation focuses on the factors required for trace chemical identification from spectra measured by the sensor described in Chapter III. This problem is complex because real-world targets will contain a collection of non-spherical particles of varying sizes that can each exhibit different return spectra based on their size and chemical composition that will be modified by the optical characteristics of the substrate that the particles are lying on. Chemical identification is further complicated because different samples of the same chemical may exhibit disparate spectra based on the particle size distribution inherent to that sample. In this chapter, we use a Bobbert-Vlieger (BV) model to simulate particle and substrate effects on diffuse reflectance spectra, examine the effects of changes to simulation parameters on diffuse reflectance spectra, and weigh the single particle solutions with log normal distributions to fit measured spectra. We show that despite simulating non-spherical powders as spheres, the BV model can accurately fit experimentally measured spectra on glass, down to a concentration of 6.5 µg/cm$^2$. Our model can

account for changes in spectra based on real-world changes such as variations in particle size distribution and substrate effects. We can identify an unknown chemical on aluminum using solely using a library of simulated spectra with step-generated particle size distributions.

To perform chemical identification in light of the challenges mentioned above, we develop a library of BV simulated spectra with step-wise varying particle size distributions. The spectra that we simulate with BV theory accounts for reflectance changes caused by smooth substrates and can be used to accurately predict the identity of an unknown chemical that has been deposited on aluminum. In this chapter, we illustrate a model that can account for the variation in particle sizes and substrate effects that complicate real-world sample measurements. Further work is required to model the effects of a roughened background, but the work depicted here can provide a stepping stone for future measurements and models.

## 4.2 Motivation & Background

Standoff detection of chemicals in the long-wave infrared (7 - 14 µm) (LWIR) has become useful in many applications because most chemicals have a unique signature in the molecular fingerprint regime (3 - 12 µm. Previously, a lack of spatially coherent light sources has led to FTIR based standoff detection in the LWIR to rely on retroreflecting elements to examine gas signatures [1] or passive sensing using temperature differences [2, 3]. Recent advances in supercontinuum (SC) sources and quantum cascade lasers (QCL) that extend into the LWIR have made illuminated standoff chemical sensing and identification possible [4–7]. SC and QCL sources have spatially coherent outputs that can be transmitted long distances at high incident intensity. This is necessary as the strength of the scattered return diminishes with distance and is already found to be 4-5 orders of magnitude lower than incident light at 3.6 m [8].

Standoff detection methods utilize QCL or SC sources that emit in the mid-wave infrared (2.5 - 7 µm) (MWIR) and LWIR to probe targets via photoacoustic spectroscopy, photothermal spectroscopy, or backscattered reflectance [9, 10]. Photoacoustic spectroscopy involves illuminating samples with infrared energy to induce thermal expansion and create pressure waves that can be measured acoustically. This method works best in sealed environments and may be limited in open air environments where the effect may be masked by ambient noise levels [10]. Likewise, in photothermal spectroscopy, sample temperature changes of ˜1 K are measured via HgCdTe detectors and microbolometer arrays when targets are illuminated with QCLs at absorption wavelengths in the MWIR [11, 12].

Backscattered reflectance techniques directly measure scattered light that interacts with both the chemical and underlying substrate. It is of particular interest to measure scattered spectra from trace particles laying on top of various background substrates. The size of particles that are left behind in fingerprints or airborne particles that come to rest on different surfaces are on the same order as illumination wavelengths in the MWIR to LWIR [13]. Therefore, reflectance spectra from these sparse particles will vary with respect to particle size and will not exhibit the same features as bulk sample absorption or reflection spectra measured with traditional FTIR systems [8, 14, 15]. One of the major challenges in identifying unknown chemicals on surfaces is that Mie scattering effects cause shifts in absorption and reflectance peaks that vary with respect to particle size. This means that real world targets of the same chemical will manifest different spectra that depend on the specific particle size distribution that is found on its surface.

Previous studies used Mie scattering and substrate bulk reflectance to model experimental return from particles on surfaces. This model works well for substrates with smoothly varying refractive index profiles but does not accurately portray the effects that the substrate has on return spectra [15]. Furthermore, this trans-reflection

model does not account for illumination and collection optics that impact spectra in the MWIR where there are geometry related variations.

Recent studies have utilized external cavity QCLs and cameras to scan across wavelengths and create hypercube images of backscattered reflectance spectra [16, 17]. The fraction of backscattered energy from the particle and surface effects at a near-normal incidence approximation [18] is added to the diffuse reflectance signature of a blank substrate to analyze scattered return from sparsely loaded surfaces that also scatter light. The near-normal incidence approximation (Videen approximation) is an assumption applied to the Bobbert-Vlieger model utilized in our studies. Furstenberg et al. also average the returns across the backscattered hemisphere to produce theoretical spectra [16].

In our study, we simulate spherical particles on a substrate using the BV model [19]. The BV model incorporates incident angle, collection angle, and particle distribution to predict scattering return spectra from trace particles on smooth substrates [8, 20], and produces spectra that show features that are not available when applying the Videen approximation, such as oscillatory spectra caused by narrow particle size distribution samples.

## 4.3 Examination of Sample Characteristics with Confocal and FTIR Microscopy

### 4.3.1 Sample Preparation and Characteristics

Two categories of targets are measured in this study: monodisperse spherical particles on aluminum and non-spherical powders deposited on various substrates. Mono-disperse particle targets are created to verify BV theory. Mono-disperse particle size samples are created by vapor spray deposition of 5.9, 10.8, and 19.5 µm polystyrene (PS) microspheres (Microspheres-Nanospheres, USA, C-PS-5.0, C-PS-

10.0, C-PS-20.0) on 1" x 1" aluminum substrates. Non-spherical scattering samples are created to mimic samples that can be found in real world conditions. These samples are created by the U.S. Naval Research Laboratory via sieve deposition of 1,3,5-Trinitroperhydro-1,3,5-triazine (RDX), caffeine, or N-acetyl-para-aminophenol (acetaminophen/paracetamol) powder on 1" x 1" smooth glass, aluminum, silicon, or soda-lime glass substrates [13]. Sieve deposition limits the particle size to below 30 µm in diameter. The samples exhibit isolated particles of varying sizes and a low overall fill factor. Concentrations are determined by image analysis of particle micrographs. Sample concentrations range between 0.2 and 50 µg/cm$^2$.

The chemicals and substrates included in this study are chosen to exemplify different scenarios that this type of sensor might be of use such as scanning shipping containers, vehicles, or silicon wafers for various contaminants, while distinguishing between dangerous and innocuous chemicals, such as caffeine. Furthermore, aluminum and silicon have relatively smooth reflectances in the LWIR to emphasize chemical effects on reflectance. Glass is included because it exhibits distinct bulk reflectance features that are apparent in standoff measurements.

### 4.3.2 Microscopic Analysis

Microscopic images of samples and FTIR reflective microscopic measurements are performed with a commercial FTIR with a globar source (Agilent, Cary 620 FTIR Microscope). In these measurements, the receiving aperture is reduced to ˜40 x 40 µm to examine the return from single particles or clusters to better understand the effects of particle size and shape when examining backscatter from particulate matter on a smooth substrate. The FTIR microscope illuminates and collects return over a range of 20° - 38°, so these measurements will not exhibit angular dependent effects of diffuse scattering.

Images of samples are obtained using conventional microscopy and laser confocal

microscopy to examine particle size and shape. Though particles are crystalline in nature, image processing allows the estimation of the volume of a given particle. Spherical particles with radii set to match the volume of a given particle are used to guide the idealized particle size distribution used in BV analysis.

### 4.3.3 FTIR and Confocal Microscope Measurements

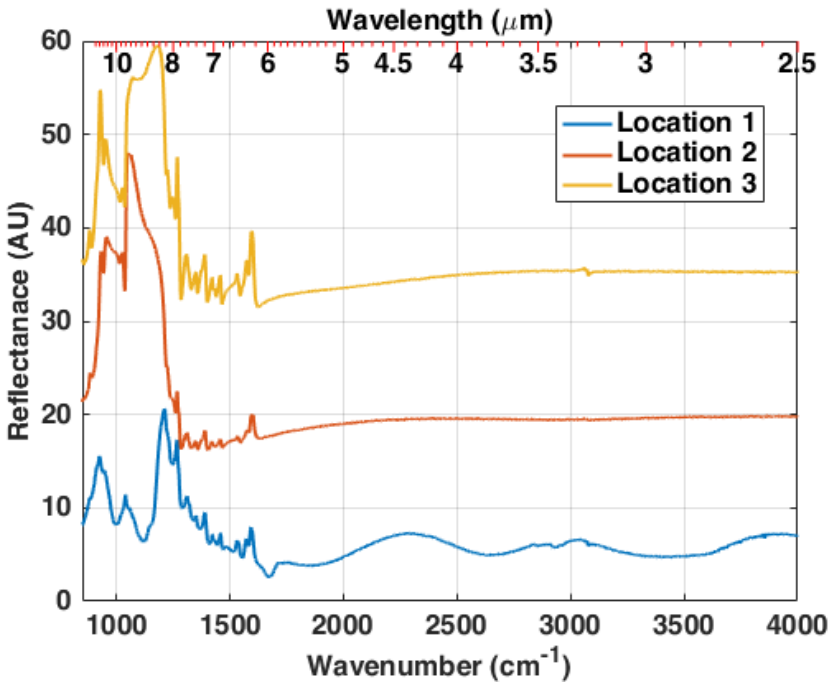


Figure 4.1: Commercial FTIR reflective microscopy of different locations of RDX particles on glass at 35.46 µg/cm$^2$. Particles measured with a ˜40 x 40 µm$^2$ aperture. Spectra are offset for clarity.

Fig. 4.1 shows the return spectra of different locations on a 35.46 µg/cm$^2$ RDX sample using a commercial globar illuminated FTIR reflection microscope. Although all of these spectra are taken from the same sample, the scattered return can vary depending on the size of the particle or differences in particle cluster. The microscope collects light over a broad range of angles, reducing spectral effects that may be angle dependent.

Microscopic images of a sample of acetaminophen at a concentration of 41.77

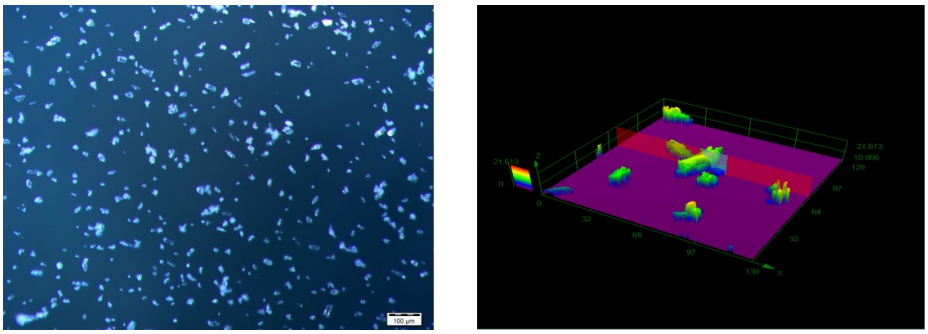

Figure 4.2: (Left) Conventional microscope image of acetaminophen deposited on a glass substrate at a concentration of 41.77 µg/cm$^2$. Particles are crystalline and non-spherical. (Right) 3D mapping of acetaminophen particles show a measurable particle size to use for BV modeling.

µg/cm$^2$ are shown in Fig. 4.2. 3D mapping using a laser confocal microscope is used to estimate particle sizes. As can been seen in Fig. 4.2, some particles aggregate after sieving and clumping leads to larger scattering sites than from individual particles. Although the particles seen in the images are crystalline in structure, we estimate the particle shapes as spherical to ease computation in the BV model. The results of microscopic analysis guide the parameters of the log-normal used to weigh the theoretical model in Section 4.5.2 but are not necessary for unknown trace chemical identification as spectra are created from arbitrary particle size distributions.

## 4.4 Bobbert-Vlieger Modeling

### 4.4.1 Modeling Overview

Testbed sensor acquired scattering spectra are modeled by numerical solutions of the BV model of light scattering off a spherical particle on a flat substrate. The effects of particle size distribution, chemical response, and substrate reflectivity are all included in the BV model. Mie scattering states that particle size and shape change the relative amount of forward and backscattering as a function of wavelength [21]. The substrate that the particles are deposited on changes the electromagnetic bound-

ary conditions compared to free space Mie scattering. The BV model reduces this problem to the scattering by a sphere in a homogeneous medium and that of the reflection of spherical waves by the substrate. It then solves this using Mie theory and the propagation of dipole radiation along a flat surface [19]. We use the National Institute of Standards Technology (NIST) modeled integrated scatter tool (MIST) and SCATMECH C++ library to compute the effects of target chemical, substrate, angle of incidence, and collection angle on the scattering spectra of spherical particles near a smooth surface [22, 23].

Experimental samples have a distribution of particle sizes including diameters of up to 50 µm. To allow adequate convergence of the BV algorithms for large particle diameters, the NIST SCATMECH code are modified to use long double (80 bit) floating point numbers. For each particle, substrate, incident and collection angle combination, BV simulations are run and stored for particle radii from 0.1 to 25 µm in 0.1µm steps.

### 4.4.2 Refractive Index Data and Sources of Error for Input Parameters

To simulate particle on surface effects with the BV model, we must first have accurate refractive index data that can be measured from FTIR transmission data performed on bulk samples or KBr pellets. Figure 4.3 shows the complex refractive indices for the RDX, acetaminophen, and caffeine tested in this study. The data for these chemicals are provided by Pacific Northwest National Laboratory and U.S. Naval Research Laboratory where the complex refractive indices are determined from FTIR transmission measurements of KBr pellets. The transmission spectrum of a given chemical that has been diluted with KBr and pressed into a pellet is converted into an absorption spectrum and the effective thickness of the sample is used to determine the imaginary refractive index, k. The real refractive index, n, is determined via the Kramers-Kronig relation, and assumed to have a baseline value, $n_\infty = 1.5$ [24].

The refractive index data used to model the polystyrene microspheres were determined from KBr pellets created from polystyrene powders measured by the U.S. Naval Research Laboratory and have a higher purity than targets created from the polystyrene microspheres.

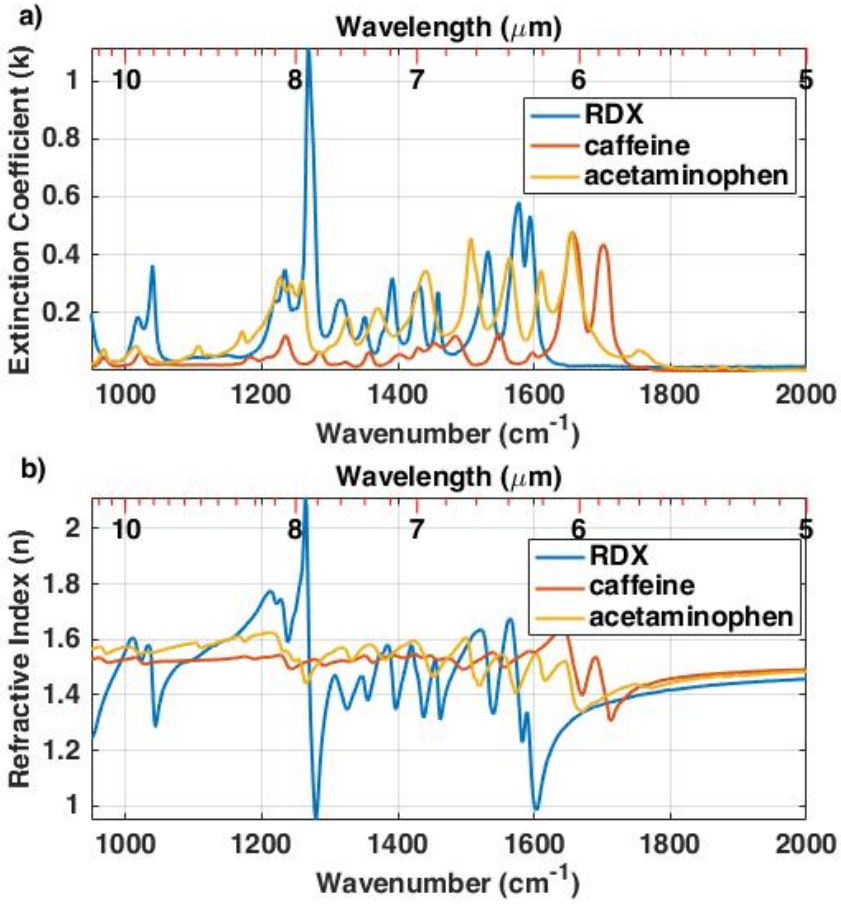


Figure 4.3: (a) Extinction coefficient and (b) refractive index for RDX, caffeine and acetaminophen utilized in BV simulations.

During the course of this study, we have found that the complex refractive index for a given chemical can vary based on how the original absorbance data is measured. Any errors in the absolute absorbance measurements will translate to errors in the magnitude of the extinction coefficient and refractive index. The assumption typically made during these measurements is that the $n_\infty$ value is 1.5 for unknown materials. While, this assumption is generally true, there may be instances where deviations

from the norm will cause deviations in the magnitude of the reflected signal and shifts in reflectance peaks as seen in Fig.4.15.

Aside from baseline differences in $n_\infty$, absorbance spectra measured from different suppliers of the same chemical may vary drastically. These variations will be a limitation to spectra created via BV modeling as trace particulates may have different refractive index profiles from those measured in bulk material or KBr pellets. Differences in the complex refractive indices may arise from the hydroscopic nature of some powders or through contamination associated with how the chemicals are deposited on a given surface. This is most apparent in Fig. 4.8, where the microspheres contain features associated with water contamination and UV degradation that are not modeled in the pure PS powder. It would be beneficial to perform further research on methods to determine the refractive index directly from scattering return measurements. The reliability of data measured in these bulk and pellet samples is critical to accurately modeling the particle effects using BV theory and further work is required to determine the differences in purity that may cause real-world powders to vary from uncontaminated chemicals.

### 4.4.3 BV Model Solutions and Transreflection

Different size particles will cause interference of incident infrared light at different wavelengths. Figure 4.4 depicts how a difference in particle size will affect relative peak height and locations of features in the molecular fingerprint regime. While the peak spacing is similar, the location of reflectance peaks will shift. Spectra above 1600 $cm^{-1}$ vary greatly with particle size. The changes in reflectance peak locations caused by Mie scattering make the spectra measured via diffuse reflectance different than those that can be measured via bulk reflectance of solid or powder bed measurements. Figure 4.4 emphasizes the spectral changes below 2000 $cm^{-1}$ because most chemicals do not have absorption and reflectance features outside this range.

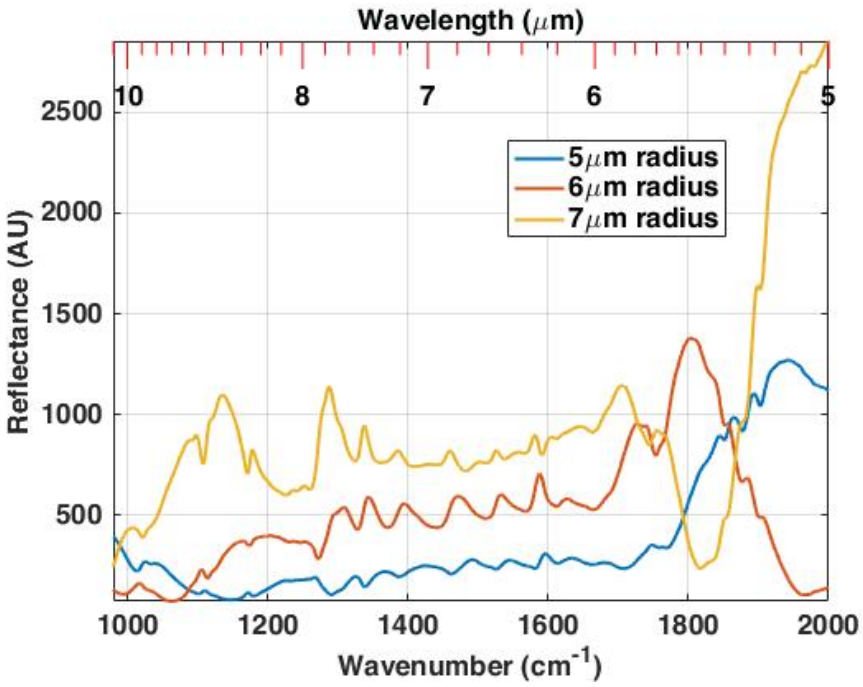


Figure 4.4: Acetaminophen spectra for particles on aluminum with a 5, 6, and 7 µm radius at 1° incident angle and -4.373° collection angle.

The substrate refractive indices also play a pronounced role in measurable diffuse reflectance. BV simulations of RDX and caffeine for various particle sizes on glass is shown in Fig. 4.5. Glass has a very distinct bulk reflectance that alters the prevalence of features beyond 1250 $cm^{-1}$ and features that may be obvious on aluminum are hidden by the decrease in reflectance of glass. This matches what is shown experimentally later when these particle size solutions are weighed in Fig. 4.10 to fit experimental measurements. Oscillatory features seen in the MWIR are caused by single particle size interference effects. With sufficiently large particle size distribution these effects disappear.

Adjusting the incident or collection angles in the MIST BV simulator affects the slope of the oscillations from 2500 - 4000 $cm^{-1}$ while minimally affecting the 900 - 1700 $cm^{-1}$ component in the molecular fingerprint regime as shown in Fig. 4.6. At small particle sizes, changes in incident or collection angles cause a slope change in reflectance values, but at longer wavelengths that baseline effect turn into bowing.

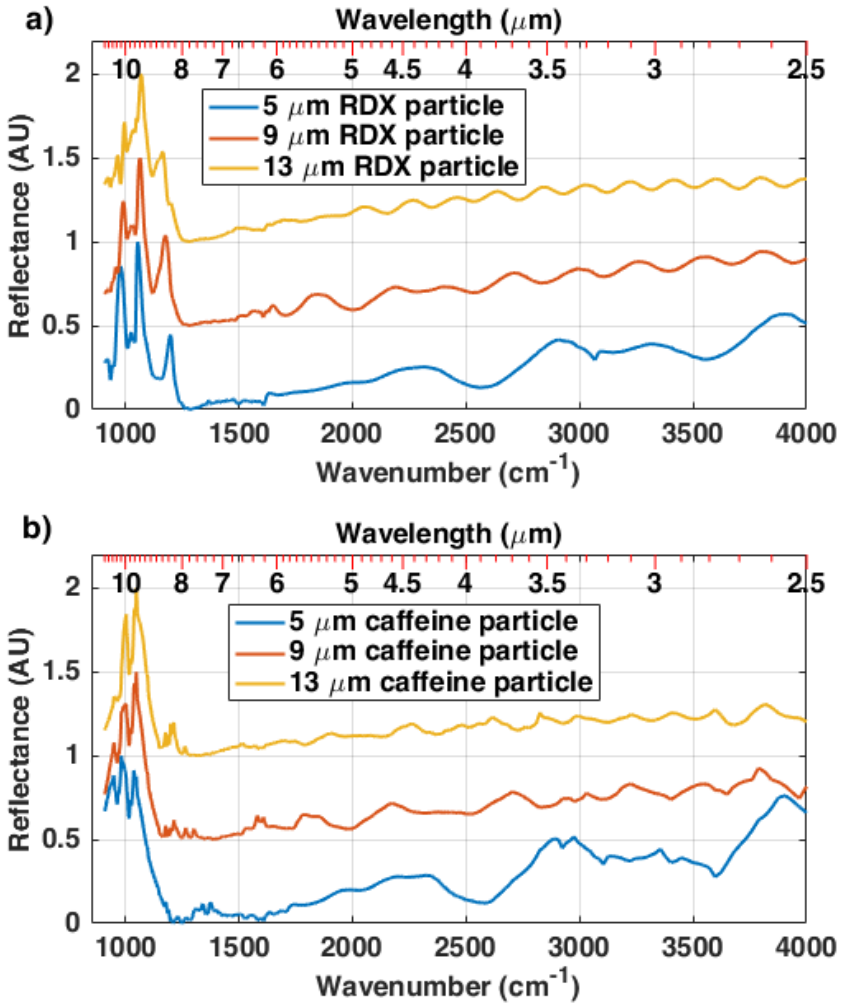


Figure 4.5: BV model predicted backscatter from a) RDX and b) caffeine for particles of radii, r = 5, 9, 13 µm deposited on a glass substrate from unpolarized light incident at 3° off normal. Spectra have been offset for clarity.

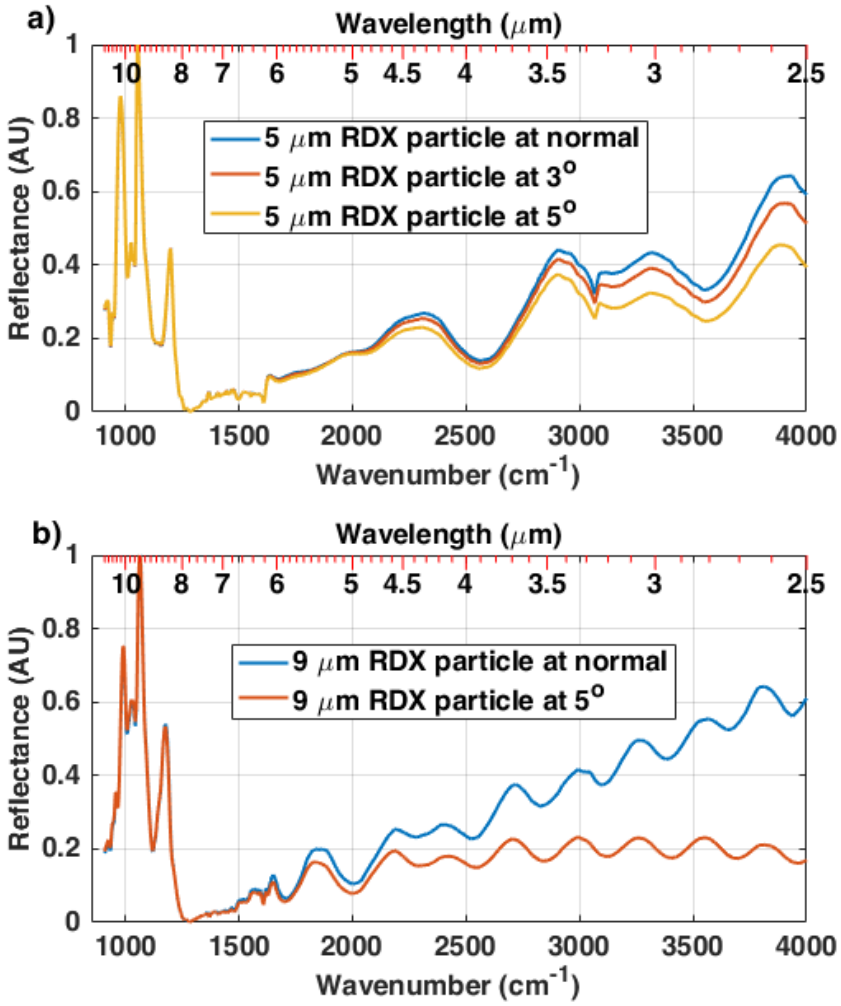


Figure 4.6: BV calculated incident beam angular dependence of scattered return for a) 5 µm and b) 9 µm RDX particles on glass. Slope and bowing of features above 2000 cm$^{-1}$ changes with particle size.

BV theory is required over a Mie and Transreflection based model because BV theory takes chemical and substrate optical properties into account when determining reflectance value. The Mie/Transreflection model predicts the backscattered and forward scattered energy from Mie theory then calculates how the forward scattered energy would be reflected from the substrate. This does not accurately predict how illumination and collection angles will impact scattering and cannot account for the second pass through the particle that the reflected light will take. BV theory however, takes these effects into account and models the boundary conditions between the chemical and the substrate.

## 4.5 Fitting BV Model Solutions to Standoff Trace Particle Measurements

We use the BV modeling of spherical particles from the previous section to fit spectra from trace particles of RDX, caffeine, and acetaminophen on aluminum, silicon, and glass substrates measured using the LWIR SC and FTIR based sensor. The experimental configuration for the measurement of trace particle targets is the same as that described in Fig. 3.5. The collection optics are measured to be 3.767° away from the incident plane. Data in this manuscript are shown for incident angles of 0° and 1°, which correspond to collection angles of -3.767° and -4.767°, respectively. The targets are placed on pitch and yaw stages to adjust and measure collection and incident angles for reproducible measurements. The preamplifier gain of the Vigo PCI detector is adjusted such that high load samples on glass produce a centerburst that fills the 1-volt range on the analog-to-digital converter. Specular measurements require a 30 dB optical attenuation filter to keep the interferogram centerburst within the linear range of the detector, scattering measurements of chemicals on aluminum or silicon require a 10 dB attenuation filter, and scattering measurements of chemicals

on glass are performed without attenuation. The experimental spectra shown in this chapter are produced by averaging together 8 runs of 500 scans and are divided by a background specular measurements from a $BaF_2$ wedge.

### 4.5.1 Log-Normal Particle Size Distributions

The scattering from real world samples are fit using the incoherent addition of the BV solutions for single particle sizes weighed with a log-normal distribution:

$$f(D) = \frac{1}{D\sigma\sqrt{2\pi}}\exp\left(-\frac{(\ln(D)-\mu)^2}{2\sigma^2}\right) \tag{4.1}$$

where $D$ is particle size, $\mu$ is the mean of the log of the distribution, and $\sigma$ is the standard deviation of the log of the distribution.

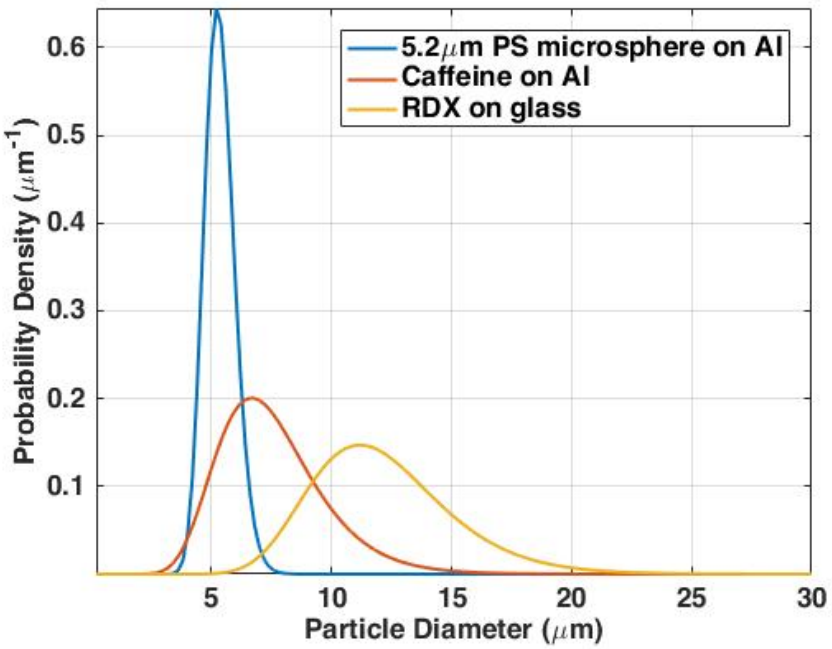


Figure 4.7: Exemplary log-normal particle size distributions for fits performed with BV model.

To illustrate how such distributions may look, Fig. 4.7 shows the probability density functions of the log-normal distributions for different measurements performed

in this chapter. Figure 4.7 depicts the distributions for the 5.2 µm PS microspheres on aluminum in Fig. 4.8(a), the caffeine on aluminum in Fig. 4.9(b), and the RDX on glass in Fig. 4.10(c).

### 4.5.2 Testbed Sensor Scattering Measurements of Spherical Particle Targets

We test the validity of BV theory for producing spectra that can match experimental results, by measuring mono-dispersed PS microspheres with 5.2, 10.8, and 19.5 µm diameters that are deposited on aluminum substrates. Figure 4.8 depicts the results of these measurements with an expanded wavenumber scale out that extends from 980 $cm^{-1}$ to 4000 $cm^{-1}$ to emphasize that BV theory accurately predicts oscillations caused by narrow particle size distributions of spherical particles. The simulated data in Fig. 4.8 is produced from log-normal particle size distributions with parameters $\mu = 1.67$, $\sigma = 0.117$ for the 5.2 µm spheres on aluminum, $\mu = 2.23$, $\sigma = 0.0471$ for 10.8 µm spheres on aluminum, and $\mu = 2.73$, $\sigma = 0.0566$ for 19.2 µm spheres on aluminum, with the incident and collection angles set to 0° and -3.767°, respectively. Single particle size solutions also provide accurate oscillation positions, but accentuate features not seen in measured data. The dip in spectra between 1720 and 1830 $cm^{-1}$ seen in all three measured spectra may be caused by carboxyl groups that can occur when PS degrades in UV light [25]. The features between 1000 and 1400 $cm^{-1}$ may be caused by water impurities gained during the emulsification process used to create the mono-disperse spheres. These features are not shown in the simulated data because the KBr pellets created with nonspherical PS powder, that were used to determine the complex refractive indices, did not contain these impurities.

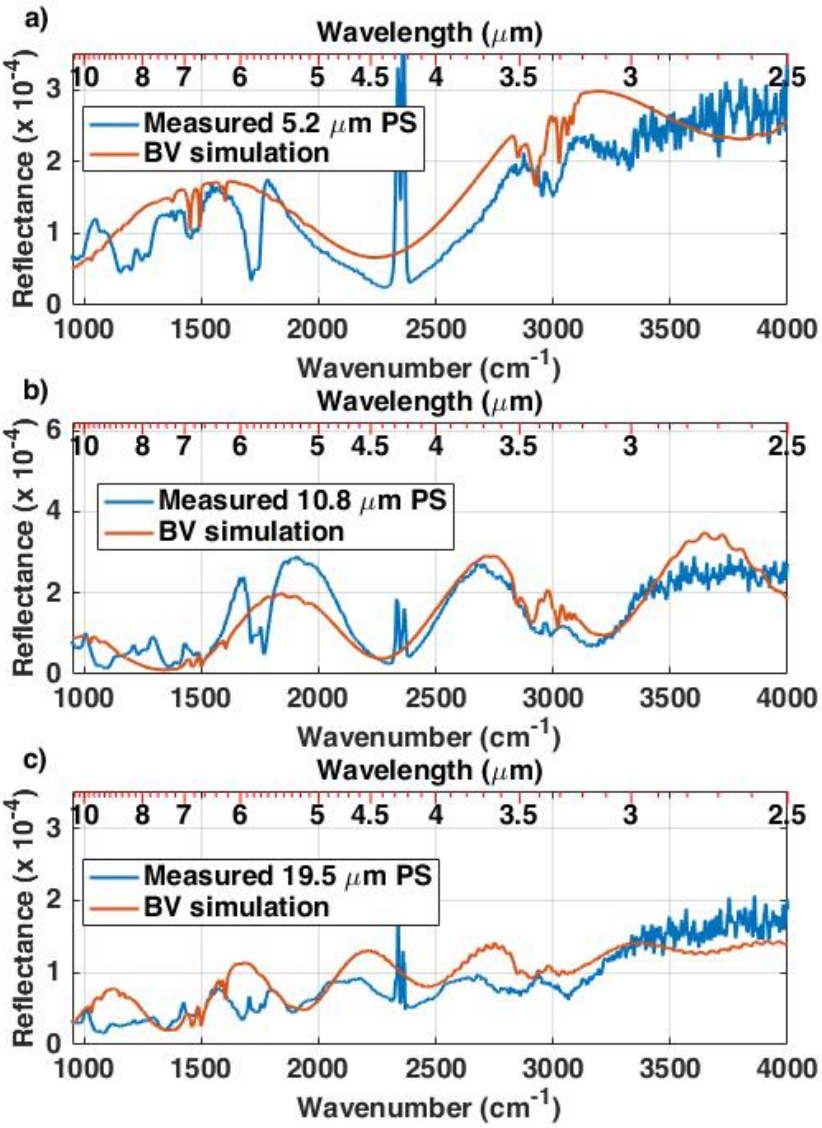


Figure 4.8: Return from (a) 5.2 µm, (b) 10.8 µm, and (c) 19.5 µm polystyrene microspheres deposited on aluminum substrates with BV simulated spectra.

### 4.5.3 Testbed Sensor Scattering Measurements Non-Spherical Particle Targets

Spectral signatures are dependent upon the chemical that is deposited on a given surface. Figure 4.9 shows measured scattered return from different chemicals deposited on 1" aluminum substrates with the log-normal fits of BV solutions for the given chemical on aluminum. The parameters for the fits are $\mu = 2.55$, $\sigma = 0.136$ for RDX on aluminum, $\mu = 1.98$, $\sigma = 0.286$ for caffeine on aluminum, and $\mu = 2.38$, $\sigma = 0.165$ for acetaminophen on aluminum, with the incident and collection angles set to 0° and -3.767°, respectively. Unique features for RDX, caffeine, and acetaminophen can be found in the molecular fingerprint regime between 950 and 1800 $cm^{-1}$. These spectra also contain a sharp reflectance change between 1600 and 1800 $cm^{-1}$, which corresponds to the last absorption peak that each chemical exhibits in this range (see Fig. 4.3).

Measurement discrepancies near 1700 $cm^{-1}$ can be caused by particle shape effects. Fig. 4.14, illustrates that non-spherical particles can have wildly varying spectra entering the MWIR because of shape induced resonances [15].

For a given chemical, the substrate can have a pronounced impact on reflectance spectra. Figure 4.10 shows measured scattered return from RDX deposited onto 1-inch aluminum, silicon, and glass substrates fitted with the BV simulations for the given substrate. The parameters for the fits are $\mu = 2.02$, $\sigma = 0.298$ for RDX on aluminum, $\mu = 2.13$, $\sigma = 0.255$ for RDX on silicon, and $\mu = 2.47$, $\sigma = 0.236$ for RDX on glass, with the incident and collection angles set to 1° and -4.767°, respectively. Although all three substrates are smooth and would not contribute scattered return themselves, their reflectance begin to play a role in the magnitude and clarity of signal. Specifically, glass reflectance decreases at ˜1250 $cm^{-1}$, and masks the features seen in the other two substrates between 1250 and 1800 $cm^{-1}$.

The magnitude of the scattered return from chemicals on a smooth surface is

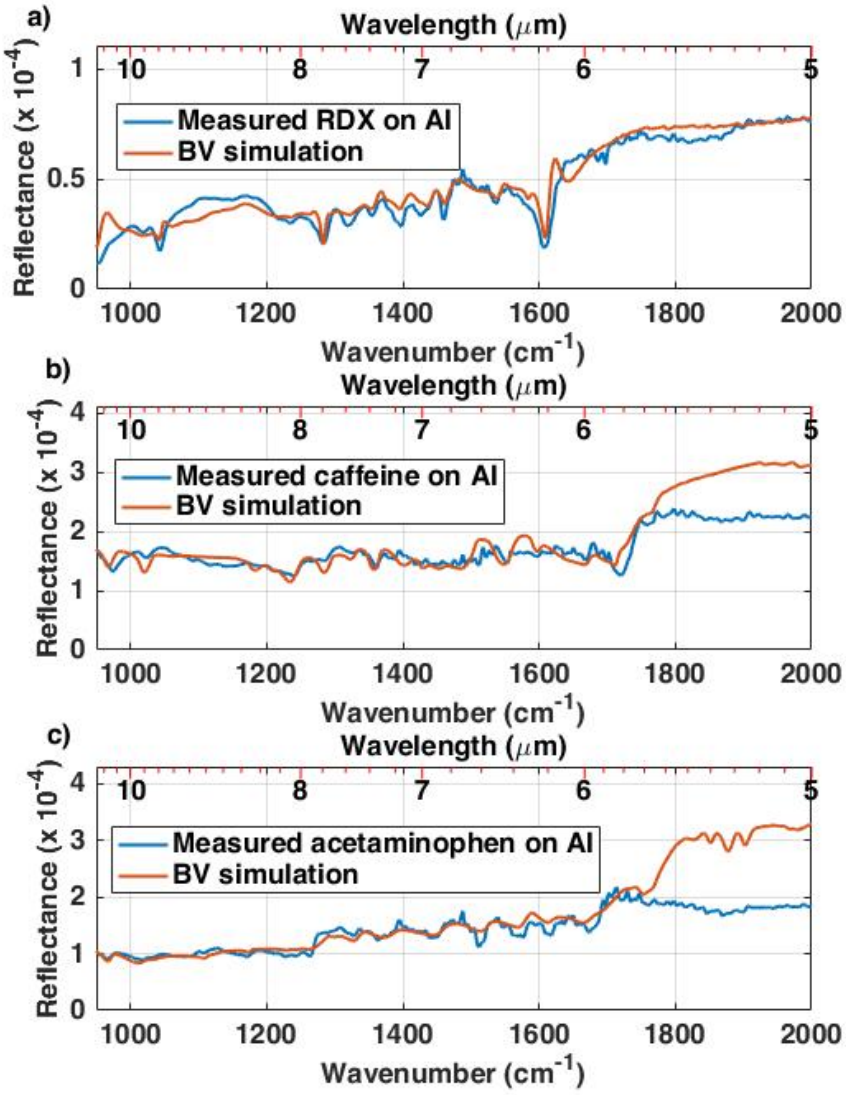


Figure 4.9: Experimental scattered return from (a) RDX, (b) caffeine, and (c) acetaminophen deposited on a 1"x1" aluminum substrate and their simulated return at 0° angle of incidence.

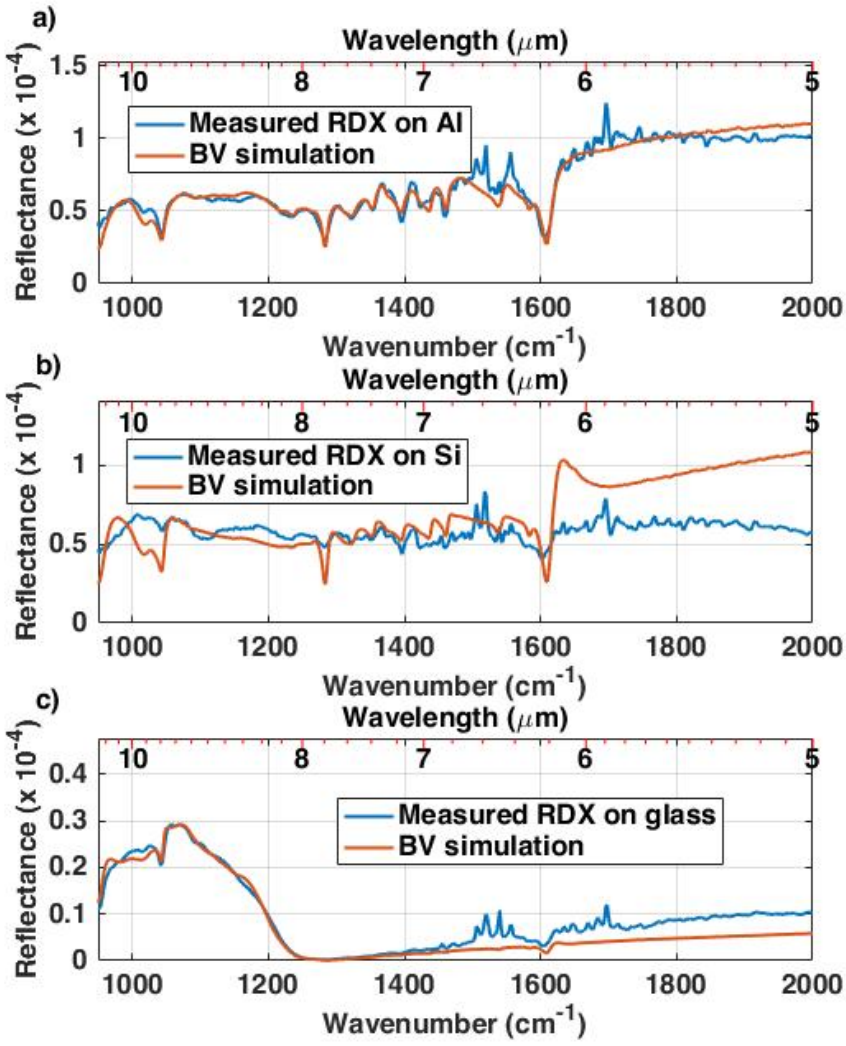


Figure 4.10: Experimental scattered return from RDX deposited on 1" x 1" (a) aluminum, (b), silicon, and (c) glass substrates and their simulated return at 1° angle of incidence.

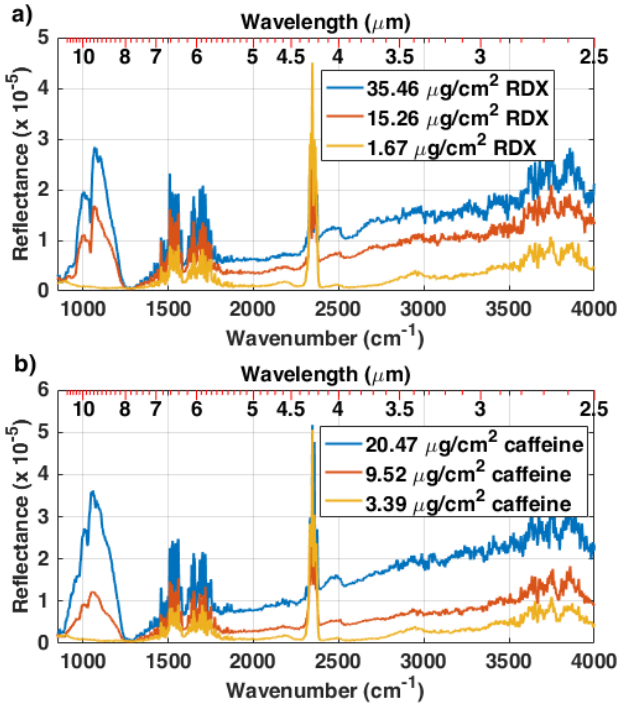


Figure 4.11: Testbed sensor measured scattering spectra of a) RDX and b) caffeine particles on glass at 3.6 m.

directly proportional to its concentration. The results of scattering measurements performed with the testbed sensor on sieve deposited RDX and caffeine particles on 1" x 1" glass substrate at varying concentrations are shown in Fig. 4.11. As particle concentration decreases, the chemical signatures visible at 900 - 1250 $cm^{-1}$ also decrease, but the atmospheric effects between 1250 - 1750 $cm^{-1}$, near 2350 $cm^{-1}$, and above 3500 $cm^{-1}$ do not.

### 4.5.4 Analysis of Measured Spectra

To aid in the analysis of the testbed sensor scattering measurements, the theoretical bulk reflectances of soda-lime glass, RDX, and caffeine are shown in Fig. 4.12. These figures show the normal incident Fresnel reflection expected from flat samples of each material calculated from their refractive index n- and k-values.

The BV model and microscope FTIR show that the substrate plays a large role in

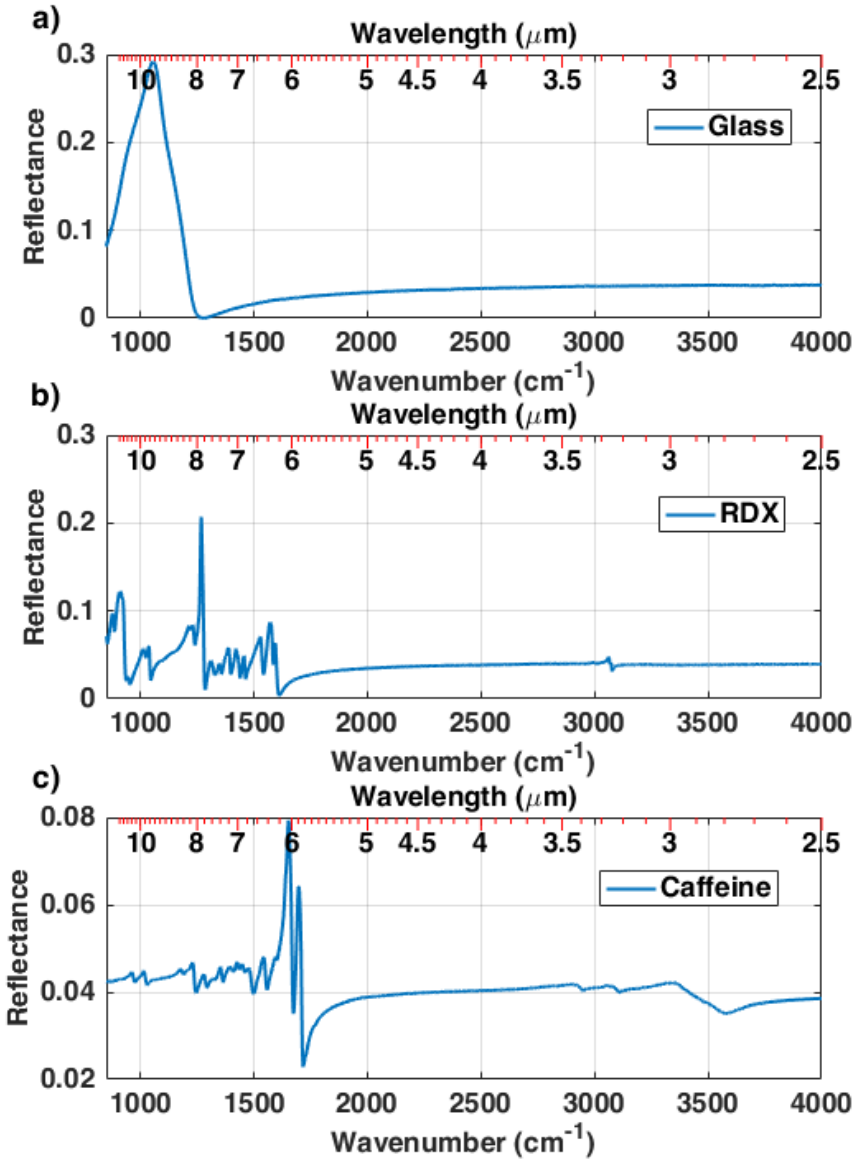


Figure 4.12: Theoretical bulk Fresnel reflection of a) soda-lime glass, b) RDX, and c) caffeine.

the shape of expected return spectra. The microscopic reflective FTIR measurements in Fig. 4.1 and BV particle simulations in Fig. 4.4 exhibit substrate reflectance features seen in the glass from Fig. 4.12. Chemical signatures based on particle size are superimposed upon the substrate signature as dictated by BV theory. This suggests that a high reflectance, smooth substrate will increase scattered return and allow for lower measured concentrations and further standoff distances. Unfortunately, if the substrate is not smooth, the substrate scattered return may overpower signals from chemicals found on its surface.

Chemical specific reflectance peaks exhibit wavelength dependent differences as expected from Mie scattering. Fortunately, the magnitude of the reflectance peaks and the location of the reflectance peaks quantifiably vary with respect to particle size and can be simulated with the BV model.

Because real world samples are comprised of many different particle sizes, the testbed sensor measured reflectance shown in Fig. 4.9 and Fig. 4.10 is a superposition of single particle size spectra. The experimental return is modeled by performing a log-normal weighted average of BV predicted returns. The model can estimate the concentration of the measured sample to within a factor of two from the magnitudes of the return signal. However, the particle distribution that best fits the experimental result for a given sample is not unique, and different particle distributions can yield similar return spectra. Examination of the images taken with the confocal microscope guide the selection of the most probably particle size distribution. Therefore, log-normal weighted BV modeling can be used to develop a library for chemical identification and differentiation but may not correctly estimate the particle size distribution.

The particle size distribution has a broadening and smoothing effect on the return spectra because reflectance peaks and troughs shift and change magnitude based on particle size. This may limit the differentiation between chemicals that are function-

ally and optically similar. Resolutions above 4 $cm^{-1}$ may not improve differentiation because the chemical features will be broader in samples made up of multiple particle sizes.

We measure variations in spectra caused by the background substrate on which chemicals are deposited. Silicon and aluminum have a flat specular return spectrum in the molecular fingerprint regime, but the magnitude of the silicon return should be ˜30% lower than that of the aluminum sample. We find that the magnitude of return are similar in Fig. 4.10, but the depth of the chemical features are less pronounced than those on the aluminum sample. This effect may be due to the second surface of the silicon wafer being unpolished. The unpolished side can diffusely scatter light back to the detector and provide a heightened baseline, which dilutes the chemical reflectance peaks. The signal height may also be caused by more particles sticking to the silicon substrate than the aluminum substrate after shipping. A smoothed second derivative for chemical identification can avoid these limitations.

The measurements performed in this study are for particles deposited on smooth substrates. Understanding the effects of roughened, non-uniform, or woven substrates on scattered return is important for the development of a sensor that will work in real world environments and will be one of the next steps in expanding the potential for LWIR standoff spectroscopy. Standoff illumination of particles on non-uniform substrates will cause infrared light to pass through particles multiple times and deepen the reflectance features in the molecular fingerprint regime [16] and return reflectance features from the bare substrate between particles. Aside from modeling constraints, experimentally, the scatter from a roughened substrate can be orders of magnitude higher than the scatter from particles on its surface. It is possible that glare reduction methods, such as illuminating with circularly polarized light and detecting non-circularly polarized light may reduce the amount of detected scatter from a rough substrate.

### 4.5.5 Distance and Concentration Limits of Standoff Sensor

We repeatably measure particle data on glass backgrounds and can determine some limits of the current testbed sensor configuration. Return spectra from particle samples at concentrations down to 7.4 µg/cm$^2$ are measured at 3.6 m. At this distance, the scattered return is 4 orders of magnitude lower than the incident intensity. According to BV modeling, the magnitude of the spectral return is directly proportional to the concentration of the particle on the substrate. As a first approximation of the limit of detection, based on regression analysis of the return for nine samples on glass shown in Fig. 4.13(a), we estimate the three standard deviation detection limit to be 6.5 µg/cm$^2$. This limit is limited by the instrument sensitivity and not the modeling. BV theory would be expected to fail at higher conecentrations when there is much more particle aggregation and contact.

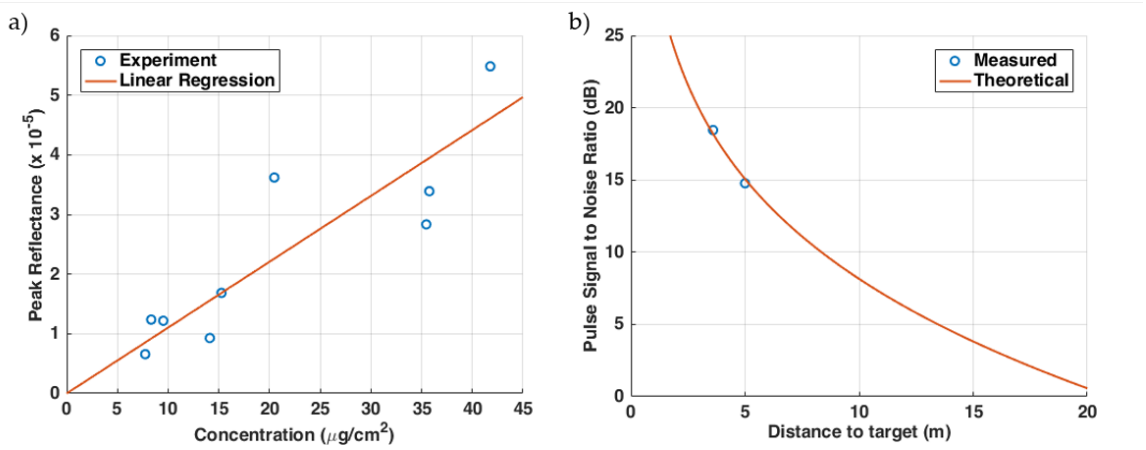


Figure 4.13: (a) Linear regression to determine the lowest measurable concentration with the LWIR SC FTIR sensor. (b) Theoretical centerburst pulse SNR assuming incident intensity described in Fig. 2.7 and 1/r$^2$ dependence on scattered intensity.

The theoretical maximum distance that this sensor can measure a given sample would be based on the height of the collected centerburst pulse, which must be at least 3 dB above the noise to produce measurable spectra. The centerburst return

signal is expected to be inversely proportional to the square of the distance between the target and the first collecting optic. By assuming a $M^2 = 2$ quality beam as described in Fig. 2.7, the theoretical maximum distance that this sensor can measure a 40 µg/cm$^2$ sample is ˜16 m. Preliminary measurements at a 5 m distance agree with this analysis as shown in Fig. 4.13(b). Ways to increase the measurement distance will be discussed in Section 5.3.3.

### 4.5.6 Deviations in the MWIR

BV simulation and measured spectra can deviate in the MWIR because this regime is susceptible to geometry related resonances [16]. As the wavelength decreases with respect to the particle size, particle shape begins to play a more pronounced role, as more spherical harmonics are required to approximate the interaction of the incoming wave with the particle.

Deviations from theoretical predictions between 2500 and 4000 cm$^{-1}$ that may arise from variations in collection and incident angle compared to those modeled and particle shape differences. Adjusting the incident or collection angles in the MIST BV simulator affects the slope of the oscillations from 2500 - 4000 cm$^{-1}$ while minimally affecting the 900 - 1250 cm$^{-1}$ component as shown in Fig. 4.6. Additionally, the spectral features above 1667 cm$^{-1}$ are be governed by interference effects caused by particle geometry, and that these effects can differ according to particle roughness [15]. These traits also explain why there will be differences in microscope or close-range diffuse scattering measurements, which both collect with a high NA, compared to those measured at a standoff distance and low NA. The geometric contributions will begin to average together at larger illumination and collection angles.

### 4.5.7 Particle Shape and $n_\infty$ Effect

Figure 4.2 shows that trace particles on surfaces are not spherical. It is much more computationally intensive to simulate the diffuse reflectance from non-spherical particles, and there is a myriad of parameters that can be changed to alter spectra. We justify the spherical particle approximation used in this chapter, by showing that the reflectance spectra of various axisymmetric particles can be approximated by a spherical particle of the same volume.

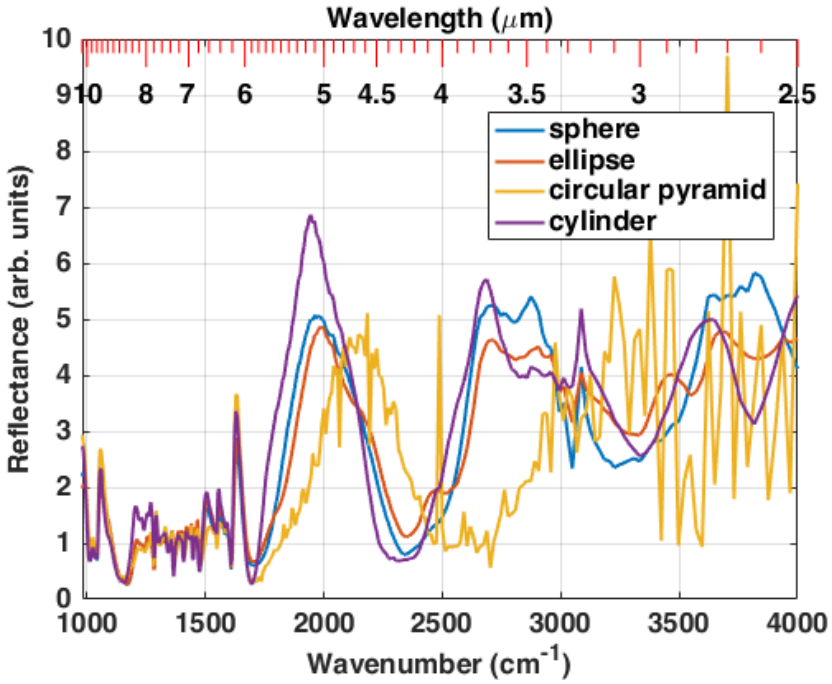


Figure 4.14: RDX spectra for particles on aluminum of differing axisymmetric shapes with the same volume.

Figure 4.14 shows the molecular fingerprint for a spherical particle of radius 5 µm, an ellipsoidal particle with a vertical semiaxis of 4.7 µm and horizontal semiaxes of 5.15 µm, a circular pyramidal particle of radius 5 µm and height 20 µm, and a cylindrical particle of radius 5.5 µm and height 8.2 µm. Chemical reflectance peak locations in the molecular fingerprint regime for non-spherical particles can match those of spherical particles with the same volume. However, as the light approaches

shorter wavelengths, the theoretical spectra begin to vary drastically.

Volume is not the only metric to consider when varying particle shape. Narrower and taller particles of the same volume may exhibit drastic peak position shifts in the LWIR and exhibit features more similar to larger radius spheres. For example, a circular bipyrimidal particle of radius 5 µm and height 10 µm is better simulated with a spherical particle of radius 8 µm in the molecular fingerprint regime.

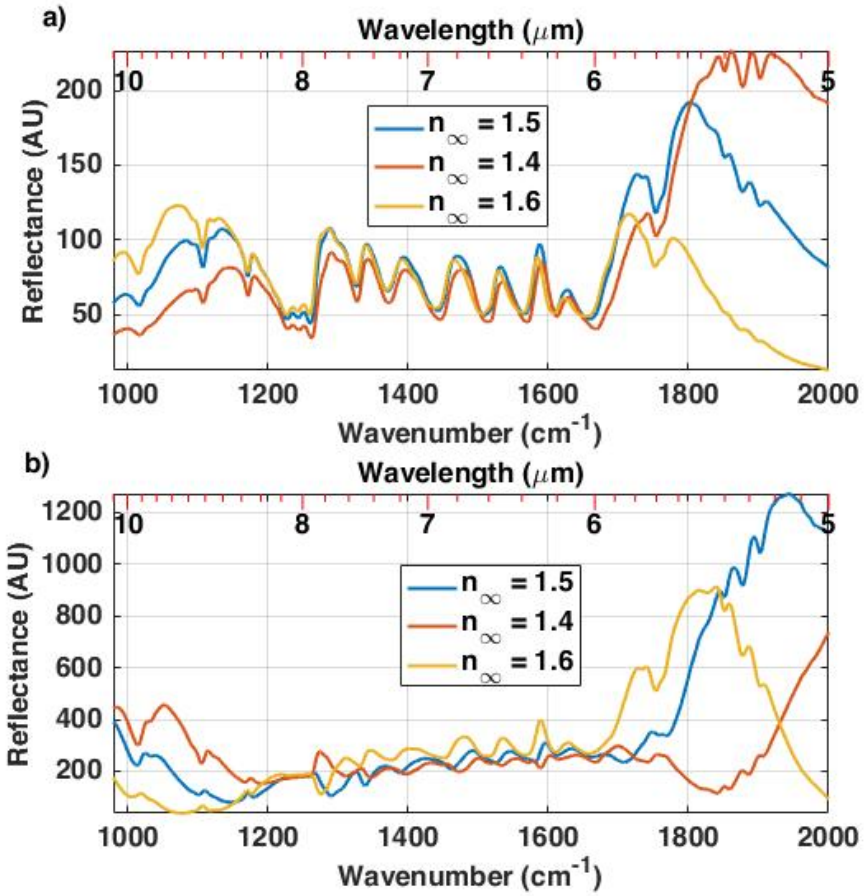


Figure 4.15: Acetaminophen spectra for particles on aluminum with a (a) 3 µm radius and (b) 5 µm radius when $n_\infty$ is shifted from its original value of 1.5.

For completeness, we have also modeled the impact a change in $n_\infty$ may have on diffusely scattered return. Figure 4.15 illustrates spectral changes caused altering the $n_\infty$ value for 3µm and 5µm radius particles. Adjusting $n_\infty$ from 1.5 to 1.4 or 1.6 greatly affects spectra entering the MWIR and has a more pronounced effect in the

LWIR for larger particle sizes by shifting reflectance peak locations. The shift in peak position for adjusting the $n_\infty$ value is similar to the change seen when particle size is changed as shown in Fig. 4.4 Therefore, peak position errors that may arise from overall shifts of $n_\infty$ can be minimized by the use of a log-normal weighted distribution of particle sizes for real world trace particle identification.

Overall, particles on surfaces will produce diffuse reflectance spectra that will express changes in peak reflectance positions based on particle size as seen in Fig. 4.4. Fig. 4.5 shows that reflectance spectra are further complicated by the substrate reflectance, which weighs the return spectra with its reflectance properties and must be calculated using BV theory. Errors in refractive-indices calculations as depicted in Fig. 4.15 are on the same order as particle size changes and can be mitigated with particle size distributions as described in Section 4.5. Spectral differences caused by non-spherical particles are minimal in the LWIR for particles of similar volumes but are much more pronounced in the MWIR, especially as shapes vary further from spherical (See Fig. 4.14). Geometry related resonances begin to dominate in the MWIR [15] and can overwhelm the weaker absorbances that some chemicals exhibit in the MWIR. Because most MWIR chemical features are hidden, we typically limit the unknown chemical identification wavenumber range to 950 $cm^{-1}$ - 1800 $cm^{-1}$. However, the MWIR can provide information about the target orientation with respect to the illumination and collection optics. Figure 4.6 suggests that target tilt can be determined by examining the baseline curvature of measured spectra.

## 4.6 Unknown Chemical Identification

The goal of the work done in this dissertation is to create a non-contact, non-ionizing, optical measurement device that can be used to identify unknown chemicals at a distance without having to approach at distances that would put the investigator in danger of said chemicals. Using the insights gained from Section 4.5.2 and Section

4.4.1, the log-normal distributions of BV solutions can be utilized for unknown trace chemical identification.

To test this, we create a library of scattering spectra for RDX, caffeine, and acetaminophen at normal incidence and a -3.767° collection angle assuming log-normal particle size distributions of spherical particles varying in maximum probability particle diameter, $D_{max}$ = 0.1 to 25.8 µm in 0.2 µm steps and $\sigma$ = 0.01 to 0.5 in 0.01 steps. The unknown targets contain sieve deposited RDX, acetaminophen, or caffeine particles on a 1" x 1" aluminum substrate that have been randomized and presented to the tester. The tester measures the backscattered spectra of the unknown at normal incidence and compare the measured spectra to the library of spectra created for RDX, caffeine, and acetaminophen. The figure of merit (FOM) for chemical identification is the root mean square error between the second derivative of the measured and simulated spectra and is described below:

$$FOM = \sqrt{\frac{1}{n}\sum_{\nu}\left(\frac{R''(\nu)}{max|R''(\nu)|} - \frac{S''(\nu)}{max|S''(\nu)|}\right)^2} \tag{4.2}$$

where $R''(\nu)$ and $S''(\nu)$ are the smoothed second order derivatives of the measured spectra and simulated spectra for a given wavenumber, $\nu$, and n is the number of wavenumbers in the range of interest. Spectra are smoothed and a second order derivative is taken using the Savitzky-Golay method with a 19-point window and third-degree smoothing order. We choose to examine features in the molecular fingerprint regime from 980 to 1800 $cm^{-1}$. The library value with the minimum FOM are considered to be the best match for the unknown chemical.

Table 4.1 shows a comparison the library spectra of three unknown trace chemicals that have been deposited on 1" x 1" aluminum substrates, with the lowest FOM for each unknown highlighted in gray. The identification schema works well for unknowns with large absorption and refractive index features. This is exhibited by Unknown

Table 4.1: Lowest figure of merit values for measured unknowns compared to library spectra for RDX, caffeine, and acetaminophen. The comparison with the lowest figure of merit has been highlighted and depicts the identity of the unknown trace chemical on aluminum.

| Sample | RDX | caffeine | acetaminophen |
|---|---|---|---|
| Unknown 1 | 0.2423 | 0.2015 | 0.2603 |
| Unknown 2 | 0.0787 | 0.2395 | 0.2486 |
| Unknown 3 | 0.3137 | 0.2655 | 0.1801 |

2, which exhibits a low FOM for RDX. Similarly, some chemicals have a much less varied refractive index profile. The difference in FOM values for unknown 1 are not as pronounced because the complex refractive index for caffeine does not contain the larger variations shown in the complex refractive index of RDX.

An example of the spectra for Unknown 3 is presented in Fig. 4.16 and illustrates the best fit cases of an unknown chemical with simulated spectra of RDX, caffeine, and acetaminophen on aluminum. The second derivative of the measured data shows peaks in the molecular fingerprint regime that match with those modeled for the given chemical. Because there are minimal features outside of the molecular fingerprint regime, the second derivative is relatively constant above 1800 $cm^{-1}$. Second derivative data is noisy above 3000 $cm^{-1}$ due to water absorption and lower wavenumber spectral density and is not considered in the FOM. The figure of merit for the shown spectra are 0.3137, 0.2655, and 0.1801 for RDX, caffeine, and acetaminophen, respectively. Using this metric, we would identify Unknown 3 as acetaminophen.

### 4.6.1 Second Derivative and FOM Analysis

We use the second derivative of measured spectra for library comparisons because bowing or baseline deviations can cause false positives in chemical identification. The total magnitude of scattered return will vary with respect to chemical density and substrate background as well as the target distance from the collection optics [8]. Analyzing second derivatives is a standard method in spectroscopy to emphasize

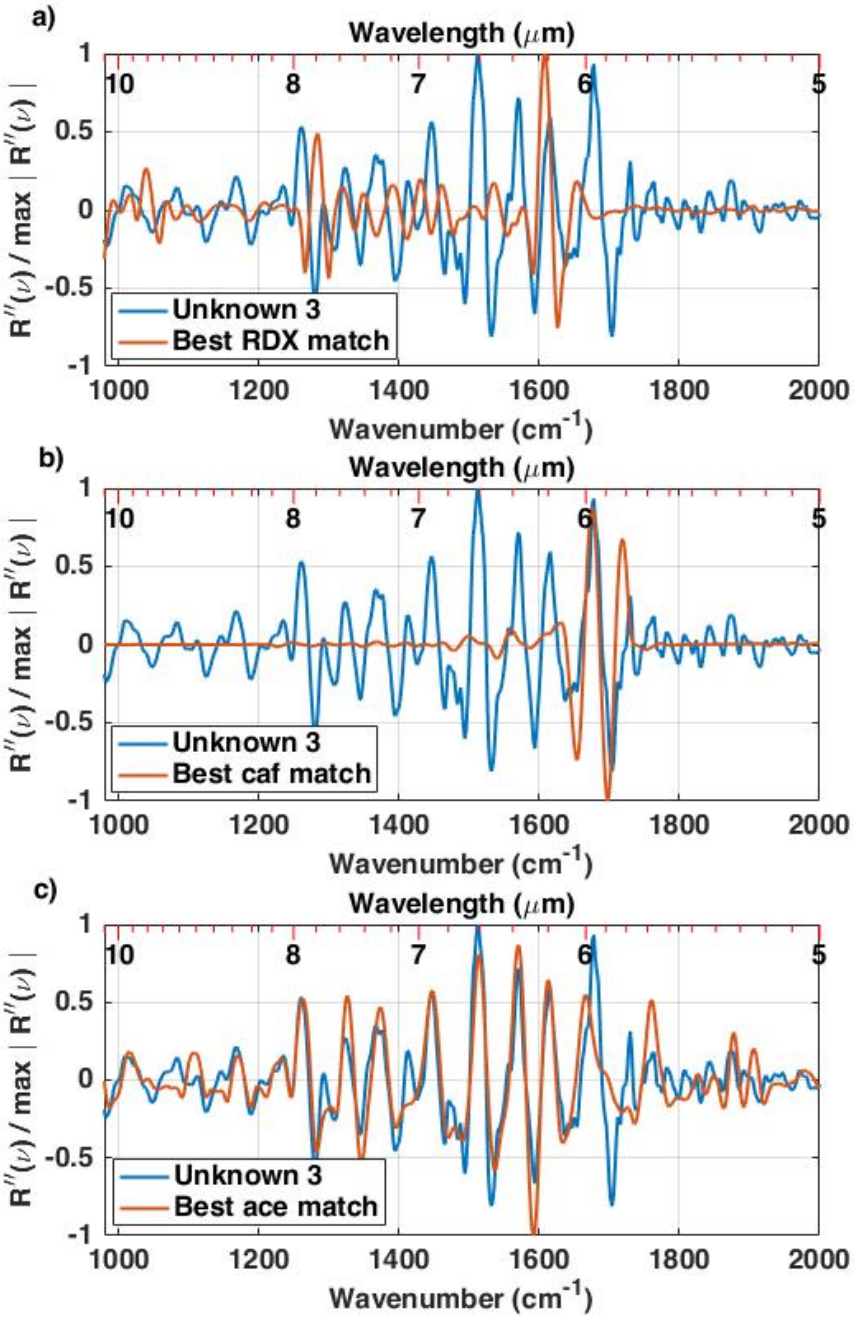


Figure 4.16: The second derivative of Unknown 3 compared to the lowest FOM match from libraries created using log-normal distributions of (a) RDX, (b) caffeine, and (c) acetaminophen.

sharp structures [26]. By comparing second derivatives, we focus our identification techniques on chemical feature recognition rather than slowly varying baseline or magnitude changes that may result from misalignment, particle shape, or chemical concentration.

There are several limitations to the use of the root mean square error as the figure of merit for chemical identification. Firstly, the second order derivative of measured and simulated spectra oscillate around zero and reduces the maximum value obtainable for a FOM. For instance, the worst library match to a sample measurement during unknown testing, does not exceed a FOM of 0.5271. Additionally, slight shifts in peak location can cause large variations in the difference between spectra at a given wavenumber. This disadvantage is minimized because the log-normal distribution of particles widens sharp spectral features found in single particle size reflectance.

## 4.7 Summary

We analyze the spectra obtained from sparsely loaded powders deposited on smooth substrates. We find that the long-wave infrared from 950 to 1800 $cm^{-1}$ contains robust chemical information that is dependent upon particle size distribution, chemical refractive indices, and the substrate material. We model these effects using BV theory, and can use this model as an analytical tool to predict the backscattered spectra of unmeasured samples illuminated by LWIR light at standoff distances. The LWIR backscattered spectra of non-spherical particle can be well approximated by spherical particles of a similar volume. Second derivative analysis removes baseline magnitude changes caused by chemical concentration and slowly varying changes that may arise from target orientation and focuses chemical identification on the sharp chemical features in the LWIR. The insights gained by examining and modeling single particles deposited on smooth substrates can enable the study of more complex targets in the future and further the capabilities of real LWIR spectroscopic

techniques.

## References


[1] David A Kirchgessner, Stephen D Piccot, and Ajay Chadha. Estimation of methane emissions from a surface coal mine using open-path ftir spectroscopy and modeling techniques. *Chemosphere*, 26(1-4):23–44, 1993.

[2] Roland Harig. Passive remote sensing of pollutant clouds by fourier-transform infrared spectrometry: signal-to-noise ratio as a function of spectral resolution. *Applied Optics*, 43(23):4603–4610, 2004.

[3] Mark L Polak, Jeffrey L Hall, and Kenneth C Herr. Passive fourier-transform infrared spectroscopy of chemical plumes: an algorithm for quantitative interpretation and real-time background removal. *Applied optics*, 34(24):5406–5412, 1995.

[4] Ramon A Martinez, Genevieve Plant, Kaiwen Guo, Brian Janiszewski, Michael J Freeman, Robert L Maynard, Mohammed N Islam, Fred L Terry, Oseas Alvarez, Francois Chenard, Robert Bedford, Ricky Gibson, and Agustin I Ifarraguerri. Mid-infrared supercontinuum generation from 1.6 to >11 $\mu$m using concatenated step-index fluoride and chalcogenide fibers. *Optics letters*, 43(2):296–299, 2018.

[5] Kaiwen Guo, Ramon A Martinez, Genevieve Plant, Lukasz Maksymiuk, Brian Janiszewski, Michael J Freeman, Robert L Maynard, Mohammed N Islam, Fred L Terry, Robert Bedford, Ricky Gibson, Francois Chenard, Stephane Chatigny, and Agustin I Ifarraguerri. Generation of near-diffraction-limited, high-power supercontinuum from 1.57 $\mu$m to 12 $\mu$m with cascaded fluoride and chalcogenide fibers. *Applied optics*, 57(10):2519–2532, 2018.

[6] Sergey Vasilyev, Igor S Moskalev, Viktor O Smolski, Jeremy M Peppers, Mike Mirov, Andrey V Muraviev, Kevin Zawilski, Peter G Schunemann, Sergey B Mirov, Konstantin L Vodopyanov, and Valentin P Gapontsev. Super-octave longwave mid-infrared coherent transients produced by optical rectification of few-cycle 2.5-$\mu$m pulses. *Optica*, 6(1):111–114, 2019.

[7] Christopher J Breshike, Christopher A Kendziora, Robert Furstenberg, Viet Nguyen, Andrew Kusterbeck, and R Andrew McGill. Infrared backscatter imaging spectroscopy of trace analytes at standoff. *Journal of Applied Physics*, 125(10):104901, 2019.

[8] Ramon Arturo Martinez, Kaiwen Guo, Tianqu Zhai, Fred L Terry, Leland E Pierce, Mohammed Nazrul Islam, Ricky Gibson, Jennifer Reed, Robert Bedford, Lukasz Maksymiuk, Michael J Freeman, Brian A Gorin, Noah P Christian, and Agustin I Ifarraguerri. Active mid-wave to long-wave supercontinuum ftir sensor for standoff chemical detection. *Journal of Lightwave Technology*, 2019.

[9] JS Li, B Yu, H Fischer, W Chen, and AP Yalin. Contributed review: Quantum cascade laser based photoacoustic detection of explosives. *Review of Scientific Instruments*, 86(3):031501, 2015.

[10] Charles W Van Neste, Larry R Senesac, and T Thundat. Standoff photoacoustic spectroscopy. *Applied Physics Letters*, 92(23):234102, 2008.

[11] Robert Furstenberg, CA Kendziora, J Stepnowski, SV Stepnowski, M Rake, MR Papantonakis, V Nguyen, GK Hubler, and RA McGill. Stand-off detection of trace explosives via resonant infrared photothermal imaging. *Applied Physics Letters*, 93(22):224103, 2008.

[12] Xing Chen, Dingkai Guo, Fow-Sen Choa, Chen-Chia Wang, Sudhir Trivedi, A Peter Snyder, Guoyun Ru, and Jenyu Fan. Standoff photoacoustic detection of explosives using quantum cascade laser and an ultrasensitive microphone. *Applied Optics*, 52(12):2626–2632, 2013.

[13] Viet Nguyen, Michael Papantonakis, Robert Furstenberg, Christopher Kendziora, and R Andrew McGill. Real-world particulate explosives test coupons for optical detection applications. In *Chemical, Biological, Radiological, Nuclear, and Explosives (CBRNE) Sensing XIV*, volume 8710, page 87100T. International Society for Optics and Photonics, 2013.

[14] Christopher J Breshike, Christopher A Kendziora, Robert Furstenberg, Yohan Yoon, TJ Huffman, Viet Nguyen, and R Andrew McGill. Rapid detection of infrared backscatter for standoff detection of trace explosives. In *Chemical, Biological, Radiological, Nuclear, and Explosives (CBRNE) Sensing XXI*, volume 11416, page 114160W. International Society for Optics and Photonics, 2020.

[15] Robert Furstenberg, Christopher A Kendziora, Michael R Papantonakis, Viet Nguyen, and R Andrew McGill. The challenge of changing signatures in infrared stand-off detection of trace explosives. In *Chemical, Biological, Radiological, Nuclear, and Explosives (CBRNE) Sensing XV*, volume 9073, page 90730M. International Society for Optics and Photonics, 2014.

[16] Robert Furstenberg, Andrew Shabaev, Christopher A Kendziora, Christopher Breshike, Tyler J Huffman, Andrew Kusterbeck, Dawn Dominguez, Samuel G Lambrakos, and R Andrew McGill. Synthetic models for infrared reflectance signatures of micro-particle traces on surfaces. In *Chemical, Biological, Radiological, Nuclear, and Explosives (CBRNE) Sensing XX*, volume 11010, page 110100K. International Society for Optics and Photonics, 2019.

[17] Christopher J Breshike, Christopher A Kendziora, Norman Budack, Yohan Yoon, Robert Furstenberg, Viet Nguyen, and R Andrew McGill. Active lwir hyperspectral imaging and algorithms for rapid standoff trace chemical identification. In *Algorithms, Technologies, and Applications for Multispectral and Hyperspectral Imagery XXV*, volume 10986, page 109860K. International Society for Optics and Photonics, 2019.

[18] Gorden Videen. Light scattering from a sphere on or near a surface. *JOSA A*, 8(3):483–489, 1991.

[19] PA Bobbert and J Vlieger. Light scattering by a sphere on a substrate. *Physica A: Statistical Mechanics and its Applications*, 137(1-2):209–242, 1986.

[20] Ramon A Martinez, Kaiwen Guo, Fred L Terry Jr, Tianqu Zhai, Mohammed N Islam, and Agustin I Ifarraguerri. Scattering spectra from trace particles actively illuminated by a mid-infrared supercontinuum ftir sensor. In *Optical Biopsy XVIII: Toward Real-Time Spectroscopic Imaging and Diagnosis*, volume 11234, page 112340V. International Society for Optics and Photonics, 2020.

[21] Gustav Mie. Beiträge zur optik trüber medien, speziell kolloidaler metallösungen. *Annalen der physik*, 330(3):377–445, 1908.

[22] Thomas A Germer. Modeled integrated scattering tool (mist). `https://pages.nist.gov/ScatterMIST/docs/index.htm`, 2017. 2018-05-30.

[23] Thomas A Germer. Scatmech: Polarized light scattering c++ class library. `https://pages.nist.gov/SCATMECH/docs/index.htm`, 2018. 2018-05-30.

[24] Tanya L Myers, Ryan M Francis, Catherine A Banach, Sarah D Burton, Ashley M Oeck, Timothy J Johnson, Robert Furstenberg, and Christopher A Kendziora. Obtaining the complex optical constants n and k via quantitative absorption measurements in kbr pellets. In *Chemical, Biological, Radiological, Nuclear, and Explosives (CBRNE) Sensing XX*, volume 11010, page 110100M. International Society for Optics and Photonics, 2019.

[25] José Salas Vicente, Juan López Gejo, Sonja Rothenbacher, Sumalekshmy Sarojiniamma, Eliso Gogritchiani, Michael Wörner, Gerhard Kasper, and André M Braun. Oxidation of polystyrene aerosols by vuv-photolysis and/or ozone. *Photochemical & Photobiological Sciences*, 8(7):944–952, 2009.

[26] Barbara Stuart. Infrared spectroscopy. *Kirk-Othmer Encyclopedia of Chemical Technology*, 2000.

# CHAPTER V

# Summary and Future Work

## 5.1 Summary

This dissertation is focused on the development of a LWIR SC source and sensor for standoff spectroscopic measurements, and the measurement and modeling of trace particles deposited on smooth surfaces. We do this by creating an SC source for standoff illumination, implementing a sensor capable of measuring diffuse scattering at a distance, and modeling chemical spectra to create a reference library for identification.

We've created an all-fiber supercontinuum source with at least an order of magnitude higher power output than other fiber-based SC sources in this wavelength range. The elegant and simple design makes it a robust source with high spectral density that can be customized to fit the needs of real-world applications. This dissertation describes an output from the LWIR SC source of up to 417 mW at 800 kHz that extends from 1.6 - 11 µm via the concatenation of ZBLAN, $As_2S_3$, and $As_2Se_3$ solid-core, supercontinuum generating fibers that are pumped with Er/Yb amplifier based MOPA configuration.

Several breakthroughs and achievements were required for the success of this source. First, the use of a thulium amplifier to filter light below 2 µm and amplify energy above 2 µm increases the spectral density of the signal and reduces high-loss

wavelengths from interacting with low damage threshold fibers. Second, the cascade of fibers from high damage threshold/low transmission window to low damage threshold/high transmission window protects each subsequent fiber while spreading the spectra to beyond high loss regions. Third, the development of a low loss, high 0.76 NA, $As_2Se_3$ fiber that has a loss edge of $> 11$ µm, prevents the spread of the mode field diameter of light within the fiber at high wavelengths. Lower NA fibers, though commercially available, have large mode field diameters that spread too far into the cladding, which reduces non-linearities and increases loss from cladding impurities. Finally, the development of the splice between the chalcogenide fibers reduced Fresnel losses from almost 50% to less than 1%, and helps protect the input face of the $As_2Se_3$ fiber.

Because of the concatenated design, if shorter wavelengths than those described and used in this dissertation are necessary, the change or removal of fibers in the chain can lead to the required spectra. For example, if wavelengths up to 6 - 7 µm are required for $NO_x$ detection and analysis, the $As_2Se_3$ fiber can be removed and the higher output from the $As_2S_3$ fiber would be sufficient.

The single mode, near diffraction-limited output enables collimation with limited divergence and enables the use of the LWIR SC source as an active illuminator for standoff spectroscopy. We are able to create a standoff infrared sensor using a refraction-based FTIR to modulate the output signal into an interferogram that can be Fourier transformed into an infrared spectra that spans from 950 $cm^{-1}$ to 4000 $cm^{-1}$ (2.5 µm - ˜10.5 µm) with 4 $cm^{-1}$ resolution. This sensor utilizes a Triggered simultaneous acquisition and record function that allows every one of the ˜6000 pulses in an interferogram to be captured and recorded, for an acquisition time of 69 seconds for 1000 scans.

In Chapter III we demonstrate volatile gas spectra along a 10 cm path length and measure the diffuse scattering from bulk samples with the LWIR SC and FTIR based

sensor. We find that these spectra may vary with respect to commercially available FTIR systems because of the differences in collection and illumination optics. Our standoff sensor is necessarily low NA illumination and collection, which causes features in the MWIR measured with the standoff sensor to differ from those measured in a commercial FTIR with high NA illumination and collection for diffuse scattering measurements. We also find that it is necessary to use a smooth target with a smooth featureless Fresnel reflection as a background scan because while scattering references are less angle dependent, they exhibit sharp features in the molecular fingerprint regime that muddy chemical response signatures.

The LWIR SC and FTIR based sensor is also be used to measure trace particles that have been deposited on smooth substrates. Despite most real-world particles being non-spherical, their reflectance spectra can be estimated by spherical particles because differences in particle geometry impact the MWIR more strongly than the LWIR. We find that the concentration of particles on the surface determine the overall magnitude of the return signal and there are unique reflectance peaks in the molecular fingerprint regime that can be used for chemical identification. We are able to measure powders at concentrations as low as 6.5 $\mu g/cm^2$ at a 3.6 m distance.

We model the effects of particles on smooth substrates using Bobbert-Vlieger modeling that uses particle size, incident angle, scattering angle, chemical refractive indices, substrate refractive indices, and collection NA to numerically determine the reflectance of a particle on a smooth surface. The BV model we use to fit experimental data weighs the single particle size solutions with a log-normal distribution and adds them incoherently. This creates particle distributions similar to those present in real-world situations, such as particle contamination on surfaces from being in a powder filled room, or the deposition of loose powders from a fingerprint.

The log-normal distribution of particle shapes changes the features that would be found in single particle size cases. Narrow particle distributions or single particle sizes

exhibit sharp chemical features and oscillatory behavior associated with interference effects. As the distribution of particle sizes widens, chemical features broaden and their peaks and dips diminish in strength because different particle sizes exhibit those peaks at shifted positions and varying relative strengths determined by Mie scattering. This has the additional consequence of causing multiple particle size distributions to exhibit the same reflectance spectra. The absence of unique solutions is beneficial to chemical identification because it would require less spectra to characterize a given chemical when creating a library of potential spectra for that chemical.

We find that one method for chemical identification of unknown chemicals on substrates is to use a figure of merit that determines the root mean square error between the normalized second derivative reflectance spectra of an unknown with a library of theoretical normalized second derivative reflectance spectra created from systematically created log-normal distributions of the single particle size BV solutions. The second derivative spectra reduce the prevalence of magnitude and baseline errors that may come from particle shape, target tilt, or concentration of particles.

We have developed a new light source and sensor to non-destructively measure spectra from trace particles at standoff distances. We then simulate the reflectances of particles on smooth substrates and use our simulations to create a library from which we can identify unknowns based on the reflectance peaks and troughs in the molecular fingerprint regime using second derivative spectra. Because measured spectra can vary with respect to particle size distribution for different samples of the same chemical, we created the simulation library to identify chemical samples that we may not have a spectrum for.

## 5.2 Contributions, Difficulties, and Surprises

This was a Herculean effort that involved many different people to accomplish. The members of my lab, Kaiwen and Lukas, performed numerical modeling for the

$As_2Se_3$ NA and dispersion requirements. Genny assisted in the development of the LWIR source and initial testing of the FTIR sensor. The folks at AFRL assisted in the $As_2Se_3$ loss measurements and the Michaelson interferometer measurements. Collaborators at OMNI science put together a prototype LWIR SC source box that could be transferred for measurements and testing. Augie and collaborators at Leidos developed the standoff FTIR measurement algorithms, and initial sensor optical configuration. Prof Terry and Prof Pierce modified the BV code to work for larger particle sizes. Prof Islam provided insight on two-photon absorption damage occurring in the $As_2Se_3$ and fought to get the FTIR sensor prototype transferred to the University of Michigan so that we can develop the system to perform standoff measurements. Some of my major contributions include the development of the ZBLAN attenuator that first allowed us to generate SC in the $As_2Se_3$ fiber, the methodology for fiber alignment and power scaling, alignment of the TurboFT as part of the launching optics as opposed to receiving optics to optimized the infrared energy traveling through the interferometer, and the creation of the simulation library and FOM used for unknown chemical identification.

The most difficult part of the project was determining a way to inject high peak-power SC into the $As_2Se_3$ without damaging the fiber face. Bulk optic coupling proved difficult because focusing broadband energy with lenses proved unreliable. We also found that two-photon absorption in the $As_2Se_3$ immediately destroyed the fiber face and therefore needed to filter out 1550 nm light with a thulium amplifier. The first instances of expansion came through the use of the ZBLAN attenuator to provide full spectrum input at lower overall power levels. This allowed our first glimpses of high-power expansion in the $As_2Se_3$ out to ˜6 µm. It was this initial expansion that led to the idea that a buffer was needed between the high output powers of the $SiO_2$/ZBLAN fibers and the $As_2Se_3$ fiber, and eventually led to a cascade involving light transfer from $SiO_2$ to ZBLAN to $As_2S_3$ to $As_2Se_3$.

There were several big surprises that we found during the development of the FTIR sensor for trace particle detection. First, we found that the infrared spectral features in gold scatterers contained sharp peaks that muddied spectral signatures when the gold scatterer was used as a background (as can be seen in Fig.3.12. Because of this, we decided to use specular reflectance from Si wafers and $BaF_2$ wedges as backgrounds since they are essentially featureless in the LWIR. This necessitated realignment between background and sample scans but provided quantifiable spectra that could be compared to our models. Another surprise was the clarity of spectra produced from glass samples compared to spectra measured on roughened aluminum. Early in the project, we had assumed that the high intensity return provided by the roughened aluminum substrate would emphasize chemical spectral features. What we found instead was that the aluminum scattering overpowered the chemical signature by at least an order of magnitude and hid the requisite features for chemical identification. Further work needs to be done to model these effects and mitigate the high substrate return. The glass sample, on the other hand, provided a very low signal that includes quantifiable peaks and troughs that can be used for chemical identification, even with glass substrate effects and atmospheric water masking parts of the LWIR.

This dissertation teaches how to create a LWIR SC source with high power output and ultra-wide broadband spectral coverage. We show how to utilize this source with an FTIR interferometer as an illuminator for standoff LWIR spectroscopic measurements. Finally, we teach how the BV model can be used to identify trace chemicals on smooth surfaces at standoff distances. The insights gained through these teachings further the realization of a non-contact, non-ionizing radiation, chemical identification system that can be used in real world applications. That being said, there is still much to be done to make a standoff LWIR spectroscopic sensor work beyond the lab setting.

## 5.3 Future Work

### 5.3.1 Fiber Limitations

The greatest challenge we face is the maintenance of the interfaces between different fiber types. Specifically, the ZBLAN fiber to $As_2S_3$ fiber in the fiber cascade tends to degrade over time in open atmosphere. So far, we have been able to prevent this deterioration by purging the interface with nitrogen to keep $H_2O$ content low, but a long-term solution may require a switch to $TeO_2$ fibers.

Tellurite and fluorotellurite fibers, though not as mature as ZBLAN fibers, show several advantages over their hydroscopic counterparts. Tellurite fibers have been shown to not absorb moisture, have transmission windows as wide as ZBLAN fibers, and have nonlinearities that are as high as two orders of magnitude higher than ZBLAN [1–4]. One study suggests that pumping a cascade of $TeO_2$ and $As_2S_3$ entirely in the normal regime can produce coherent supercontinuum generation strictly because of their high nonlinearity [5]. Unfortunately, these fibers are not yet commercially available, and can exhibit higher losses than their ZBLAN counterparts. Conversely, due to their high nonlinearity, broadband expansion can occur with shorter lengths of tellurite fiber than ZBLAN fibers, potentially offsetting the loss difference.

Another limitation lies in the availability of the high-NA $As_2Se_3$ fiber. The purification process for the selenide fibers is very difficult and a great deal of time has been spent by CorActive and IRflex trying to reproduce the fiber properties described in Fig. 2.2. Without a stable supply of low-loss high-index $As_2Se_3$ fiber, the LWIR SC source cannot be made commercially.

### 5.3.2 Improving SC Source Noise Performance

One of the limitations of using MI initiated SC sources for standoff illumination is that these SC sources tend to exhibit high levels of pulse to pulse variability. Because

modulation instability-initiated pulse breakup is a noise initiated nonlinear effect, the solitons which form in the anomalous regime are randomly generated and high energy solitons may form during different parts of the envelope pulse. This means that while the average power output might be very similar, there can be large spectral differences between single 1.5 ns pulses. There is continual research into ways to reduce the noise of supercontinuum based infrared sources that may aid in the noise performance of our system.

One method for improving SC pulse-to pulse stability is to use high non-linearity fibers in the normal dispersion regime to rely on self phase modulation and optical wave breaking based on the peak power of the system alone [5] for SC generation. The output SC maintains coherence, and for an OCT system for example, normal dispersion SC sources can exhibit 5 dB higher SNR [6]. Unfortunately, these sources typically require fs pulses with peak powers of up to 300 kW for spectral broadening. The ns pulses we use in our experiments typically output less than 15 kW peak power. This may be overcome with longer fiber lengths if the tellurite fiber maintains sufficiently low loss as the fiber lengths in [6] is only 10 cm in length. There are other challenges that include the small core size of the $TeO_2$ fiber to maintain all normal dispersion and preventing nonlinearities from occurring the $SiO_2$ fiber. These may be solved with dispersion tuning of either fiber, High non-linearity tellurite fibers, though still immature may be utilized to create all-normal regime supercontinuum generation into the LWIR.

Another method for increasing the pulse SNR is based upon dispersion tuning an early fiber in the SC cascade to reduce the relative intensity noise [7]. This occurs when a fiber has two zero dispersion wavelengths so that solitons rebound off of the second zero dispersion wavelength and deposit more energy at the edge of the spectra instead of falling into the high-loss regions and being absorbed by the fiber. This process may be used to increase spectral density before entering later

fibers in the cascade and maintaining the highest power solitons for input to the next fibers. Optimally, each fiber in the cascade should be dispersion tuned to prevent the expansion of solitons into the long wavelength edge of the fiber so that the energy can be used for expansion in the following fibers.

One study suggests inputting a seed pulse before the main SC pulse decreases pulse-to-pulse variability [8]. Modulation instability is typically noise-initiated, but the seeded pulse can initiate MI in a repeatable manner which normalizes the resulting pulse breakup and provides more consistent pulse characteristics. This methodology can potentially be adapted for our system and pulsed energy can be tapped after the second Er/Yb amplifier and reinjected before the amplifier to seed SC expansion. The length of the delay fiber will unfortunately be tied to the pulse repetition frequency and may need to be adjusted and optimized for various use cases.

A recent study also suggests that using in amplifier SC expansion can also decrease the relative intensity noise [9]. According to the study increasing the SC generation that occurs in amplifier or in gain fibers can lead to soliton alignment as high-power solitons are pushed out of the gain band of the amplifier. This effect can be further enhanced by using unpumped thulium fiber after the Er/Yb amplifier to increase spectral red shift and soliton alignment. While interesting, we may already be utilizing the benefits that this study suggests exist in SC generation, and may speak in favor of our ns pulse MOPA and concatenated SC fiber design.

The idea behind all these techniques is to improve the noise characteristics of the pulses that are to be injected into the SC generating fiber. Any noise from early in the system will be transferred to each of the following fibers. Any improvements in SNR at the early stages will improve the overall SNR of the source.

Other methods of increasing throughput and therefore signal, would be based around applying anti-reflection end-faces between fibers. Moth-eye structures can increase output from $As_2Se_3$ fibers by $> 12\%$ [10].

Overall, decreases the signal-to-noise performance in the source by 10 dB will reduce the number of scans required to achieve high-SNR spectra and coupled with advancements in the next section could reduce scan times to less than 5 seconds per scan.

### 5.3.3 Improving FTIR Sensor Performance

Currently, the speed of acquisition for the standoff LWIR SC and FTIR based sensor is limited by the transfer speed of the pulse data to the internal memory of the computer used to process and create interferograms. This bottleneck is caused by the need to sample over 140 points per pulse and the inclusion of $> 6000$ pulses per interferogram. The current triggered simultaneous acquisition and record program cannot transfer the information fast enough to prevent the rotating buffer memory to fill completely at higher pulse repetition frequencies. Thus, our system is limited to a 300 kHz pulse repetition frequency. One of the ways to prevent a data transfer bottleneck would be to activate pulse processing directly on the acquisition card. Namely determining the pulse energy on the acquisition card itself would reduce the amount of data transferred by 140 times. This would open the possibility of scaling the LWIR SC source output and rotation rate without worrying about transfer speeds limiting data acquisition.

Scanning 1000 scans has an acquisition time of 69 s, but if the bottleneck described above is mitigated we could potentially obtain quality scans much faster. The highest pulse repetition frequency described in this dissertation is 800 kHz. If we were to run the source at 800 kHz and scale the rotation rate of the Turbo FT correspondingly, that would reduce the acquisition time of 1000 scans to 25.8 s. If we then increase the rotation rate of the Turbo FT by another factor of 2 because we do not require spectra in the MWIR for chemical identification, we further reduce the time for 1000 scans to be 12.9 s. Another factor of 2 in speed can be gained by collecting 500 scans

as opposed to 1000 and we can create robust spectra in under 10 sec. If the continuous measurement features that are inherent in commercial FTIR systems is utilized, the LWIR SC and FTIR based sensor can become a real-time sensor that measures spectra in real-time and can be used to scan across various surfaces for drastic changes in spectra.

The greatest improvement to this system would be gained through creating a standoff imaging sensor to create hypercubes similar to those created when using QCLs for standoff chemical detection. According to [11] for the number of samples along the interferogram required for a given resolution and wavenumber range is given by:

$$N_s = \frac{2(\widetilde{\nu}_{\max} - \widetilde{\nu}_{\min})}{\Delta\widetilde{\nu}} \tag{5.1}$$

where $N_s$ is the number of points to be sampled, $\widetilde{\nu}_{\max}$ and $\widetilde{\nu}_{\min}$ are the maximum and minimum wavenumbers, respectively, and $\Delta\widetilde{\nu}$ is the resolution of the resulting spectra. Our current system samples ˜6000 pulses when the system is running at 300 kHz pulse repetition frequency. This corresponds to 3.3 µs between 1.5 ns pulses. One of the fastest HgCdTe cameras in use for QCL hypercube measurements is a 128 x 128 pixel camera that can measure 138 frames in 14 ms when in sub-window mode (16 x 96 pixels) [12]. This corresponds to 101.45µs per frame. Each frame, therefore, would be an average of 30 pulses, and would lead to a sampling number of 200 pulses per interferogram. If we limit the band of the spectra to 950 - 1750 cm−1, we can achieve a theoretical resolution of 8 $cm^{-1}$ and can create hypercube images with spectral data. Creating images becomes extremely important for the detection of trace chemicals on roughened surfaces by baseline subtracting the bulk background spectra in real-time.

Once imaging becomes available, increasing imaging distance becomes a matter of implementing telescoping optics that can collect as much light as possible over a

broad range of wavelengths. The collection optics shown in Fig. 3.5 are commercially available mirrors. In a new study, our collaborators describe an optical setup with spectral measurements performed at 10 m distances [13] with an SNR similar to the measurements we perform at 3.6 m. Following the calculations performed for Fig. 4.13(b), this sensor configuration should be able to measure spectra up to 50 m, with high chemical loading.

### 5.3.4 Limitations of BV Theory

BV theory provides accurate diffuse scattering spectra for individual particles that have been deposited on a smooth surface. As soon as the particles begin to aggregate or form a film, BV theory begins to break down and scattered spectra may no longer match with simulations. Further work needs to be done to develop a model to simulate spectra from bumpy thin films that may result from wiping surfaces with various cleaning agents.

The BV model is a computationally intensive simulation technique. Incorporation of the Videen approximation may help to create spectra for larger particle sizes in more reasonable time frames. Currently it may take at least 15 hours to simulate scattering from a particle with a radius of 15 µm.

### 5.3.5 Measurement of Trace Particles on Roughened Substrates

The work presented in this dissertation is focused on the measurement of trace chemicals deposited on smooth substrates. Understanding the fundamentals of smooth substrate measurements is a stepping stone for the much more difficult problem of measuring spectra from particles that are deposited on surfaces that scatter signal themselves. One of the main challenges will derive from the high signal return from the substrate itself that may overpower the trace chemical signal by over an order of magnitude. One of the ways that standoff spectroscopists have overcome this hurdle

is with detection mapping of hyperspectral images [14]. This method uses a hyperspectral image cube that normalizes the blank regions of the substrate and detects any changes compared to that background. They then measure the spectra of the bright or dark spots found on the surface. When divided by the substrate, Mie theory for specific particle sizes can be used to match peak positions. If the above use of a HgCdTe camera can be implemented for LWIR SC and FTIR based illumination, we would be able to similarly measure spectra by creating an interferogram cube that can be Fourier transformed to create a hyperspectral image cube. There should be no difference in spectra between trace particles illuminated with swept QCLs or with FTIR modulated supercontinuum sources.

Apart from imaging techniques, recent study has found that particles on roughened surfaces exhibit reflectance troughs that are deeper than particles on smooth substrate [15]. They are able to accurately fit spectra of $KClO_2$ measured on roughened gold by multiplying their smooth substrate spectra by a multiplicative factor and an offset based off of the substrate roughness. If the original backscattered spectra is $Q_i$, then the new spectra $Q_i'$ is described as:

$$Q_i' = f(\rho)Q_i + g(\rho) \tag{5.2}$$

$$f(\rho) = a_1 + a_2\rho^{0.25} + a_3\rho^{0.5} \tag{5.3}$$

$$g(\rho) = b_1 + b_2\rho^{0.25} + b_3\rho^{0.5} \tag{5.4}$$

where $\rho$ is a measure of the roughness and the coefficients for $a_i$ and $b_i$ are obtained through a global fit. We could very easily implement this change in fitting the measurement of trace chemicals on scattering substrates if the roughness is known. Additional parameterizations may need to occur for substrates with an arbitrary roughness. This roughness metric may be unnecessary if we decide to use second order derivatives for chemical identification because the FOM used in Chap. IV depends

more strongly on peak position than relative peak height changes.

### 5.3.6 Chemical Identification

The discussion of the figure of merit in subsection 4.6.1, shows that the rms error between the second derivative of the library values and the second derivative of the measured spectra may not have a high enough dynamic range to accurately differentiate chemicals that may contain shallow reflectance features or too many zero crossings. Because of this it would be beneficial to use machine learning algorithms for classification [16] with or without principle component analysis to reduce the number size of the data input [11]. Supervised machine learning could be used to group data according to characteristics found in their spectra, where new unknown spectra can be grouped under a specific classification. Second derivative spectra should still be used during analysis to emphasize the sharp chemical features in the molecular fingerprint regime.

### 5.3.7 BV Modeling for Microscopic FTIR Analysis

The BV solutions for a specific particle size can be integrated over various collection angles to produce spectra that may be collected by complicated optics. One such example is the illumination and collection optics required for microscopic FTIR measurements which involve the use of a Cassegrain reflector to focus a semi-hemisphere of light onto a sample. The same Cassegrain reflector is used to capture reflected energy from the opposite semi-hemisphere through a preset aperture. The reflectance spectra would include the integration of 22° - 30° wedge integrated around an azimuthal angle between 180° and 360°. A separate calculation would need to be performed for every illumination angle within the same wedge, with azimuthal angle between 0° and 180° with a step size that would need to be determined through repetition.

This process would be computationally intensive, but would provide spectra that

is useful for microspectroscopy applications such as the investigation of particle contamination on diffraction gratings or other delicate surfaces that cannot be touched or polished without damage. It can also be useful in the examination of microstructures that are used to create anti-reflection coatings on fiber tips to determine if other contaminants from stamping process are left on the fiber surface.

### 5.3.8 Comparisons to QCL Hypercube Sensing

A major competitor LWIR SC FTIR sensor presented in Chapter III is the use of quantum cascade lasers with a LWIR imaging camera [17, 18]. Instead of requiring an FTIR spectrometer to modulate the signal of a broadband source, an external-cavity QCL can scan across wavelengths of interest while a camera records scattered spectra per pixel over time. By matching time stamps with wavelength, a hypercube of intensity vs wavelength vs position can be created for trace chemical location and identification. The modeling theory described in Chapter IV applies to measurements made via QCL, but with the aid of images to locate chemical contamination.

FTIR spectroscopy has the potential for providing full spectra faster than QCLs can scan across the requisite wavelength range for chemical identification, but until pulse-to-pulse variation in spectra can be mitigated or compensated for, QCL sources can provide images in ˜12 s, or about as fast as the LWIR SC sensor can collect a single spectra [19].

### 5.3.9 2D Array Detector for Standoff LWIR Sensing

One of the ways to create fast hyperspectral measurements while utilizing the total output of the LWIR SC source would be to use a two-channel detector array coupled to a LWIR diffraction grating. The diffraction grating would separate the incoming light by wavelength along one direction of the array and provide a 1D image along the other. By scanning the collection optics, a 3D hyperspectral cube can be

formed quickly and efficiently.

Currently, we average 8 measurements of 500 scans to produce high SNR spectra. That means that a pulse along the interferogram is averaged roughly 4000 times. If we were to run the LWIR SC source at 400kHz, the pulse averaging can be achieved in 10 ms for a 1D strip. For robustness, you may double the acquisition time and add another 20 ms delay time between scanning mirror positions and a 128 x 128 pixel hypercube can be collected within 5.12 s. By doubling the pulse repetition frequency, this can drop to 2.56 s. A 128 x 128 pixel array could potentially be used to measure a wavenumber range of 980 - 1492 $cm^{-1}$ every 4 $cm^{-1}$.

Additionally, if we include a second grating and detector array as a reference arm, the simultaneous acquisition of both sample and reference arm data can eliminate pulse-to-pulse variation noise. The SNR may increase from ˜10 dB per pulse to within the noise limit of the detectors as seen in some studies where reference arms were used to account for SC source fluctuations [20]. This would drastically reduce the number of pulses required to collect high SNR spectra and decrease the acquisition time by at least an order of magnitude.

### 5.3.10 Future of LWIR Sources for Standoff Chemical Detection

With the advancements of LWIR sources, detectors, and fibers it is possible to create a standoff imaging sensor that can create hypercube images in less than a second. QCLs currently produce the fastest spectra and are showing great promise for standoff measurements on a wide array of substrates because of their ability to background subtract spectra in real-time. Optical parametric amplifier pumped non-linear crystals are swiftly approaching power levels in the LWIR that were presented in Chapter II, [21] and may provide better noise characteristics due to the direct pumping of fs pulses into the nonlinear crystal at the cost of a non-fiber coupled output

If the noise performance of the sensor can be improved via source pulse-fluctuation improvements or the use of 2D detector arrays and a reference arm, real-time short range investigation of scattered spectra, like that from luggage scanned by TSA could be available within 10 years for SC based devices. If the reproducibility of the $As_2Se_3$ fiber does not improve, OPO pumped nonlinear crystals are very likely to become a common LWIR SC source for standoff broadband illumination.

Quantum Cascade Laser based sources can currently measure concentrations as low as 100 ng/cm$^2$ at 1 m distances, and high SNR spectra of higher loading samples at 15 m [19]. The distance and concentration limits should only improve because LWIR QCL technology and stability have improved at pace with that of LWIR SC sources. Their use in short-range standoff applications should start becoming more prevalent within 5 years as imaging is already possible with these sources. QCLs may become more pervasive than SC sources as a LWIR source because wavelength tuning occurs source side and does not require additional components, such as gratings or interferometers to produce spectra. This makes QCLs great for wavelength-based investigation where the entire spectra provided by SC sources may not be necessary.

## References


[1] Aoxiang Lin, Aleksandr Ryasnyanskiy, and Jean Toulouse. Fabrication and characterization of a water-free mid-infrared fluorotellurite glass. *Optics letters*, 36(5):740–742, 2011.

[2] P Domachuk, NA Wolchover, M Cronin-Golomb, A Wang, Alan K George, CMB Cordeiro, Jonathan C Knight, and FG Omenetto. Over 4000 nm bandwidth of mid-ir supercontinuum generation in sub-centimeter segments of highly nonlinear tellurite pcfs. *Optics Express*, 16(10):7161–7168, 2008.

[3] Than Singh Saini, Nguyen Phuoc Trung Hoa, Tong Hoang Tuan, Xing Luo, Takenobu Suzuki, and Yasutake Ohishi. Tapered tellurite step-index optical fiber for coherent near-to-mid-ir supercontinuum generation: experiment and modeling. *Applied optics*, 58(2):415–421, 2019.

[4] Huan Zhan, Tengfei Shi, Aidong Zhang, Zhiguang Zhou, Jinhai Si, and Aoxi-

ang Lin. Nonlinear characterization on mid-infrared fluorotellurite glass fiber. *Materials Letters*, 120:174–176, 2014.

[5] Hoa Phuoc Trung Nguyen, Kenshiro Nagasaka, Tong Hoang Tuan, Than Singh Saini, Xing Luo, Takenobu Suzuki, and Yasutake Ohishi. Highly coherent supercontinuum in the mid-infrared region with cascaded tellurite and chalcogenide fibers. *Applied optics*, 57(21):6153–6163, 2018.

[6] Mikkel Jensen, Iván Bravo Gonzalo, Rasmus Dybbro Engelsholm, Michael Maria, Niels Møller Israelsen, Adrian Podoleanu, and Ole Bang. Noise of supercontinuum sources in spectral domain optical coherence tomography. *JOSA B*, 36(2):A154–A160, 2019.

[7] Rasmus Dybbro Engelsholm and Ole Bang. Supercontinuum noise reduction by fiber undertapering. *Optics express*, 27(7):10320–10331, 2019.

[8] Ziqi Jiang, Tianshu Wang, Zhiwen Sun, Junda Chen, Xinmeng Zhang, Peng Lin, Peidi Chen, and Yiwu Zhao. Partially coherent seeding of supercontinuum generation in picosecond regime. *Optics & Laser Technology*, 120:105752, 2019.

[9] Kyei Kwarkye, Mikkel Jensen, Rasmus D Engelsholm, Manoj K Dasa, Deepak Jain, Patrick Bowen, Peter M Moselund, Christian R Petersen, and Ole Bang. In-amplifier and cascaded mid-infrared supercontinuum sources with low noise through gain-induced soliton spectral alignment. *Scientific Reports*, 10(1):1–11, 2020.

[10] Mikkel Lotz, Julius Needham, Mogens H Jakobsen, and Rafael Taboryski. Nanoimprinting reflow modified moth-eye structures in chalcogenide glass for enhanced broadband antireflection in the mid-infrared. *Optics letters*, 44(17):4383–4386, 2019.

[11] Peter R Griffiths and James A De Haseth. *Fourier transform infrared spectrometry*, volume 171. John Wiley & Sons, 2007.

[12] David B Kelley, Derek Wood, Anish K Goyal, and Petros Kotidis. High-speed and large-area scanning of surfaces for trace chemicals using wavelength-tunable quantum cascade lasers. In *Chemical, Biological, Radiological, Nuclear, and Explosives (CBRNE) Sensing XIX*, volume 10629, page 1062909. International Society for Optics and Photonics, 2018.

[13] Augie Ifarraguerri, N Convers Wyeth, and Brian Gorin. Optical design for an active standoff spectrometer with a broadband source. *Optical Engineering*, 59(9):092006, 2020.

[14] Anish K Goyal, Derek Wood, Vincent Lee, Joshua Rollag, Peter Schwarz, Leyun Zhu, and Gary Santora. Laser-based long-wave-infrared hyperspectral imaging system for the standoff detection of trace surface chemicals. *Optical Engineering*, 59(9):092003, 2020.

[15] Robert Furstenberg, Andrew Shabaev, Christopher A Kendziora, Christopher Breshike, Tyler J Huffman, Andrew Kusterbeck, Dawn Dominguez, Samuel G Lambrakos, and R Andrew McGill. Synthetic models for infrared reflectance signatures of micro-particle traces on surfaces. In *Chemical, Biological, Radiological, Nuclear, and Explosives (CBRNE) Sensing XX*, volume 11010, page 110100K. International Society for Optics and Photonics, 2019.

[16] Sotiris B Kotsiantis, I Zaharakis, and P Pintelas. Supervised machine learning: A review of classification techniques. *Emerging artificial intelligence applications in computer engineering*, 160(1):3–24, 2007.

[17] Christopher J Breshike, Christopher A Kendziora, Robert Furstenberg, Viet Nguyen, Andrew Kusterbeck, and R Andrew McGill. A system for rapid chemical identification based on infrared signatures. In *Micro-and Nanotechnology Sensors, Systems, and Applications X*, volume 10639, page 1063927. International Society for Optics and Photonics, 2018.

[18] Christopher J Breshike, Christopher A Kendziora, Robert Furstenberg, Yohan Yoon, TJ Huffman, Viet Nguyen, and R Andrew McGill. Rapid detection of infrared backscatter for standoff detection of trace explosives. In *Chemical, Biological, Radiological, Nuclear, and Explosives (CBRNE) Sensing XXI*, volume 11416, page 114160W. International Society for Optics and Photonics, 2020.

[19] Christopher J Breshike, Christopher A Kendziora, Robert Furstenberg, TJ Huffman, Viet Nguyen, Norman Budack, Yohan Yoon, and R Andrew McGill. Hyperspectral imaging using active infrared backscatter spectroscopy for detection of trace explosives. *Optical Engineering*, 59(9):092009, 2020.

[20] Kaiwen Guo, Tianqu Zhai, Brandon Demory, Shawn Meah, Ramon Martinez, Mohammed N Islam, Fred Terry, and Robert Maynard. Stand-off non-destructive determination of protein level in wheat flour with a super-continuum laser. In *Optical Biopsy XVIII: Toward Real-Time Spectroscopic Imaging and Diagnosis*, volume 11234, page 112340W. International Society for Optics and Photonics, 2020.

[21] Sergey Vasilyev, Viktor Smolski, Igor Moskalev, Jeremy Peppers, Mike Mirov, Yury Barnakov, Vladimir Fedorov, Dmitry Martyshkin, Andrey Muraviev, Kevin Zawilski, et al. Multi-octave infrared femtosecond continuum generation in cr: Zns-gase and cr: Zns-zgp tandems. In *Nonlinear Frequency Generation and Conversion: Materials and Devices XIX*, volume 11264, page 1126407. International Society for Optics and Photonics, 2020.